PARMA UNIVERSITY

Physics Department

Magnetic Carbon

Angelo Goffredi

Thesis submitted for the award of the degree of PhD in

Science and Technology of the Innovative Materials

Reviser: Dr. Matteo Belli

Prof. Mauro Riccò research group

XXI Cycle – December 2008

This document was typeset in Office Word 2003
The file in Portable Document Format was generated with Adobe 7.0 - PdfMaker

---

Author's address:

Angelo Goffredi
B. Grioli street, 20 - 46100 Mantua, Italy
E.mail: angelo.goffredi@fis.unipr.it,
Web: www.fis.unipr.it/home/angelo.goffredi

To my beloved Ramona and Fabio

Contents

INTRODUCTION 11

1.1 MAGNETIC CARBON HISTORY 12
1.2 ROOM TEMPERATURE FERROMAGNETISM: FULLERENES 16
1.2.1 Ferromagnetism in fullerene based materials 16
1.2.2 Does the magnetic signal really come from carbon? 17
1.2.3 C_{60} Hydrides 18
1.2.4 Photopolymerized fullerenes 18
1.2.5 Pressure – polymerized fullerene 23
1.3 ROOM TEMPERATURE FERROMAGNETISM: GRAPHITE 26
1.3.1 Proton bombarded graphite 27
1.4 ROOM TEMPERATURE FERROMAGNETISM: AN OVERVIEW OF STRIKING RESULTS 34

RESULTS AND DISCUSSION 37

2.1 INTRODUCTION 38
2.2 FERROMAGNETISM IN C_{60} POLYMERS 38
2.2.1 Hole doped C_{60} polymers: $C_{60}(AsF_6)_2$ 39
2. 3 Mg_5C_{60} POLYMER 45
2.3 NEUTRON IRRADIATED GRAPHITES 50
2.3.1 LENA Reactor Pavia 50
2.3.2 Boron enriched graphite 54
2.3.2 Intercalated graphites 64

CONCLUSIONS 72

EXPERIMENTAL SECTION 76

4.1 EXPERIMENTAL DETAILS 77
4.1.1 X-Rays Diffraction measurements 77
4.1.2 SQUID measurements 79
4.1.3 NMR Analysis 80
4.1.4 Chemical details 80
4.2 SYNTHETIC REPORT 81
4.2.1 Synthesis of Fullerenium dihexafluoroarsenate 81
4.2.2 Synthesis of Magnesiumanthracene • 3THF complex 83
4.2.3 Synthesis of Magnesium Fullerite 84
4.2.4 Synthesis of Borazine 85
4.2.5 Synthesis of stage I/II- K-GIC (KC_8 – KC_{24}) 88
4.2.6 Synthesis of Borazine intercalated KC_{24} 90

4.2.7 Synthesis of BCl_3 intercalated KC_{24} 92
4.2.8 Synthesis of NH_3 intercalated KC_{24} 94
4.2.9 Synthesis of SO_3 intercalated graphite 96
4.2.10 Synthesis of Exfoliated RW-A Graphite 98
4.2.11 Synthesis of $NaBH_4$ Graphite composite 101

FIGURES INDEX 103

SCHEMES INDEX 111

BIBLIOGRAPHY 114

ACKNOWLEDGEMENTS 122

Introduction

1.1 Magnetic Carbon History

It is worth noting that human beings chemistry depends on the element Carbon. The number of known allotropes of this extraordinary element continues to grow, from graphite and diamond producing materials like fullerenes, nanotubes and their derivatives which are both scientifically fascinating and have a huge number of potential applications.

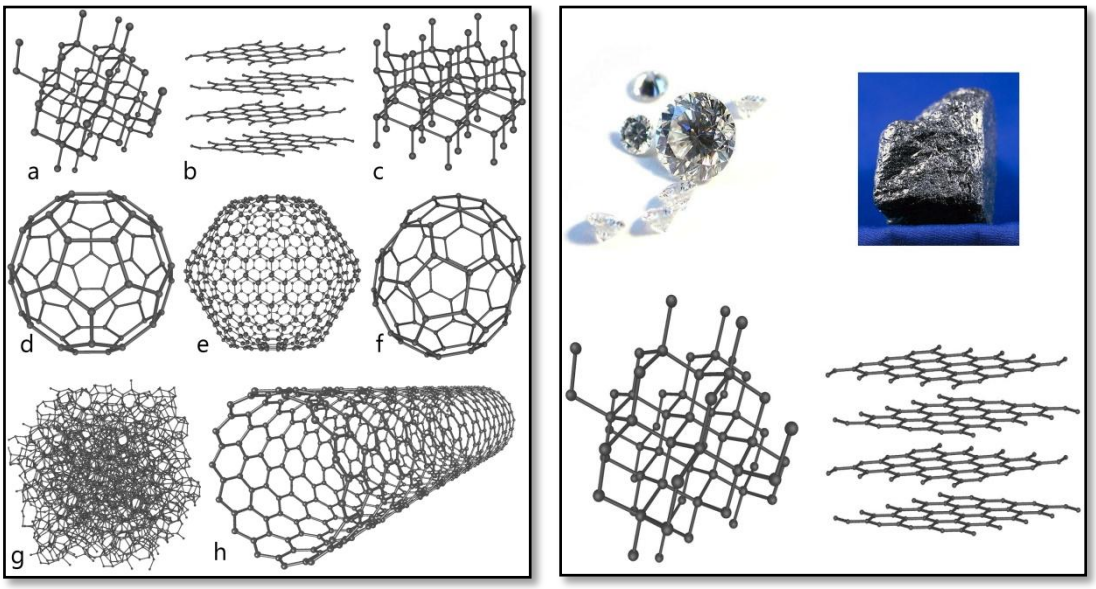

Figure 1: *Left)* The structures of eight carbon allotropes, a) Diamond, b) Graphite, c) Lonsdaleite, d) C_{60} (Buckminsterfullerene or buckyball), e) C_{540}, f) C_{70}, g) Amorphous carbon, and h) single-walled carbon nanotube or buckytube. *Right)* Visualization of the two well-known carbon allotropes: Diamond and Graphite

Despite many decades of work, even the properties of the well known graphite are still poorly understood. Although it is familiar to most people for its long list of everyday life applications such as in pencils or as a lubricant or even as a weapon against electrical installations, unexpected behaviour has been reported in the last five years, including two-dimensional electronic transport[1,2], metal-insulator transitions[3,4], extraordinary magneto-resistance[2,5], magneto-striction and even superconductivity[6].

[1] H. Kempa, P. Esquinazi and Y. Kopelevich, *Phys. Rev. B*, **65** 241101(R).

Everyday life is full of another well-known and useful materials: *magnets* which traditionally take the form of three-dimensional solids, oxides, metals and alloys. Magnets have played an important role in civilization since the earliest times. Vikings, for example, navigated their ships using a fish-shaped piece of lodestone on a floating support as a compass. Today, from electricity generation to small kitchen appliances, not to mention cars, headphones and laptop computers, magnets are essential components of our life (see Figure 2). Traditional materials used for making magnets include iron and iron oxides (lodestone and ferrites).

Figure 2: Everyday life is full of magnets, for example **a)** modern cars contains up to 30 Kg of high intensity magnetic material, **b)** natural medicine in some cases utilize magnets for therapies, **c)** magnets can even be found in modern toys and **d)** the magnetic resonance technique represents our medical forefront.

---

[2] Y. Kopelevich, J. H. S. Torres, R. R. da Silva, F. Mrowka, H. Kempa, and P. Esquinazi, *Phys. Rev. Lett.*, **90** 156402 (2003).
[3] Y. Kopelevich, P. Esquinazi, J. H. S. Torres, R. R. da Silva, and H. Kempa, *Advances in Solid State Physics* **43**, 207 (2003).
[4] T. Tokumoto, E. Jobiliong, E. S. Choi, Y. Oshima, and J. S. Brooks, *Solid State Commun.* **129**, 599 (2004).
[5] K. Ishii, A. Fujiara, H. Suernatsu, Y. Kubozono, *Phys. Rev. B*, **65** 134431 (2002).
[6] E. A. Ekimov, V. A. Sidorov, E. D. Bauer, N. N. Mel'nik, N. J. Curro, J. D. Thompson, S. M. Stishov, *Nature* **428** 542 (2004).

However, scientists are today interested in developing magnets from molecular materials whose constituent atoms are non-metallic. Such metal-free magnets would be electrical insulators (reducing energy losses in some applications) and should be cheaper, lighter, more eco-friendly and biologically compatible than their metallic counterparts.

All magnets lose their magnetic character above a critical temperature T_C, which in the case of ferromagnets is also called the Curie temperature. Below T_C the magnetic moments of electrons in the material order in such a way that a net macroscopic magnetization arises. For instance, in some materials, namely ferromagnets such as iron, magnetic ordering aligns all the moments parallel to each other. But this is only the simplest magnetic structure for a magnet, and many other more complex structures are also possible.

Although Heisenberg rejected the idea of π-electron magnetism[7], prior to the turn of the millennium nearly 100 papers and 30 patents describing ferromagnetic structures containing either pure carbon or carbon combined with first row elements[8] were published. These results were difficult to reproduce, but in more recent years the discovery of room temperature ferromagnetism have attracted huge interest in the scientific community; the discovery of ferromagnetism in pressure-polymerized fullerenes was included in Top-Ten of Physics and in Chemistry Highlights in 2001[9,10]. Furthermore the finding that graphite can also be turned ferromagnetic through irradiation led the newsletter of the American Physical Society to choose this topic for its Focus page in 2003[11], concentrating on the possibility of producing "mini magnets" with possible applications in nanoscale electronics.

[7] W. Heisenberg, *Z. Phys.* **49,** 636 (1928).
[8] Reviewed in: T. L. Makarova, *Studies of high-T_c Superconductivity*, **45**, 107 (2003).
[9] *Chemical and Engineering news* "Chemistry highlights 2001" **79,** 45 (2001).
[10] K. Pennikod, Highlights of the year. *Physics Web* **20** (2001).
http://physicsweb.org/article/news/5/12/11#11
[11] http://focus.aps.org/story/v12/st20 from 25.11.2003.

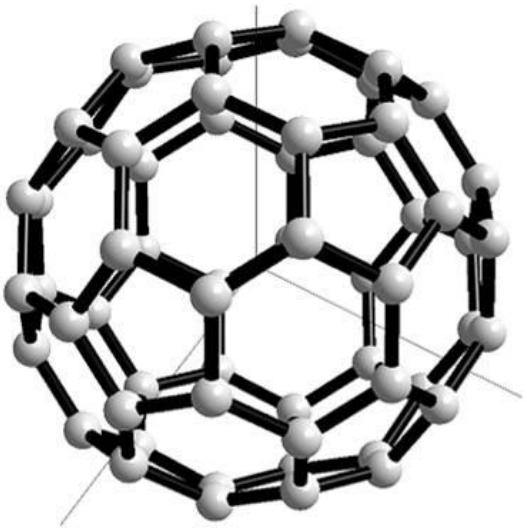

Figure 3: Ball&stick structure of Fullerene (C_{60}).

Today, nonmagnetic-defect-induced magnetism in carbon based solids[12,13] is a hot-boiling topic, especially in graphene systems like single graphite planes. A defective graphene phase is foreseen to behave as a room temperature ferromagnetic semiconductor[14].

These results might lead the way to nanoscale spintronics through carving the graphene: however, still nobody knows how to reach it in practice.

Instead, there is rich experimental evidence on magnetism in carbon-based molecules and materials[15]. Ferromagnetism was found in carbon nanospheres[16], macrotubes[17], nanorods[18] and irradiated fullerenes[19]. Elementally sensitive experiments on proton bombarded graphite provided fast evidence for metal-free carbon magnetism[20].

---

[12] F. Lopez-Urias, J. A. Rodriguez-Manzo, M. Terrones, H. Terrones, *Int. J. Nanotech.* **4,** 651(2007).
[13] T. L. Makarova in "Progress in Industrial Mathematics" Vol. 12, L. L. Bonilla et al., Eds. 467 (2007).
[14] L. Pisani, J. A. Chan, B. Montanari and N. M. Harrison, A defective graphene phase predicted to be a room temperature ferromagnetic semiconductor, *New Journal of Physics* **10**, 033002 (2008).
[15] Carbon based magnetism: an overview of the magnetism of metal free carbon-based compounds and materials, Edited by T. Makarova, F. Palacio, Elsevier Science, 576 pag (2006).
[16] R. Caudillo, X. Gao, R. Escudero, J. B. Goodenough, *Phys. Rev. B* **74**, 214418 (2006).
[17] S. Li, Z.G. Huang, L. Lue, F. M. Zhang, Y. Du, Y. Cai, Y. G. Pan, *Appl. Phys. Lett.* **90,** 232507 (2007).
[18] N. Parkansky, B. Alterkop, R. L. Boman, Z. Barkay, Y. Rosenberg, N. Eliaz, *Carbon* **46,** 215 (2008).
[19] A. Kumar, D. K. Avasthi, J. C. Pivin, A. Tripathi, F. Singh, *Phys. Rev. B.* **74**, 153409 (2006).
[20] H. Ohldag, T. Tyliszczak, R. Höhne, D. Spemann, P. Esquinazi, M. Ungureanu, T. Butz, π-Electron Ferromagnetism in Metal-Free Carbon Probed by Soft X-Ray Dichroism, *Phys. Rev. Lett.* **98**, 187204 (2007).

1.2 Room temperature ferromagnetism: Fullerenes

Ferromagnetism has been observed in various fullerene based materials. In the following chapters, an overview of the main goals in this field ranging from fullerenes to irradiated graphites will be presented.

1.2.1 Ferromagnetism in fullerene based materials

Simple C_{60} doping with a strong donor like Tetrakisdimethylaminoethylene (TDAE), shows bulk ferromagnetism. The Curie temperature referred to high-quality samples of $[TDAE]^{+\bullet} C_{60}^{-\bullet}$ reached values of 16 K[21] (see Figure 4).

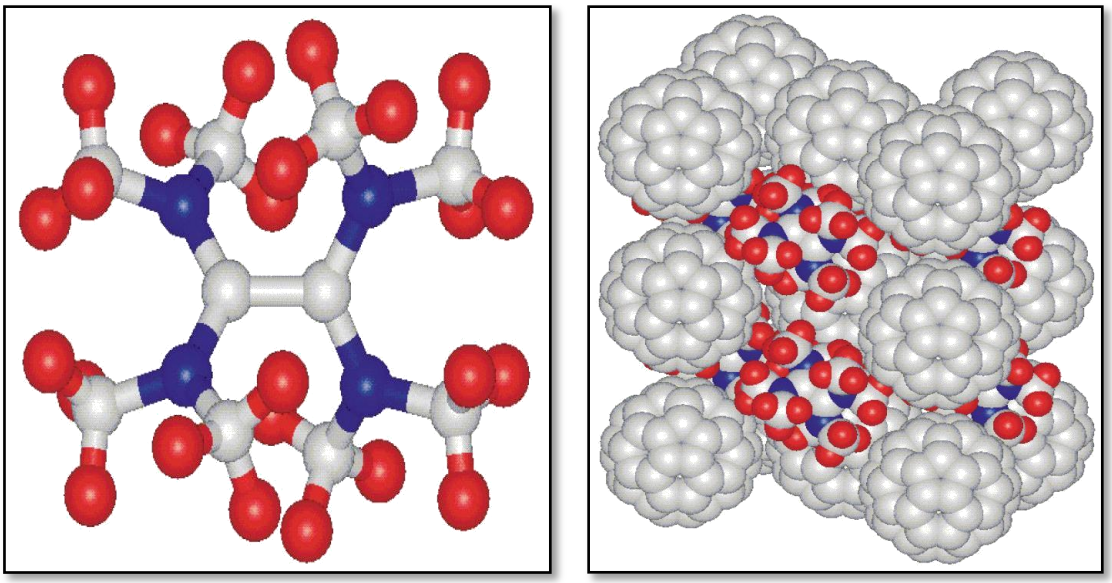

Figure 4: *Left)* Tetrakisdimethylaminoethylene (red: hydrogen; blue: nitrogen; grey: carbon). *Right)* Structure of $[TDAE]^{+\bullet} C_{60}^{-\bullet}$.

[21] P. M. Allemand, K. C. Kishan, A. Koch, F. Wudl, K. Holczer and J. D. Thompson, *Science* **253**, 301-3 (1991).

However a real striking discovery on fullerenes has been represented by a composite of C_{60} containing a polymeric film. These samples were produced by ultrasonic dispersion of C_{60} in dimethylformamide solution of polyvinylidenefluoride and subsequent vacuum evaporation of the solution. The Curie point and magnetization were 370 K and 0.210 emu/g: room-temperature ferromagnetism[22]. The contamination with Fe, Mn, Cr, Co and Ni was less than 0.001; 0.0005; 0.001; 0.002 and 0.005 wt.%, respectively, and it could not explain the observed magnetization. In addition, as described in a patent[23], ultrasonic dispersion of fullerenes (C_{60}, C_{70}, C_{76} or C_{84}) in organic polymer or in a non-conducting liquid forms a light processable magnetic material.

1.2.2 Does the magnetic signal really come from carbon?

Impurity checking plays a very important role in the amazing field of synthesizing pure organic ferromagnets. As a matter of fact, the central question in the study of magnetic properties of pure carbon systems is whether its nature is intrinsic or extrinsic. Being homogeneously distributed in the carbon matrix, the iron impurities cannot contribute to the magnetic ordering due to the large interatomic distances. One should, however, consider the possibility of clusterization of metallic atoms. If we assume that all iron impurities in the samples are concentrated in a cluster with Fe_3O_4 composition, the contribution of such a cluster to the magnetization values would be estimated 0.02 emu/g. In the majority of the papers the magnetization values substantially exceed this quantity even if in some articles the magnitudes are comparable. An important issue is that there is no difference in the impurity content among the samples examined, but the magnetic properties are strongly dependent on the preparation conditions: reaction time, temperature and atmosphere. It is highly desirable to produce totally metallic-free organic substances. However, contamination

[22] M. Ata, M. Machida, H. Watanabe, and J. Seto., *Jpn. J. Appl. Phys.* ***33***, 1865 (1994).
[23] T. Yanada, Japanese Patent JP5159915 (1993).

of iron is often unavoidable, and it is significant to know the effect of tiny amounts of metal to the magnetic properties[24].

1.2.3 C_{60} Hydrides

Fullerene hydride $C_{60}H_{36}$ has been reported to be a room-temperature ferromagnet with M_s = 0.04 emu/g[25]. Higher values of magnetization have been found for the composition $C_{60}H_{24}$[26]: although some differences from sample to sample, the magnetization reaches the value of 0.16 μ_B/C_{60} (i.e. 1.2 emu/g). Measured by atomic-emission mass spectrometry analysis, the concentration of all the detected metals in the most magnetic sample (0.16 μ_B/C_{60}) was the following: Fe: 0.01; Ni: 0.002; Pd: 0.01; Al: 0.05; Cu: 0.1 (wt.%). In other words the signal due to those metallic impurities could not explicate the entire magnetic signal, thus confirming the intrinsic magnetic ordering of hydrofullerites. In addition, the authors said that a circumstantial evidence of the intrinsic nature of that ferromagnetism is aging: one-year storage brings the samples to a diamagnetic state.

1.2.4 Photopolymerized fullerenes

Another interesting system has been recognized in polymerized fullerenes: room-temperature ferromagnetism was first reported in 1996[27].

Since the first system of polymerized C_{60}[28], subsequent extensive investigations evidenced a huge variety of structures, either 1D or 2D or 3D dimensionally arranged[29,30,31].

---

[24] A. Talyzin, A. Dzwilewski, L. Drubovinsky, A. Setzer, & P. Esquinazi, Magnetic properties of polymerized C_{60} with Fe, *The European physical journal B* **55**, 57-62 (2007).
[25] A. S. Lobach, Yu. M. Shulga, O.S. Roshchupkina, A. I. Rebrov, A. A. Perov, Y. G. Morozov, V. N. Spector, and A. A. Ovchinnikov, *Fullerene Sci. Technol.* **6**, 375 (1998).
[26] V. E. Antonov, I. O. Bashkin, S. S. Khasanov, A. P. Moravsky, Yu. G. Morozov, Yu. M. Shulga, Y.A. Ossipyan, E. G. Ponyatovsky, *J. Alloys, and Comp.* **330**, 365 (2002).
[27] Y. Murakami and H. Suematsu, *Pure Appl. Chem.* **68,** 1463 (1996).
[28] A. Rao, T. Lee, X. X. Bi, "Photoinduced polymerization of solid C_{60} films", *Science* **259**, 955 (1991).

Despite that large family of compounds, C_{60} follows substantially two polymerization reactions: [2+2] cycloaddition (Diels-Alder reaction scheme) which leads to a four-member carbon ring formation and single C-C covalent bond genesis. Cycloaddition is the most common process and characterise both doped and undoped systems (see Figure 5).

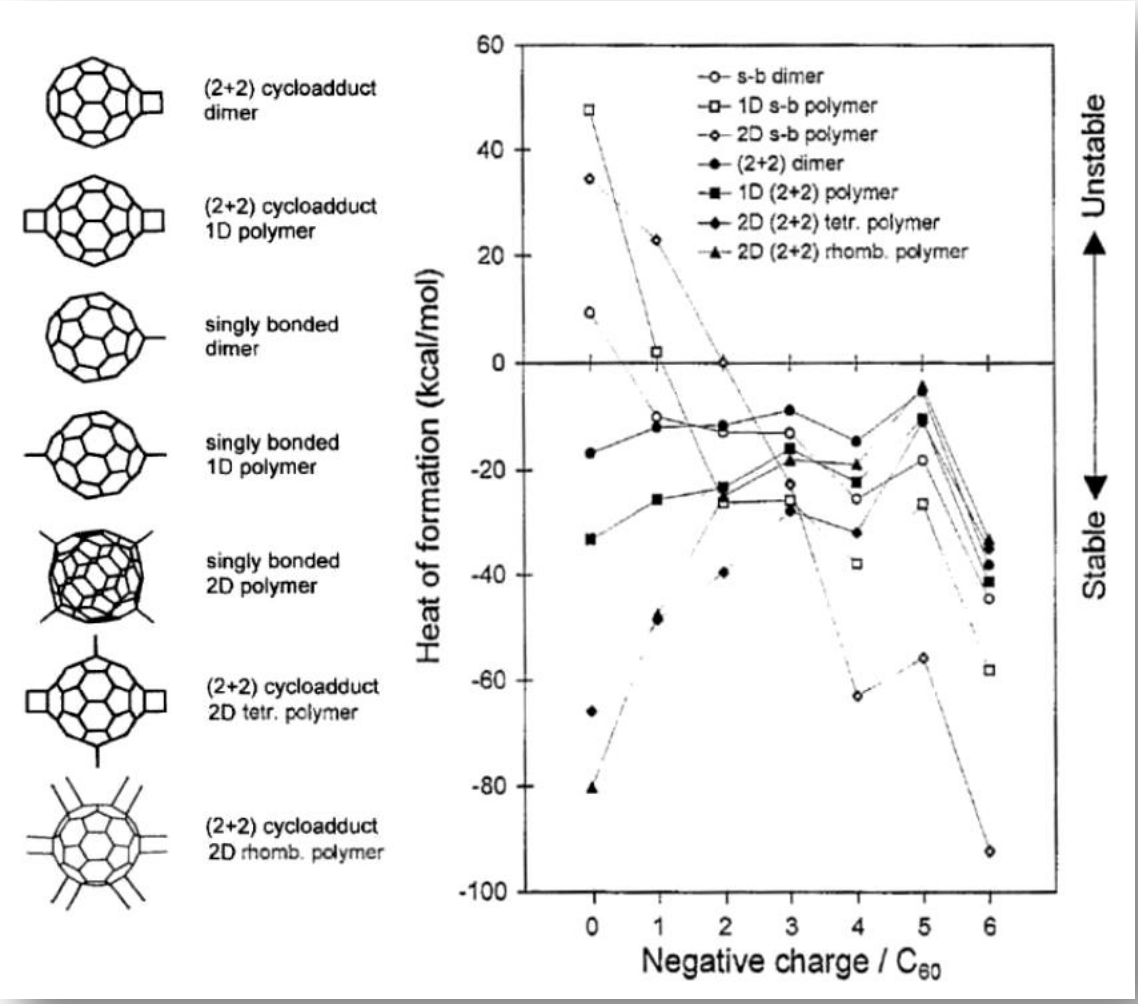

Figure 5: The enthalpy of polymerization as a function of the negative charge transfer on C_{60} for several known polymerized structures, either linked with [2+2] cycloaddition reaction or single C-C bond, calculated with thermochemical methods[32].

[29] Y. Iwasa, T. Arima, R. M. Fleming, T. Siegrist, O. Zhou, R. C. Haddon, L. J. Rothberg, K. B. Lyons, H. L. Carter, Jr., A. F. Hebard, R. Tycko, G. Dabbagh, J. J. Krajevski, G. A. Thomas, and T. Yagi, "New phases of C_{60} synthesized at high pressure", *Science* **264**, 1570 (1994).
[30] M. Nunez-Regueiro, L. Marques *et al.*, Polymerized fullerite structure", *Phys. Rev. Lett.* **74**, 278 (1995).
[31] L. Marques, M. N. Regueiro, V. D. Blank *et al*, *Science* **283**, 1720 (1999).
[32] S. Pekker, G. Oszlanyi and G. Faigel, "Structure and stability of covalently bonded polyfulleride ions in A_xC_{60}", *Chem. Phys. Lett.* **282**, 435 (1998).

In general, C_{60} polymerization can be obtained through several methods: photo-excitation, molecular collision, ionisation and combined high pressure and high temperature treatment. In particular handling C_{60} in extreme thermal and pressure conditions (T = 800 – 900 K and 2 – 5 GPa), yielded new interesting structural phases, as shown in the phase diagram below (Scheme 1).

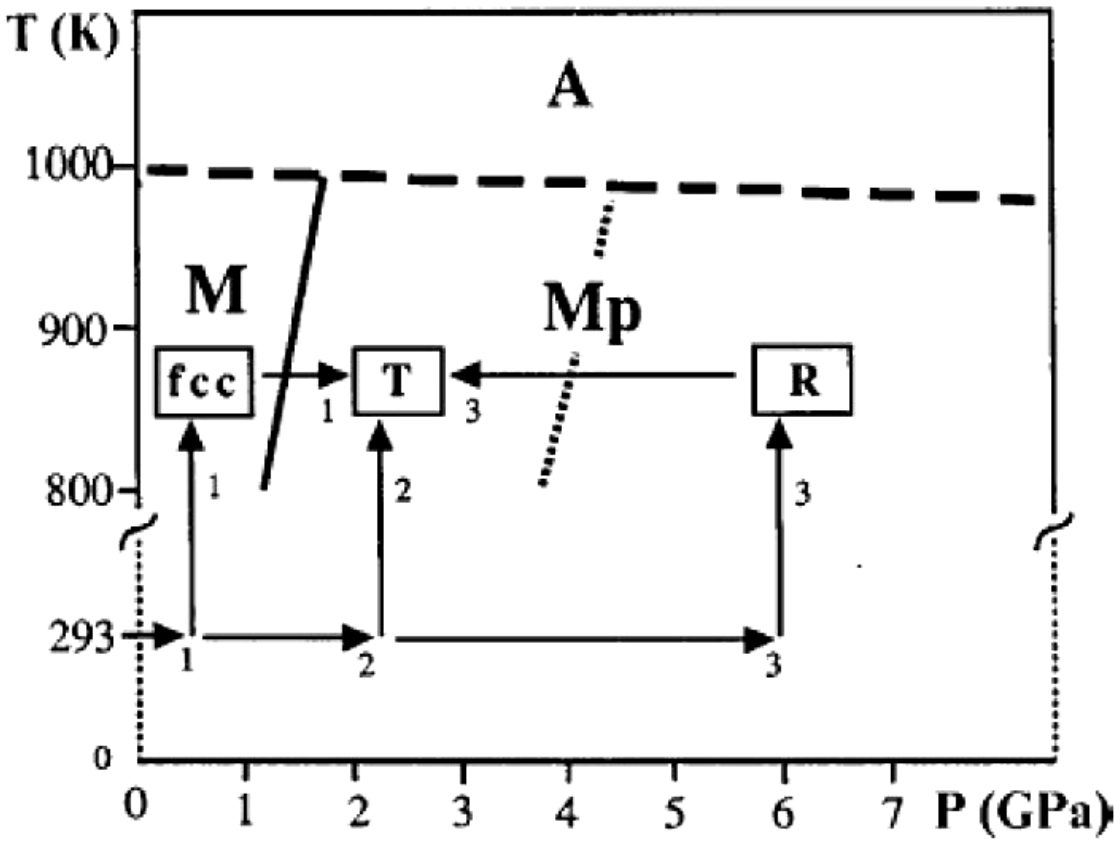

Scheme 1: Phase Diagram of pure polymerized C_{60}[33]. **A** indicates the existence range of atomic carbon due to the collapse of C_{60} cage, **M** corresponds to the monomeric state. **Mp** is the range of polymerized C_{60}, both tetragonal (**T**) and rhombohedral (**R**).

In other words it is possible to observe ferromagnetic properties of C_{60} without adding strong donors like TDAE and without treatment with iodine or hydrogen. Exposure of the C_{60} crystals to light in the presence of oxygen leads to the appearance of

[33] V. A. Davydov, H. Szwarc *et al*, "Tetragonal polymerized phase of C_{60}", *Phys Rev B* **58**, 14786 (1998).

saturating behaviour in the magnetic field with an obvious hysteresis loop[27]. The pristine Van der Waals C_{60} crystal appears diamagnetic (Figure 6, curve **a**).

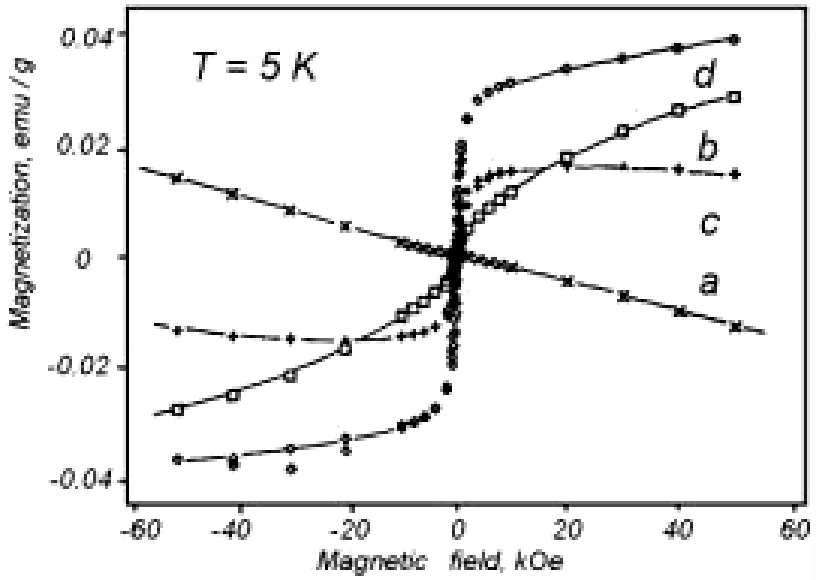

Figure 6: The field dependence of magnetization at T = 5 K for (a) pristine C_{60} crystal, (b) the sample exposed to light in oxygen for 2.5 hours (c) baked at 400 °C for 2.5 hours, and (d) exposed in air for 3 months.

The susceptibility value for the samples stored in darkness and in vacuum is practically temperature independent. The crystals are extremely oxygen sensitive, which quickly penetrates into the bulk. The paramagnetic improvement at low temperatures is always observed in the AC susceptibility of pristine C_{60} except in the case of specially prepared C_{60} single crystals, never exposed to oxygen. A different situation occurs if the sample is exposed to oxygen under the action of the visible light. The susceptibility changes its sign to positive in the whole temperature range, and its absolute value progressively increases. Exposure during 2½ hours brings noticeable features of ferromagnetism: non-linear magnetization process at low fields (Figure 6, curve **b**), and magnetization increases with the increase of the exposure time (Figure 6, curve **d**). The saturation value at high fields is $1.4 \cdot 10^{-2}$ emu/g, the remanent magnetization is about 10% of the saturated value. It is known that the physi-adsorbed oxygen can be driven away from the C_{60} crystal by heating in vacuum. Heating of the

sample, previously oxygen-exposed under the action of visible light, does not restore it to a pristine state. The most striking feature of the magnetization curves is that they remain practically unchanged from the temperature of 5 K (shown in Figure 6) to room temperature. Above 300 K the magnetization starts to decrease slowly, but remains finite up to 800 K. The saturation value $M_s = 1.4 \cdot 10^{-2}$ emu/g corresponds to approximately 10^{-3} μ_B/carbon • atom.

The experiments described in ref. 27 were repeated by another group[34], independently with respect to Y. Murakami and H. Suematsu's work. Measurements of the AC susceptibility were made on the commercial C_{60} produced by Term USA. The material was stored in darkness under a dynamic vacuum of 10^{-1} torr; In this experiments the measured saturation value for the partially polymerized sample was only $1.4 \cdot 10^{-2}$ emu/g corresponding to 10^{-3} μ_B/C_{60} referred to an exposure of one month.

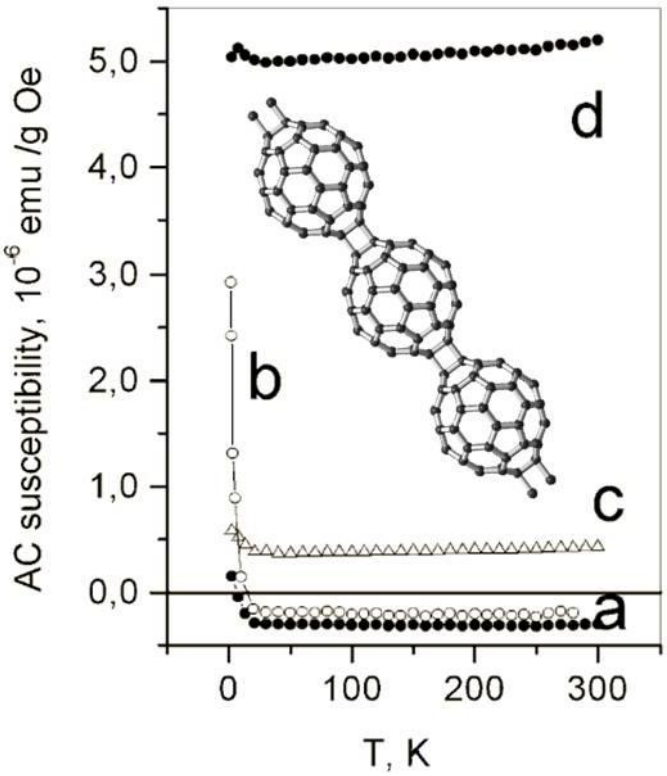

Figure 7: Susceptibility measurements for powder C_{60} sample: (a) pristine; (b) exposed to oxygen in the dark; (c, d) exposed to strong visible light in the presence of oxygen for 48 and 720 h, respectively.

[34] T. L. Makarova *et al.*, *Carbon* **41**, 1575 (2003).

The existence of a ferromagnetic phase in fullerene photopolymers was confirmed by three methods: SQUID measurements, ferromagnetic resonance and low-field nonresonance derivative EPR[35]. The room temperature value of saturation magnetization for photolyzed C_{60} was 0.04 emu/g. The experiments were done in a chamber with flowing oxygen, which exclude any possibility of penetration of metallic particles during the experiment.

1.2.5 Pressure – polymerized fullerene

It is possible to form all-carbon polymers by treating fullerenes under high pressure and high temperature conditions. The first polymerized fullerene obtained using only pressure had a rhombohedral (Rh) structure[29]. Soon after C_{60} was found to transform upon heating under pressure into three different phases: orthorhombic (O), tetragonal (T) and rhombohedral[30].

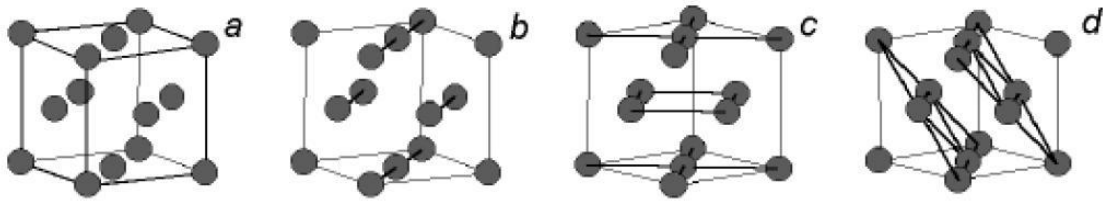

Figure 8: Transformations of fullerene C_{60} under pressure: (a): pristine *fcc* lattice, (b): orthorhombic phase, (c): tetragonal phase, (d): rhombohedral phase.

It is clear that starting from the pristine face centred cubic C_{60} lattice and for instance applying high values of pressure ($\boldsymbol{p}$) at comparatively low temperature ($\boldsymbol{T}$, less than 500 K) yields the orthorhombic (O) phase. On the other hand, combining high values of pressure and temperature ($\boldsymbol{p} > 5$ GPa, $\boldsymbol{T} > 600$ K) the rhombohedral phase becomes predominant. In the intermediate pressure-temperature range, a mixture of tetragonal

[35] F. J. Owens, Z. Iqbal, L. Belova, and K. V. Rao., *Phys. Rev. B* **69**, 033403 (2004).

and rhombohedral phases is usually formed, but it is possible to obtain a pure tetragonal phase by manipulating the preparation conditions in a pre-assigned order.

In a number of papers[36,37,38], magnetism of fullerenes polymerized by high temperature-high pressure treatment has been reported. The ref. 36 is a really important but at the same time controversial paper. In this Nature publication, Makarova *et al.* prepared a two-dimensional rhombohedral phase, which resembles highly oriented heat-treated graphite, but with layers of covalently bonded C_{60} molecules. A magnetically ordered phase with the Curie temperature of ~500 K was detected using SQUID magnetometry and the field dependent magnetic susceptibility measurements. The magnetism was attributed to the defects in the two-dimensional rhombohedral Rh-C_{60} structure. Unfortunately this paper, that has given acceptance and high resonance to magnetic carbon, has been retracted by the majority of the authors. The retraction letter[39] started with: "in this Letter we reported high-temperature ferromagnetism in a polymeric phase of pure carbon that was purportedly free of ferromagnetic impurities. Since then, however, measurements made on the same and similar samples using particle-induced X-ray emission (PIXE) with a proton microbeam have indicated that these had considerable iron content[40,41,42]. Also, polymerized C_{60} samples mixed with iron before polymerization had a similar Curie temperature (500 K) to those we described, owing to the presence of the compound Fe_3C (cementite)[24]. In addition, it has since been shown that the pure rhombohedral C_{60} phase is not ferromagnetic[43]".

On the contrary, a different method was used for the preparation of pressure-polymerized C_{60} by the group of Prof. Wood[49]: a multi-anvil octupole press at a pressure of 9 GPa. Varying the synthesis temperature, a gradual transition from paramagnetic to diamagnetic behaviour was noticed. For optimal synthesis conditions, a ferromagnetic phase with the saturation magnetization of 0.34 μ_B per fullerene cage was found. Transmission Electron Microscopy (TEM) showed that fullerenes were not

[36] T. L. Makarova, B. Sundqvist, R. Höhne, P. Esquinazi, Y. Kopelevich, P. Scharff, V. Davydov, L. S. Kashevarova, and A. V. Rakhmanina, *Nature* **413**,716 (2001).
[37] V. N. Narozhnyi, K.-H. Müller, D. Eckert, A. Teresiak, L. Dunsch, V. À. Davydov, L. S. Kashevarova, and A. V. Rakhmanina. *Physica B* **329**, 1217 (2003).
[38] R. A. Wood, M. H. Lewis, M. R. Lees, S. M. Bennington, M. G. Cain, and N. Kitamura, *J. Phys. Condens. Matter.* **14**, L385 (2002).
[39] http://www.nature.com/nature/journal/v440/n7084/full/nature04622.html.
[40] R. Höhne, & P. Esquinazi, Can carbon be ferromagnetic? *Adv. Mater.* **14**, 753–756 (2002).
[41] D. Spemann, *et al.* Evidence for intrinsic weak ferromagnetism in a C_{60} polymer by PIXE and MFM. *Nucl. Instrum. Meth. B* **210**, 531–536 (2003).
[42] K. H. Han, *et al.*, Observation of intrinsic magnetic domains in C_{60} polymer. *Carbon* **41**, 785–795 (2003); addendum **431,** 2425–2426 (2003).
[43] D. W. Boukhvalov *et al.*, Testing the magnetism of polymerized fullerene. *Phys. Rev. B* **69**, 115425 (2004).

damaged in the ferromagnetic phase and inelastic neutron scattering analysis of the magnetic phase prepared by this method showed a noticeable presence of hydrogen (H : C_{60} ≅ 17%) which can play a certain role in fullerene magnetism[44].

Pressure-polymerized fullerenes with a magnetization of about 0.5 emu/g were synthesized by another group[36]. In this work, a systematic study of the reaction conditions for the production of the ferromagnetic phase was performed. Fifteen samples were prepared at 6 GPa and the temperatures 650 ≤ T ≤ 850 °C using a "Toroid high pressure cell". Only samples prepared at 745 ≤ T ≤ 790 °C, and only some of them, namely five from the eight samples prepared at these conditions, showed ferromagnetism; their magnetic behaviour was qualitatively similar but with different values of the magnetization.

[44] J. A. Chan, B. Montanari, J. D. Gale, S. M. Bennington, J. W. Taylor, and N. M. Harrison, *Phys. Rev. B* **70**, 041403 (2004).

1.3 Room temperature ferromagnetism: Graphite

Nonmagnetic-defect-induced magnetism[45] in non-magnetic solids[46], in particular in carbon[12,47], is a hot-boiling topic today. Theories predict itinerant magnetism in graphene due to the defect-induced extended states[48] or short-range magnetic order peculiar to the honeycomb lattice[49]. Finite graphene fragments of certain shapes[50], triangles and hexagons terminated by zigzag edges[51], as well as some fractal structures[52] possess a high-spin ground state and behave as artificial ferrimagnetic atoms. Both magnetic and ferroelectric orders are predicted[53]. A defective graphene phase is foreseen to behave as a room temperature ferromagnetic semiconductor[54]. A number of nanoscale spintronic devices utilizing the phenomenon of spin polarization localized at one-dimensional (1D) zig-zag edges of graphene have been proposed[55].

These results might pave the way to nanoscale spintronics through carving the graphene; however, nobody still knows how to do it in practice.

Elementally sensitive experiments on proton bombarded graphite provided fast evidence for metal-free carbon magnetism[20]. The temperature behaviour suggests two-dimensional magnetic order[56].

The mechanism for ferromagnetism in proton irradiated graphite is essentially unknown and may result from the appearance of bound states due to disorder and the enhancement of the density of states[57] or can be induced by single carbon vacancies in

[45] A special thank to Prof. Tatiana Makarova (Umeå University, Sweden) and Prof. Pablo Esquinazi (Leipzig University, Germany) for their help in writing the "Introduction" chapter.
[46] A. L. Ivanovskii, *Phys.Usp.* **50**, 1031 (2007).
[47] T. L. Makarova in "Progress in Industrial Mathematics" Vol. 12, L. L. Bonilla et al., Eds. 467 (2007).
[48] O. V. Yazyev, L. Helm, *Phys. Rev. B* **75**, 125408 (2007).
[49] H. Kumazaki, D. S. Hirashima, *J. Phys. Soc. Jpn.*, **76**, 064713 (2007).
[50] W. L. Wang, S. Meng, E. Kaxiras, *Nano Lett.* **8**, 241 (2008).
[51] J. Fernandez-Rossier, *Phys. Rev. Lett.* **99**, 177204 (2007).
[52] O. V. Yazyev, L. Wei, S. M. Wang, E. Kaxiras, *Nano Lett.* **9**, 766 (2008).
[53] J. Fernandez-Rossier, *Phys. Rev. B* **77**, 075430, (2008).
[54] L. Pisani, B. Montanari, N. M. Harrison, *New J. Phys.* **10**, 033002 (2008).
[55] O. Y. Yazyev, M. I. Katsnelson, *Phys. Rev. Lett.* **100**, 047209 (2008).
[56] J. Barzola-Quiquia, P. Esquinazi, M. Rothermel, D. Spemann, T. Butz, N. Garcia, *Phys. Rev. B* **76**, 161403 (2007).
[57] M. A. N. Araújo, N. M. R. Peres, *J. Phys.: Condens. Matter* **18**, 1769 (2006).

a three-dimensional graphitic network[58]. The signal is inversely proportional (for both diamond and graphite) to vacancy density[59].

1.3.1 Proton bombarded graphite

Y. Kopelevich *et al.* detected ferromagnetic hysteresis loops in HOPG samples below and above room temperature[60]. This is the first experimental work that clearly shows high-temperature ferromagnetic-like behaviour and possibly superconductivity in graphite. Afterwards detailed studies have given a conclusive proof for the intrinsic nature of the ferromagnetic signal from graphite[61].

It is worth noting that irradiation effects in graphite were one major research area in the past, in particular due to its applications as a moderator in thermal nuclear reactors. Graphite is still a material used for nuclear applications owing to its low cross-section for neutron adsorption. Although that huge amount of studies on irradiation effects on graphite, their influence on the magnetic properties was only noted through the increase in the spin density and a decrease in the diamagnetism owing to the introduction of lattice defects[62]. Recently, induced magnetic order by proton irradiation was found in graphite[63,64]. The early literature on magnetism in carbon structures tends to indicate that apparently hydrogen, or anyway a light element like oxygen, plays a role in the reported ferromagnetism. In particular, the work of Murata, Ushijima, Ueda and Kawaguchi[65,66] suggests a correlation between

---

[58] R. Faccio, H. Pardo, P. A. Denis, R. Y. Oeiras, R. Yoshikawa, F. M. Araujo-Moreira, M. Verissimo-Alves, A. W. Mombru, *Phys. Rev.B* **77**, 035416 (2008).
[59] Y. Zhang, S. Talapatra, S. Kar, R. Vajtai, S. K. Nayak, P. M. Ajayan, *Phys. Rev. Lett.* **99**, 107201 (2007).
[60] Y. Kopelevich, P. Esquinazi, J. H. S. Torres, S. Moehlecke, *J. Low Temp. Phys.* **119**, 691 (2000).
[61] P. Esquinazi, A. Setzer, R. Hoehne, C. Semmelhack, Y. Kopelevich, D. Spemann, T. Butz, B. Kohlstrunk, and M. Loesche. *Phys. Rev. B* **66**,024429 (2002).
[62] B. T. Kelly, *Physics of Graphite*, Applied Science Publishers, London (1981).
[63] P. Esquinazi, D. Spemann, R. Höhne *et al.*, Induced magnetic ordering by proton irradiation in graphite, *Physical Review Letters* **91**, 227201-4 (2003).
[64] P. Esquinazi, D. Spemann, R. Höhne *et al.*, Carbon-Based Magnetism: An Overview of the Magnetism of Metal-Free Carbon-Based Compounds and Materials, Makarova, T. and Palacio, F. (Eds.), Elsevier Science, pp. 437–462, chapter 19 (2006).
[65] K. Murata, H. Ushijima, H. Ueda and K. Kawaguchi, Magnetic properties of amorphous-like carbons prepared by tetraaza compounds by the chemical vapour deposition (CVD) method, *Journal of the Chemical Society, Chemical Communications*, 1265–1266 (1991).
[66] K. Murata, H. Ushijima, H. Ueda and K. Kawaguchi, A stable carbon-based organic magnet. *Journal of the Chemical Society, Chemical Communications*, 567–569 (1992).

hydrogen concentration and magnetic order in carbon. Proton irradiation provides also measurements with the unique possibility to implant hydrogen, produce lattice defects in the carbon structure, and simultaneously have a complete elemental analysis of the sample: using PIXE method (particle-induced X-ray emission). This is a standard-free, quantitative, nondestructive multielemental analysis, which provides a 0.1–100 μg/g detection limit depending on the matrix and element to be analyzed. It requires a proton beam in the megaelectron volt energy range and it uses protons to get a map for all relevant impurity elements within a sample depth of 30 μm for a proton energy of 2 MeV in carbon.

Protons in the megaelectron volt (MeV) energy range are characterized by a penetration depth of several tens of micrometers inside a carbon structure[67]. The defect formation process by high-energy protons is a nonequilibrium process and it appears rather unlikely that ordered arrays of defects are formed by migration of interstitial carbon atoms or vacancies. According to Banhart[68] and from electron irradiation studies, the essential types of radiation damage up to intermediate temperatures are the rupture of basal planes – due to shift of the C atoms out of the plane – and the aggregation of interstitials into small dislocation loops between the graphene layers. The protuberances measured at the irradiated surface of microspots[69] result from the rearrangement of interstitials. The migration energy of the interstitial depends on whether it is bounded. Di-interstitials were proposed to explain the irradiation-induced amorphization of graphite with a migration energy of 0.86 eV[70]. The interstitial loops are stable up to rather high temperatures, probably to 1000 °C[83]. Irradiation changes the ratio of sp^2 to sp^3 bonding leading to cross-links between the graphene layers and the formation of sp^3 clusters[71]. These clusters seem to be stable and do not anneal at high temperatures. Monte Carlo simulations (Ziegler, 1977–1985) indicate that the vacancy and interstitial number produced by the H^+-MeV is about 15 times larger than the number of implanted ions. For fluencies of 0.001–75 nC • μm^{-2} Prof. Pablo Esquinazi *et al.*[63] observed in the near-surface region between $4.7 \cdot 10^{-6}$ and 0.35 displacements per carbon atom, that is, complete amorphization of HOPG

[67] D. Spemann, K. H. Han, P. Esquinazi *et al.*, Ferromagnetic microstructures in highly oriented pyrolytic graphite created by high energy proton irradiation. *Nuclear Instruments and Methods in Physical Research Section B* **219–220**, 886–890 (2004).
[68] F. Banhart, Irradiation effects in carbon nanostructures, *Reports on Progress in Physics*, **62**, 1181–1221 (1999).
[69] K. H. Han, D. Spemann, P. Esquinazi *et al.*, Ferromagnetic spots in graphite produced by proton irradiation, *Advanced Materials* **15**, 1719–1722 (2003a).
[70] K. Niwase, Irradiation-induced amorphization of graphite. *Physical Review B* **52**, 15785–15798 (1995).
[71] T. Tanabe, Radiation damage of graphite - degradation of material parameters and defect structures, *Physica Scripta*, **T64**, 7–16 (1996).

graphite for the highest fluence in agreement with recently published studies of the damage cascades by irradiation on graphite[72]. For a fluence of 75 nC • μm^{-2} they obtained 5 • 10^{11} protons/μm^2, that is, the regions where defects are created by each individual proton overlap heavily.

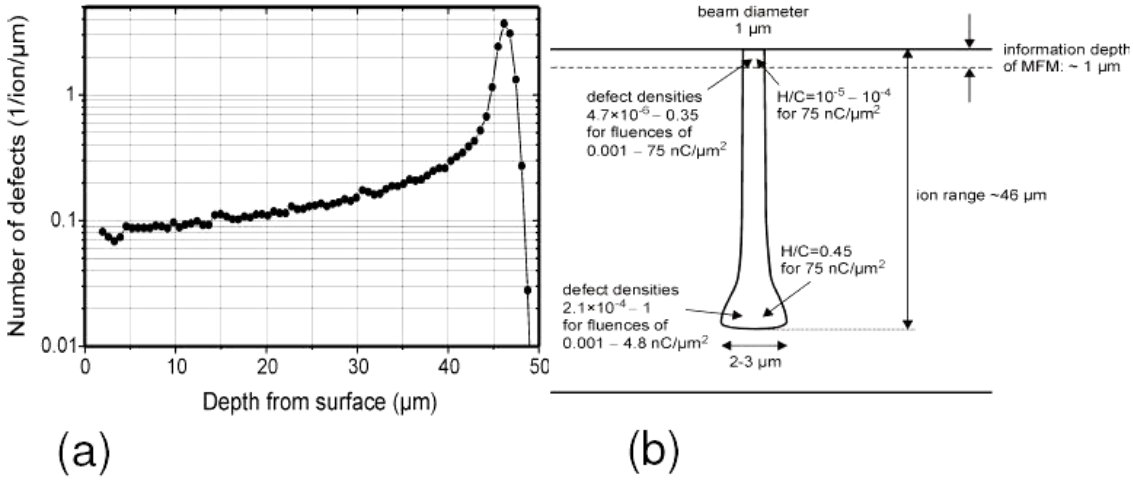

Figure 9: SRIM2003 Monte Carlo simulations for 2.25 MeV protons on HOPG. (**a**) The number of defects per ion and per μm depth interval referred to a penetration range of 46 μm. (**b**) Sketch of the modified area in graphite due to 2.25 MeV proton bombardment. The values are obtained assuming a displacement energy of 35 eV for Frenkel pairs in HOPG[69].

Also, a dangling bond at the vacancy position in the carbon structure could trap a hydrogen atom – not necessarily from the proton implantation but already present as impurity in the sample. Theoretical estimates[73] indicate that certain H-vacancy complexes as well as hydrogen bonded to carbon adatoms (just above a graphene layer) have a magnetic moment; each hydrogen would provide an average magnetic moment of ~1 μ_B.

[72] H. Abe, H. Naramoto, A. Iwase and C. Kinoshita, Effect of damage cascades on the irradiation-induced amorphization in graphite. *Nuclear• Instruments and Methods in Physical Research Section B*, **127/128**, 681–684 (1997).
[73] P. O. Lehtinen, A. S. Foster, Y. Ma *et al.*, Irradiation induced magnetism in graphite: a density-functional study, *Physical Review Letters* **93**, 187202-4 (2004).

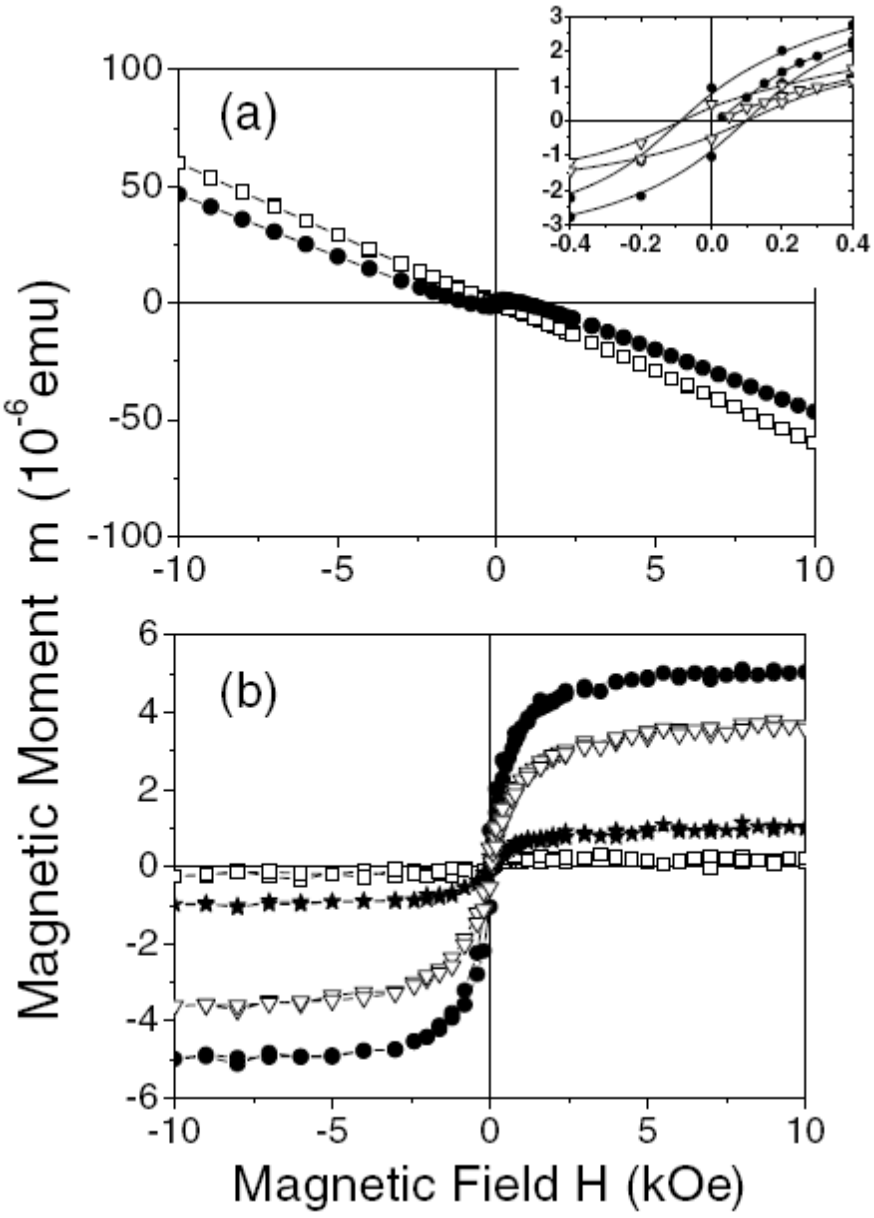

Figure 10[74]: The magnetic moment measured at T = 300 K as a function of magnetic field (1 kOe = 10^6 / 4π Am^{-1}) by cycling the field from zero to +10 kOe, from +10 kOe to -10 kOe, and back to -10 kOe for a sample glued on a silicon substrate, after various proton irradiations. **(a)** Total magnetic moment without any background subtraction for the sample after stages No. 1 (□, homogeneous irradiation of an area 1720 x 1720 μm^2, dose: 0,99 pC / μm^2, total charge: 2,93 µC (proton current I = 1,6 nA)) and No. 3 (●, four spots of 0.8 mm diameter each, dose: 0:3 nC / μm^2, total charge: ≈ 600 µC (2 MeV, I = 350 nA)) irradiations. **(b)** Magnetic moment after subtraction of the sample holder magnetic moment, for the sample after the first (□), second (*, 100 x 100 spots of 2 µm diameter each, on an area 570 x 570 μm^2 in the middle of the sample, dose: 0,3 nC / μm^2, total charge: ≈ 8 µC (I = 1,6 nA)), third (●), and fourth (Δ,

[74] P. Esquinazi, D. Spemann, R. Höhne *et al.*, Induced magnetic ordering by proton irradiation in graphite. *Physical Review Letters* **91**, 227201-4 (2003).

the same as No. 3 (2 MeV, I = 200 nA)) irradiation stages. The inset in (a) shows a smaller field region of the hysteresis loops after the third and fourth irradiation stages.

It is also possible to "magnetically write" on a graphite surface, using a proton microbeam of energy in the megaelectron volt range directed onto the HOPG surface parallel to the c axis of the sample without beam scanning (excepting line scans, see the following text), leading to the formation of micron-sized spots with enhanced defect density, as measured by micro-Raman[75,76]. With an MFM one can measure the phase change of the, eventually magnetic, signal on the spots (see Figure 11).

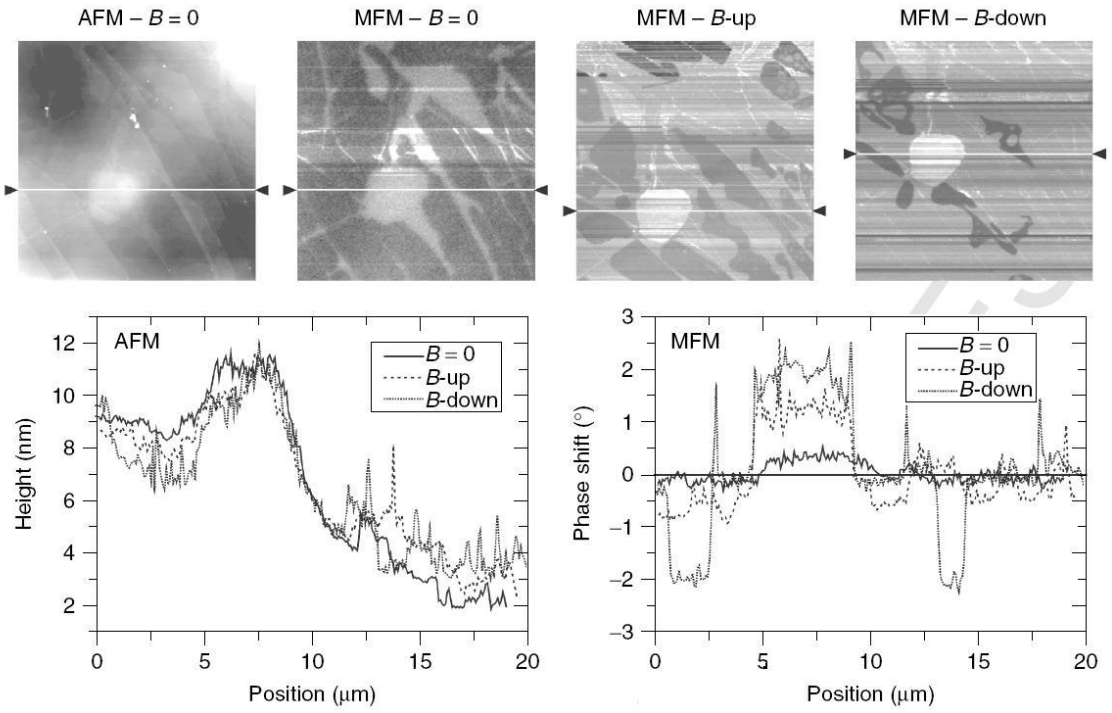

Figure 11: AFM (top left) and MFM images (scan size: 20 × 20 μm²) for a 2 × 2 μm² spot irradiated with 2.25 MeV protons at a fluence of 7.5 × 10^{16} cm^{-2} ~ 0.115 nC μm². The reported AFM and MFM line scans were extracted from the images as indicated by the black triangles. The images show the

[75] R. Höhne, P. Esquinazi, K. H. Han *et al.*, Ferromagnetic structures in graphite and amorphous carbon films produced by high energy proton irradiation, *Proceedings of the 16 International Conference of Soft Magnetic Materials*, Raabe, D. (Ed.), pp. 185–190 (2004a) (ISBN 3-514-00711-X).
[76] P. Esquinazi, D. Spemann, R. Höhne *et al.*, Carbon-Based Magnetism: An Overview of the Magnetism of Metal-Free Carbon-Based Compounds and Materials, Makarova, T. and Palacio, F. (Eds.), Elsevier Science, pp. 437–462, chapter 19 (2006).

results of the spot measured after irradiation ($B = 0$), after exposing it to a field of ~1 kOe in the c direction (B-up) or $-c$ direction (B-down) . The measurements were done, however, at zero applied field.

However, in those measurements the influence of electric potential differences (e.g., difference in contact potentials – work functions – between tip and sample surface or circuit induced potential differences) was not taken into account and appropriately checked. Therefore, one may doubt the estimated values as well as the magnetic origin of the phase contrast at and in the surroundings of an irradiated spot till clear evidence from other experimental techniques is obtained. Nevertheless, a clear evidence of the intrinsic carbon magnetism came from X-ray Magnetic Circular Dichroism absorption measurements at proton-irradiated spots produced on 200-nm-thick carbon films. Hence, using element specific XMCD they have demonstrated that proton irradiation leads to ferromagnetic order in carbon that originates from the spin polarization of the carbon π-electrons[20]. In Ref. 20 the scanning transmission x-ray microscope (STXM) located at the elliptical polarizing undulator beam line 11.0.2 at the Advanced Light Source in Berkeley, California (USA) was employed. This x-ray source provides intensive soft x-ray beams with variable polarization. The STXM uses a Fresnel zone plate to focus the incoming soft x-ray beam to a spot of about 50 nm onto the sample in normal incidence. Soft x-ray absorption microscopy makes it possible to obtain element specific information in a complex sample by tuning the photon energy of the x rays to the core level absorption resonance of each element. The exact shape and intensity of such an absorption resonance depends strongly on the local electronic structure of the investigated species and composition of the sample[77]. In addition, the polarization dependence of the absorption resonance (dichroism) carries information about the magnetic order: this effect is called x-ray magnetic circular dichroism (XMCD) and is used to quantify the magnetic moment of different elements in a sample.

[77] J. Stöhr, *NEXAFS Spectroscopy*, Springer Series in Surface Sciences Vol. 25 (Springer, Heidelberg, 1992).

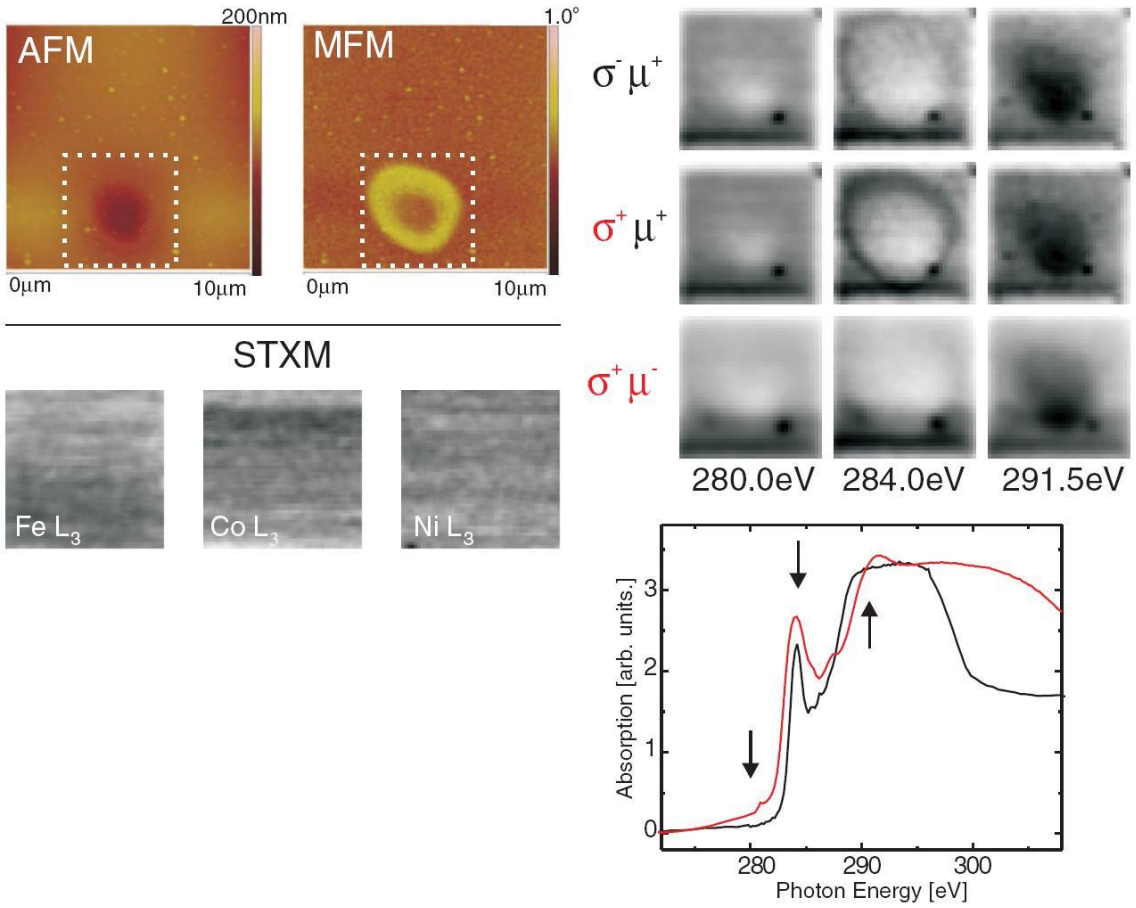

Figure 12: Left) on the top are reported AFM and MFM images of a spot irradiated with a 2.25 MeV proton beam and a fluence of 50 nC / µm2. The AFM image reveals the beam impact area. A line scan through its centre reveals a deepening of about 70 nm depth in 5 µm distance. The MFM image suggests a magnetic "ring" around the impact area. On the bottom an STXM images at the Fe, Co, and Ni absorption resonance obtained from the area marked with a dotted line in the force microscopy images above: notice that no contamination is found within the impact area. Right) Carbon K-edge absorption spectrum (bottom) obtained from a sample prepared at room temperature (black) and at 560°C substrate temperature (red). The arrows indicate the photon energies for which the STXM images (top) in the corresponding columns were acquired for a spot irradiated at 50 nC/µm². The helicity (σ) of the x-rays was reversed between the first and the second row of images. For the third row the direction (µ) of the applied field was reversed as well so that both polarization and applied field are opposite to the situation in the first row. Images acquired at the π* resonance (284.0 eV) exhibit a clear XMCD signal.

To shed more light on the nature of the HOPG magnetism, Esquinazi *et al.* used the novel low-energy muon spin rotation (LE-μSR) technique[78]. μSR is a high-sensitivity magnetic local probe technique which can detect magnetic moments as small as 10^{-3} - 10^{-4} μ_B. In a μSR experiment, an ensemble of nearly 100% spin-polarized muons is implanted in the sample. The muons stop and precess around the local magnetic field. The time evolution of the spin polarization (or asymmetry) of the muon ensemble (μSR signal) is monitored by detection of anisotropically emitted decay positrons. From this, valuable information regarding the intensity, directionality and dynamics of the internal magnetic fields can be deduced. LE-μSR advantages include: (a) insensitivity to small contaminations of any kind, since the contribution from each magnetic phase is weighted by its magnetic volume fraction. (b) microscopic depth selectivity, and (c) ability to measure at zero applied field.

Low-energy muon spin rotation and SQUID magnetization measurements were performed on proton-irradiated and non-irradiated highly oriented pyrolytic graphite samples. confirming that the surface magnetism were intrinsic and not due to irradiation[79].

1.4 Room temperature ferromagnetism: an overview of striking results

Hydrogenation of carbon materials can induce magnetism through termination of nanographite ribbons[80], adsorption on the CNT external surface[81], trapping at a carbon vacancy or pinning by a carbon adatom on CNTs[82]. A glassy carbon prepared by high pressure treatment was studied in refs. 83 and 84: Room-temperature ferromagnetic loops in a narrow range of synthesis conditions (5 GPa, 1200 °C) was

[78] E. Morenzoni, H. Glückler, T. Prokscha, R. Khasanov, H. Luetkens, M. Birke, E. M.Forgan, Ch. Niedermayer, M. Pleines, *Nucl. Instrum. and Methods B* **192**, 254 (2002).
[79] M. Dubman, T. Shiroka, H. Luetkens, M. Rothermel, F. J. Litterst, E. Morenzoni, A. Suter, D. Spemann, P. Esquinazi, A. Setzer, and T. Butz, *Join European Magnetic Symposia (JEMS08)*, to be published in JMMM.
[80] K. Kusakabe and M. Maruyama, *Phys. Rev. B* **67**, 092406 (2003).
[81] X. Y. Pei, X. P. Yang, and J. M. Dong, *Phys. Rev. B* **73**, 195417 (2006).
[82] Y. C. Ma, P. O. Lehtinen, A. S. Foster, and R. M. Nieminen, *Phys. Rev. B* **72**, 085451 (2005).
[83] X. Wang, Z. X. Liu, Y. L. Zhang, F. Y. Li, and C. Q. Jin, J. Phys.: *Condens. Matter.* **14**,10265 (2002).
[84] C. Q. Jin, X. Wang, Z. X. Liu, Y. L. Zhang, F. Y. Li, and R. C. Yu, *Braz J. Phys.* **33**, 723 (2003).

recorded. Also, high-temperature ferromagnetism has been found in microporous carbon with a three-dimensional nanoarray zeolitic structure[85].

Studies of carbon particles prepared in He plasma[86] showed that the saturation magnetization of carbon fine particles increases with decreasing grain size. The highest Ms = 8.5·10-7 Wb·m/kg (0.67 emu/g) has been obtained for the grain size of 19 nm; the intensities of Fe, Co, and Ni lines were comparable to the noise level in EPMA analysis. The saturation magnetization deceases gradually with increasing temperature and disappears at a temperature of 607 K. The strong dependence of saturation and remanent magnetization and coercive force on grain size of the powder was observed earlier in PYRO-pan powder: Ms, Mr and Hc grow by a factor more than ten with decreasing average grain size of the powder from 45 to 5 μm.

Carbon nanofoam is sometimes called the fifth carbon allotrope. As first observed by Rode *et al.*[87], it exhibits room-temperature ferromagnetic behaviour. Freshly produced, it shows rather high saturation magnetization 0.4 emu/g at room temperature. The high temperature magnetization disappears in a few hours after synthesis but persists at lower temperatures with a narrow hysteresis curve and a high saturation magnetization.

Multilevel ferromagnetic behaviour has been described[88] for chemically modified graphite: powdered graphite mixed with powdered copper oxide and then heated in a tube furnace containing either nitrogen or argon. Two magnetic transition were observed, at 115 and 315 K. Iron content was determined by AAS, XRF and EDS to be around 40–60 ppm range, Ni and Co around 1 ppm, The Ms values are 0.58 and 0.25 emu/g at 2 and 300 K correspondingly. The simple and inexpensive chemical route, based on a vapour phase reaction, to obtain ferromagnetic graphite in bulk amounts was accepted as the state patent in 2004[89].

[85] Y. Kopelevich, R. R. da Silva, J. H. S. Torres, A. Penicaud, and T. Kyotani, *Phys. Rev. B* **68**, 092408 (2003).
[86] S. Akutsu and Y. Utsushikawa, *Mater. Sci. Res. Int.* **5**, 110 (1999).
[87] A. V. Rode, E. G. Gamaly, A. G. Christy, J. D. Fitz Gerald, S. T. Hyde, R. G. Elliman, B. Luther-Davies, A. I. Veinger, J. Androulakis, and J. Giapintzakis, *Phys. Rev. B* **70**, 054407 (2004).
[88] A. W. Mombrú, H. Pardo, R. Faccio, O. F. de Lima, A. J. C. Lanfredi, C. A. Cardoso, E. R. Leite, G. Zanelatto, and F. M. Araújo-Moreira, *Phys. Rev. B* **71**, 100404(R) (2005).
[89] H. Pardo, A. Mombrú, and F.M. Araújo-Moreira, *Patent PI* 0402338-2 (2004).

Results and Discussion

2.1 Introduction

During the PhD research activity period, all the work has been focused on the synthesis of potential new room temperature carbon based ferromagnets, following substantially the two main systems described in the previous chapter. In particular we managed to synthesise new fullerene polymers in particular donor/acceptor intercalated C_{60} which arrange into novel polymeric structures and on the other hand we performed neutron irradiation on graphite samples in order to induce bulk ferromagnetic order in completely organic systems.

2.2 Ferromagnetism in C_{60} polymers

During the last years, as it is already cited in the Introduction chapter, the scientific interest in polymerised fullerenes strongly increased, due to the publication of numerous experimental works, which claimed room-temperature ferromagnetic order in some of these systems. However, the most important paper regarding room-temperature ferromagnetism in pressure polymerised rhombohedral C_{60}, was then retracted, since the cause of the ferromagnetic signal turned out to be extrinsic, namely due to a relevant magnetic impurities contamination[24,36]. Nevertheless, the possibility of the existence of magnetic order in such carbon based systems even at room temperature is still debated and polymeric fullerenes continue to be subject of intense research[90,91].

[90] A. N. Andriotis, R. M. Sheets, M. Menon, *Phys. Rev. B* **74**, 153403 (2006).
[91] D. W. Boukhvalov and M. I. Katsnelson, cond-mat: arXiv:0712.2928v1 (2007).

2.2.1 Hole doped C_{60} polymers: $C_{60}(AsF_6)_2$

The C_{60} molecule, thanks to its remarkable redox stability, gives rise to the fullerides upon electron doping. The electron properties of these compounds arise from the LUMO-derived band, since C_{60} is in the anionic form. In analogy a very interesting research perspective was identified in a new class of C_{60} derivatives, the Fullerenium salts where fullerenes are in the oxidised state. In this case the HOMO-derived band may assume a leading role in the determination of the electronic properties. The first compound belonging to such a new class of C_{60} based materials has been synthesized in our research group, working on strongly correlated, carbon-based, molecular materials. The fullerene molecule, in this case, is present for the first time in the solid state, in its oxidized form C_{60}^{2+}. A theoretical investigation of the magnetism in C_{60} isolated ions has been performed by Lüders *et al.*[92,93] in order to shed more light on the possible analogies or differences between the negative C_{60}^{n-} and the positive C_{60}^{n+} ions. The ground-state spin for the charge states ranging from -3 to +5 has been computed taking into account the electron-electron and electron-vibration interactions. The former, through the Coulomb exchange, promotes the molecular Hund's rule magnetism; on the contrary, the latter through the Jahn-Teller distortions favours the spin pairing providing an energy gain for the low spin states and, thus, quenching the magnetism. In particular previous hints can be found in the literature[94,95] outlining how for C_{60}^{n-} ions the contribution from JT interaction is expected to overcome the Coulomb exchange leading the C_{60}^{2-} ion, as well as C_{60}^{4-} to be non magnetic. On the contrary, the results reported predict the ion C_{60}^{2+} to be magnetic being its ground state with spin S=1, 30 meV lower in energy than the spin state S=0. Although this prediction can not be straightforward extended to the solid state compounds, it represents a strong input in the investigation of the magnetic property of the

[92] M. Lüders, A. Bordoni, N. Manini, A. D. Corso, M. Fabrizio, and E. Tosatti, Coulomb couplings in positively charged fullerene, *Philosophical Magazine B* **82**, 1611(2002).
[93] M. Lüders, N. Manini, P. Gattari, and E. Tosatti, Hund's rule magnetism in C_{60} ions, *The European Physical Journal B* **35**, 57 (2003).
[94] A. Auerbach, N. Manini, and E. Tosatti, Electron-vibron interactions in charged fullerenes. I. Berry phases, *Physical Review B* **49**, 12998 (1994).
[95] N. Manini, E. Tosatti, and A. Auerbach, Electron-vibron interactions in charged fullerenes. II. Pair energies and spectra, *Physical Review B* **49**, 13008 (1994).

fullerenium salt $C_{60}(AsF_6)_2$, since, for the first time in this case the C_{60}^{2+} cation can be studied in the solid state.

In spite of the difficulty in synthesizing such a compound, the feasibility of stabilising the C_{60} dication in the solid state is however confirmed by cyclic voltammetry which clearly shows at least three reversible oxidation states in the fullerene molecule [96].

The Fullerenium salt $C_{60}(AsF_6)_2$ synthesis[97,98,99,100] is based on the reaction between pentafluoroArseniate (AsF_5) as a very oxidant gas and the fullerene molecule in liquid SO_2 (dried over CaH_2) as non-nucleophilic solvent.

C_{60} molecule were inserted in a schlenk vial using a Glove Box (moisture and oxygen concentration lower than 2 ppm), then the reaction took place in a 3 stages glass reactor in order to avoid any air/water contamination (see

Scheme **2**) by suspending C_{60} in liquid SO_2 where the gaseous AsF_5 is soluble.

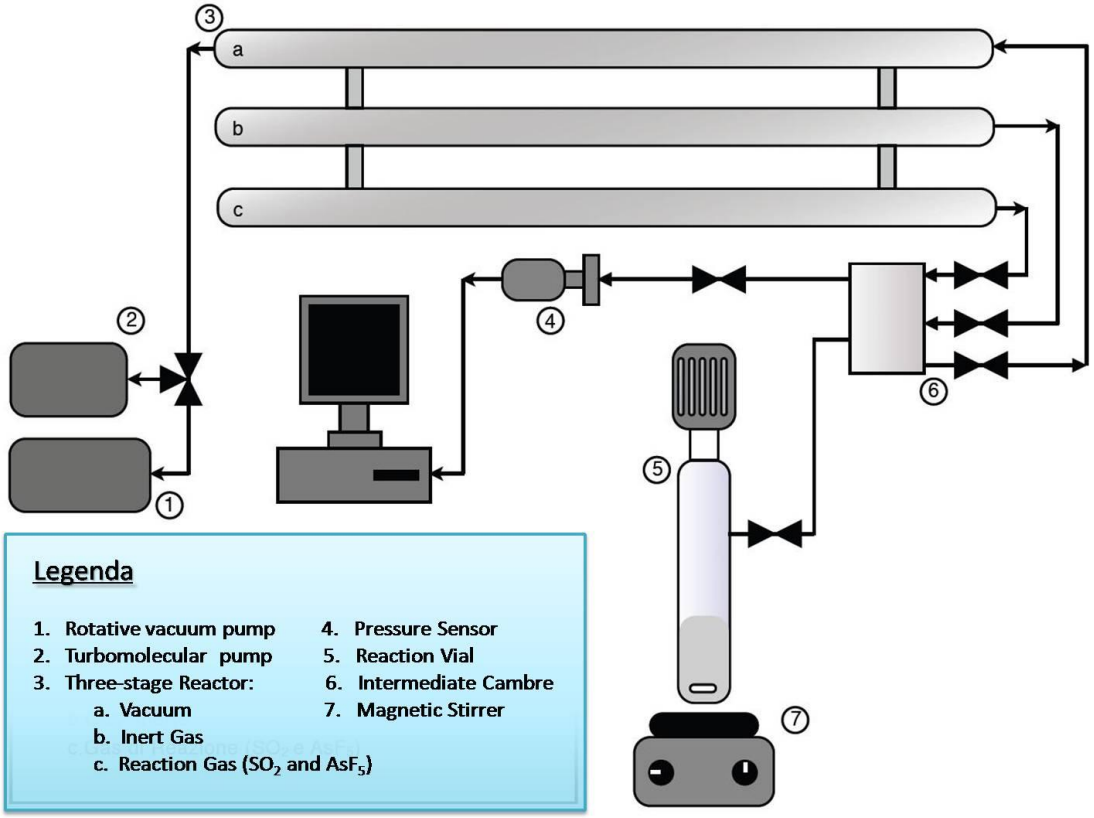

[96] C. Bruno *et al., J. Am. Chem. Soc.* **125**, 15738 (2003).

[97] W. R. Datars, T. R. Chien, R. K. Nkum, and P. K. Ummat, , Intercalation of AsF_5 in C_{60}, *Physical Review B* **50**, 4937 (1994).

[98] W. R. Datars, J. D. Palidwar, and P. K. Ummat, Identification of acceptors in C_{60}, *Journal of Physics and Chemistry of Solids* **57**, 977 (1996).

[99] W. R. Datars and P. K. Ummat, Identification of AsF_6^- in C_{60}, *Solid State Communications* **94**, 649 (1995).

[100] Evolution of the preliminary PhD work of dr. Massimo Pagliari and dr. Fabio Gianferrari.

Scheme 2: Three stage glass reactor employed in the synthesis of $C_{60}(AsF_6)_2$.

In particular, the Lewis superacid AsF_5 oxidizes the fullerene molecule and generates by disproportionation through charge transfer, the anion AsF_6^- which is also sufficiently inert and non-nucleophilic to avoid the covalent attach of the fullerenium ion.

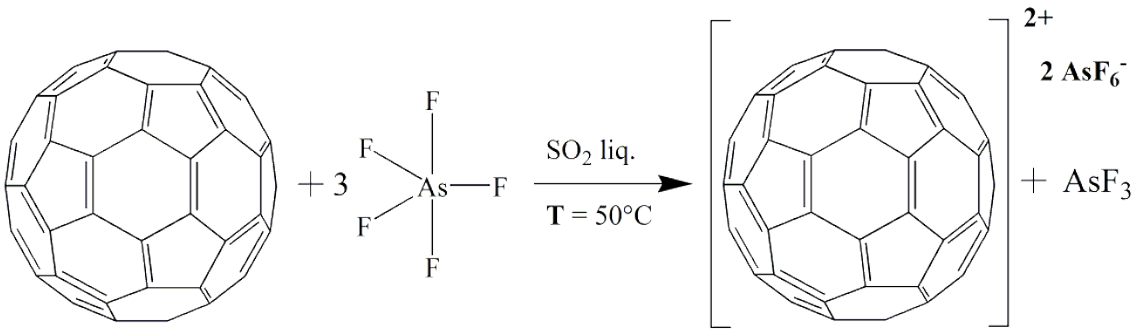

Scheme 3: Fullerenium salt reaction scheme.

The glass reactor is connected with a pressure sensor which allows stoichiometric gas additions to the reaction solution. The stoichiometric amount of AsF_5 (in ratio 1:3) is condensed on the C_{60} powder in a suspension of liquefied SO_2 at 77 K. After a 15 hours heterogeneous reaction the liquid SO_2 is thermally evaporated and neutralized in a NaOH solution.

Figure 13: Fullerene salt experimental setup.

Both elemental analysis and density measurements[100], performed with a home-built gas picnometer, confirmed the stoichiometry $C_{60}(AsF_6)_2$. Then, we carried out accurate structural investigation by using synchrotron radiation powder diffraction[101] at room temperature (ESRF, Grenoble). Almost all the peaks of the powder diffractogram were indexed with an orthorhombic cell (a = 10.4469(5) Å, b = 9.9913(8) Å, c = 32.050(2) Å, spatial group *Imma*), thus confirming the purity of the synthesised product. The lattice appeared profoundly changed if compared to the high symmetric cubic arrangement of pristine C_{60}; moreover, the correct structural model of this compound has been achieved using the *simulated annealing* algorithm. This calculation indicated that in $C_{60}(AsF_6)_2$ the minimum distance of two neighbours C_{60} is just ~ 9 Å, a value strongly suggesting the polymerisation of the molecules. Synchrotron data Rietveld refinement confirmed the 1D polymeric nature of the fullerenium salt (see Figure 14, left picture); in particular, the fullerene chains propagate along the a-axis direction, in form of unusual zigzag chains, with neighbouring C_{60} units forming an angle of ~ 72°.

[101] A special thank to Dr. Daniele Pontiroli for structural characterizations (XRD analysis and refinements).

The bonding architecture consists in an alternating sequence of [2+2] cycloaddition bridges and single C-C bonds, as shown in Figure 14 (right picture). It is important to direct the reader's attention to this particular 1D polymeric arrangement which has never been observed before in other fullerene compounds[102].

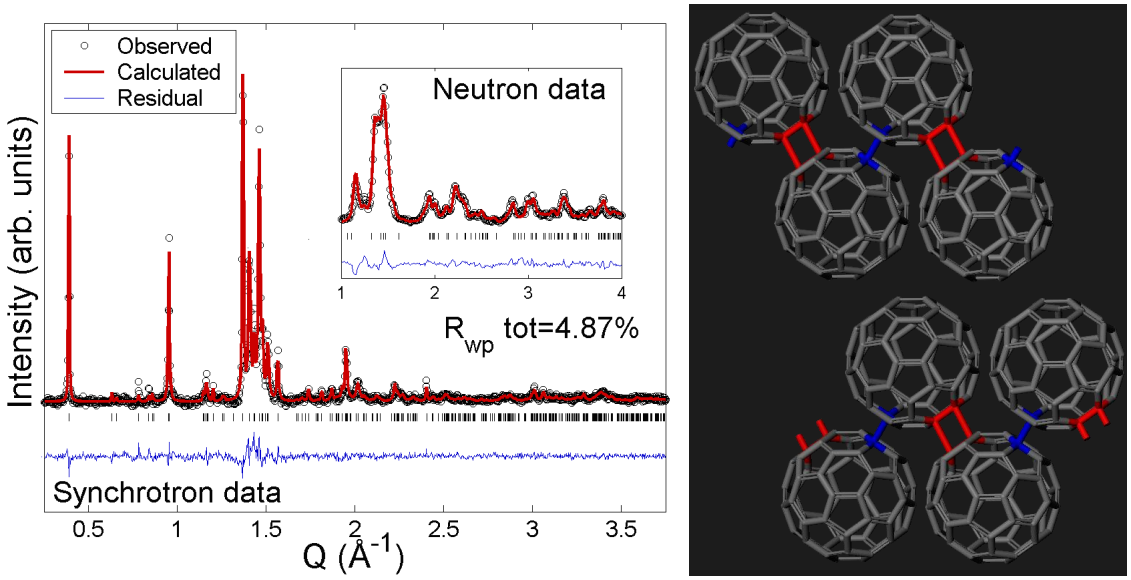

Figure 14: *Left)* Observed (o) and calculated (solid red line) powder diffraction pattern of $C_{60}(AsF_6)_2$ at 300 K, both from synchrotron and neutron diffraction data. *Right)* The 1D polymeric structure of $C_{60}(AsF_6)_2$, consisting in polymeric chains connected alternatively by single C-C bonds and four-membered carbon rings.

Furthermore, chemical stability of the fullerenium salt was proved through a controlled sample thermal annealing, contemporary monitoring the structural evolution. The compound underwent a depolymerisation transition which was completed above T ~ 475 K.

This transition was accompanied by gas emission – probably AsF_3 generated by anion decomposition – and yielded a new monomer *fcc* phase (see Figure 15), which was preserved on cooling (irreversible phase transition). Even if this phase is currently under study, we suggest that the cubic structure should correspond to a stable charge-transfer salt, in which fullerene units are in the oxidised state C_{60}^{+}.

[102] A. Goffredi, M. Pagliari, D. Pontiroli, T. Shiroka, M. Belli, F. Gianferrari, G. Zandomeneghi and M. Riccò, *manuscript in preparation.*

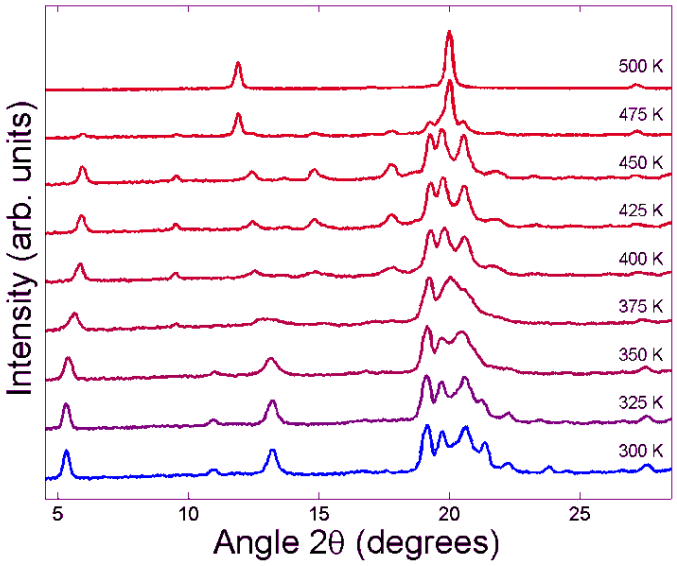

Figure 15: Thermal stability of the fullerenium salt $C_{60}(AsF_6)_2$. The polymeric phase disrupts above ~ 450 K and undergoes an irreversible polymer-to-monomer transition, by the contemporary emission of gas. The monomer phase is face centred cubic and persists on cooling the sample.

In spite of the unconventional electronic properties expected from a fullerenium salt, SQUID magnetic measurements were performed on both the polymer and the monomer phase. However, no significant electronic and magnetic properties were found. The samples are substantially diamagnetic (see Figure 16); the presence of superimposed paramagnetic signal, which follows the Curie-Weiss law, is easily explained with a small amount of paramagnetic impurities. The absence of magnetism in these compounds is still an open question and is currently under investigation.

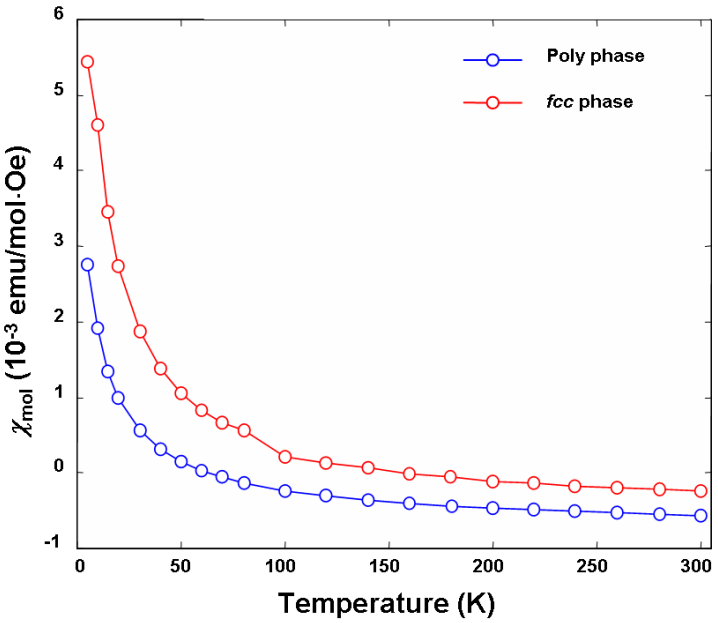

Figure 16: Magnetic SQUID measurements performed on the fullerenium salt in the polymeric state (curve in blue) and after the polymer-to-monomer transition (curve in red). In both cases, the samples show essentially a diamagnetic behaviour, with a small superimposed Curie-Weiss contribution arising from paramagnetic impurities and corresponding respectively to 0.14 and 0.25 ½ spin per C_{60}.

2. 3 Mg_5C_{60} Polymer

Following the open but at the same time controversial path of magnetic polymerized fullerenes, we improved a new synthetic method of an alkali earth ion doped fullerene that is expected to be a C_{60} polymer.

Recent studies indicate that the compound Mg_4C_{60} is a 2D polymer with a rhombohedral network, similar to what observed in pressure polymerised C_{60}[103], except for the bonding architecture, which, in this case, was proposed to be constituted by single C-C bonds. This compound also displayed rather interesting features, such as metallic behaviour and an exceptional thermal stability, up to 800 K[104].

However, the interest on such compounds was so far reduced, mainly because of synthetic problems. In fact, metallic Mg intercalation in C_{60} through standard

[103] F. Borondics *et al.*, *Sol. State Comm.* **127**, 311 (2003).
[104] D. Quintavalle, F. Borondics, G. Klupp, A. Baserga, F. Simon, A. Jánossy, K. Kamarás and S. Pekker, *Phys. Rev. B* **77**, 155431 (2008).

methods, based on the thermal diffusion of the alkali-earth vapours in the fullerene lattice, required up to one month's reaction time, because of the relatively low vapour pressure of Mg also at high temperatures.

The intercalation of small Mg ion has been successfully obtained by our group with a completely new synthetic path, based on a thermal decomposition of a metallorganic precursor mechanically mixed to C_{60} (see Scheme 5).

In particular we performed a one-pot synthesis of the organometallic complex $MgAnt(THF)_3$ by reacting Mg, previously activated with dibromoethane, with a stoichiometric amount of Anthracene powder (Alfa-Aesar, 99%) in Tetrahydrofuran (THF dried over $LiAlH_4$) at room temperature.

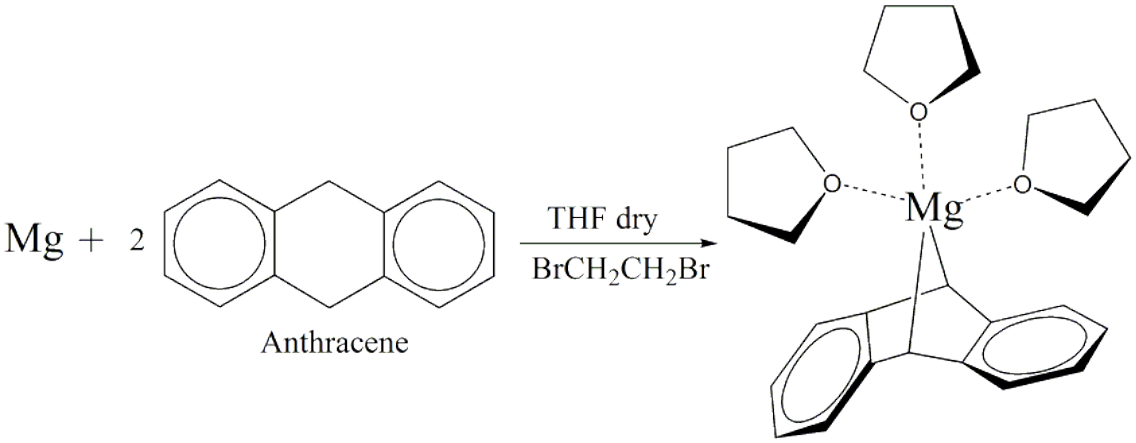

Scheme 4: $MgAnt(THF)_3$ synthetic scheme.

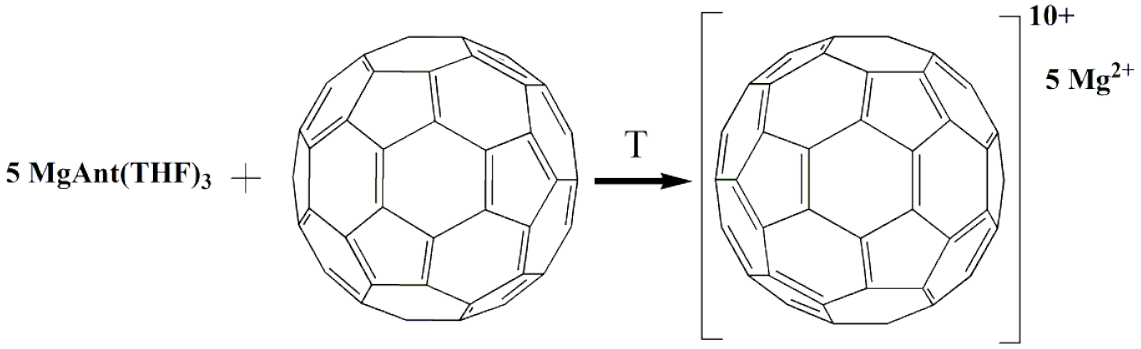

Scheme 5: $Mg_{x=4-5}C_{60}$ polymer synthetic scheme. To notice that the stoichiometry of this compound has not been completely investigated. All presented data are preliminary results.

This new method drastically reduces the reaction time, without decreasing the crystallinity of the product.

Preliminary laboratory diffraction analysis was performed on these sample. While the structure proposed by Borondics[103] indicates the compound as a 2D polymer with single bonds established between fullerene units, we suggest that the structure should be indeed a 2D polymer, but with [2+2] cycloaddiction intermolecular bridges ($dist_{C60}$ = 9.25 Å). In fact, such a polymer arrangement, similar to Rh-C_{60}, seems not to be compatible with this model, since, in this case, the structure would result extremely tensioned.

Samples obtained with this method, with the nominal stoichiometry Mg_5C_{60}, underwent preliminary synchrotron radiation powder diffraction (ESRF, Grenoble), in which the peaks corresponding to the rhombohedral polymer phase were clearly observed (see Figure 17). The lattice parameters obtained with the Le Bail Pattern decomposition (spatial group *R-3m*, a = 9.227(7) Å, c = 25.20(2) Å, γ = 120°) agree with the structure proposed by Borondics *et al.*[103].

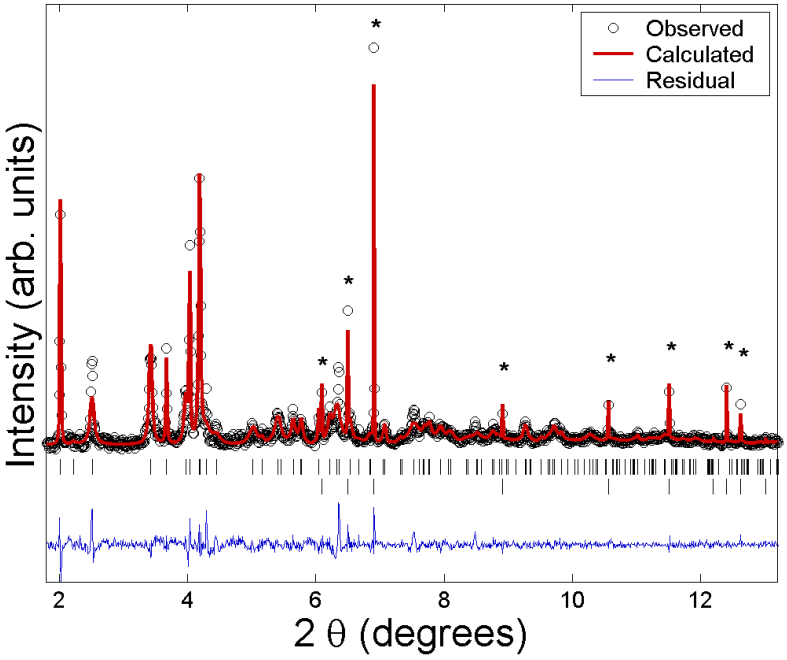

Figure 17: Observed (o) and calculated (solid red line) powder synchrotron diffraction pattern of Mg_5C_{60} measured at 300 K (Le Bail analysis). The compound arranges in a rhombohedral lattice, where inter-fullerene distances are compatible with 2D polymerisation. The peaks marked with asterisks are due to unreacted Mg (Rwp = 9.89 %).

Some of the diffraction peaks could be ascribed to the presence of unreacted Mg, thus suggesting that a line-phase could exist in this class of compounds, containing a less amount of magnesium. Further work is required in order to precisely describe the structural properties of this polymer.

Preliminary magnetic SQUID measurements performed on Mg_5C_{60} indicated the absence of any kind of magnetic order in this compound, down to 5 K (see Figure 18). The signal essentially consists of a Curie-Weiss temperature dependent contribution, arising from a small amount of paramagnetic impurities, superimposed to a Pauli constant and temperature independent baseline, which could arise from the presence of unreacted Magnesium.

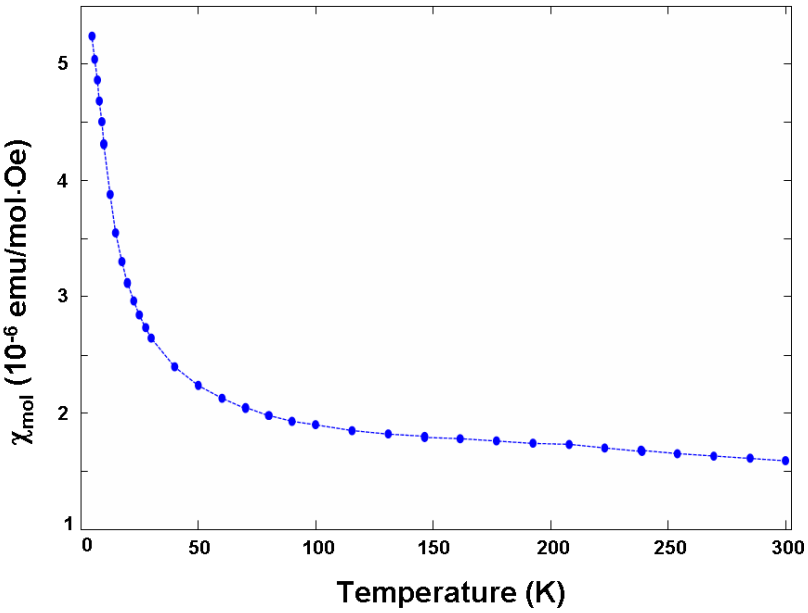

Figure 18: Magnetic SQUID measurement performed on Mg_5C_{60}. A small Curie-Weiss contribution, due to the presence of paramagnetic impurities, is superimposed to a Pauli constant contribution, probably arising from the metallic unreacted Mg.

2.3 Neutron irradiated graphites

In order to extend to the bulk the proton-irradiation induced ferromagnetism in graphite[105], we based our work on neutron irradiation which, as well as proton bombardment, induces defects into the crystalline structure of graphite but on a bulk scale. This is a very known effect, in particular for graphite, which has been the most common moderator in the first nuclear reactors. Since defects seem to be at the basis of the magnetism in carbon compounds, in particular in graphene[106], we tried to induce them in a controlled way, by following two different strategies:

- ✓ **Direct neutron bombardment** of graphite samples**;**
- ✓ **Indirect irradiation** by neutrons fission of Boron enriched graphites.

In other words we moved in the direction of synthesising a completely organic bulk ferromagnet since no really bulk magnetic signals have been measured until now.

2.3.1 LENA Reactor Pavia

Neutron irradiation was performed twice, on several compounds at the LENA reactor[107] (Pavia, Italy). It is a TRIGA MARK II type nuclear research reactor (250 kW steady-state nominal power and 250 MW pulsing): it offers many irradiation positions "in core" with neutrons fluxes ranging from 10^{11} up to 10^{12} and six irradiation channels "out core" with neutrons fluxes ranging from 10^{6} up to 10^{10}.

[105] P. Esquinazi *et al.*, "Magnetic order in proton irradiated graphite: Curie temperatures and magnetoresistance effect", *Journal of Nuclear Material* in press (presented at TMS 2008 Meeting).
[106] L. Pisani, J. A. Chan, B. Montanari and N. M. Harrison, Electronic structure and magnetic properties of graphitic ribbons, *Physical Review B* **75**, 064418 (2007).
[107] http://www-1.unipv.it/weblena/.

Figure 19: The TRIGA MARK II LENA reactor (Pavia, ITALY).

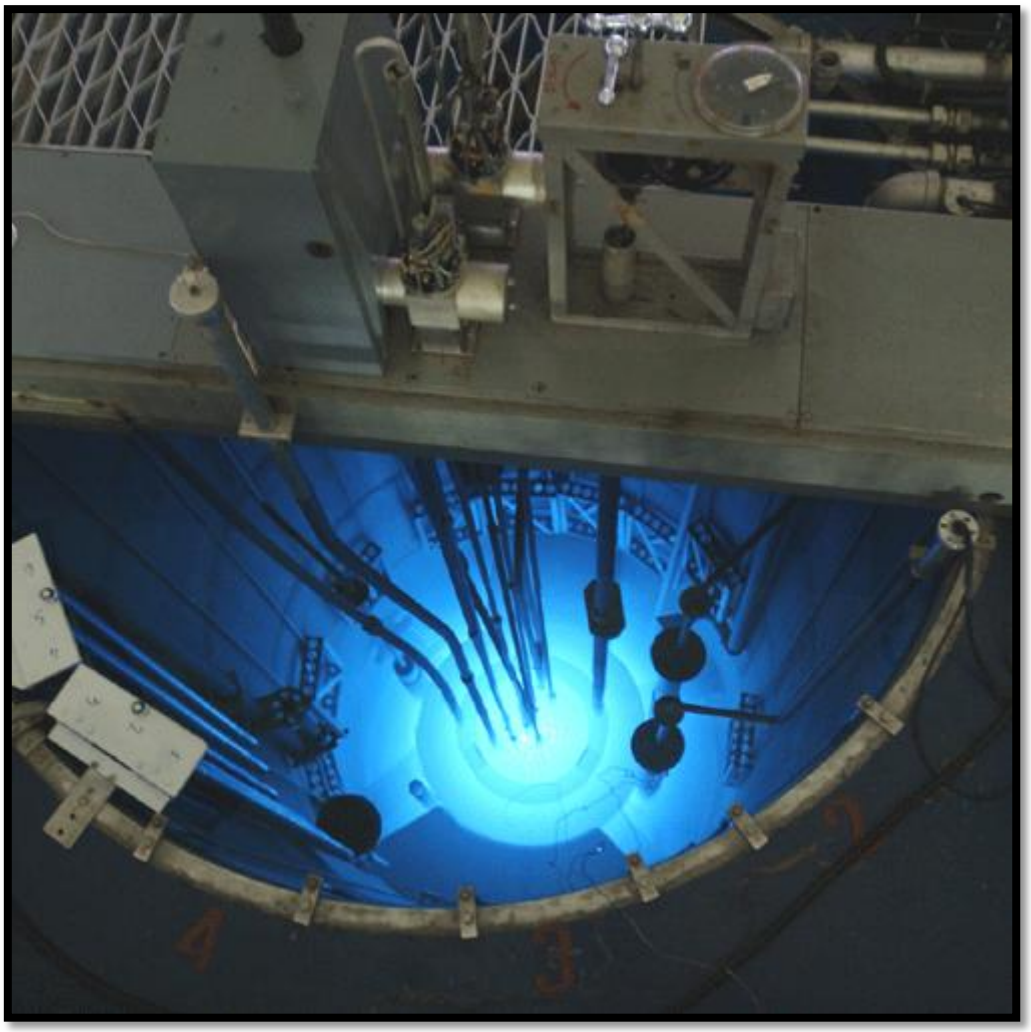

Figure 20: Top view of the LENA irradiation channels.

The sample irradiation was performed in the central channel (see Figure 21) in order to reach the highest neutron flux ($\varphi \sim 10^{12}$ n cm^{-2} s^{-1}).

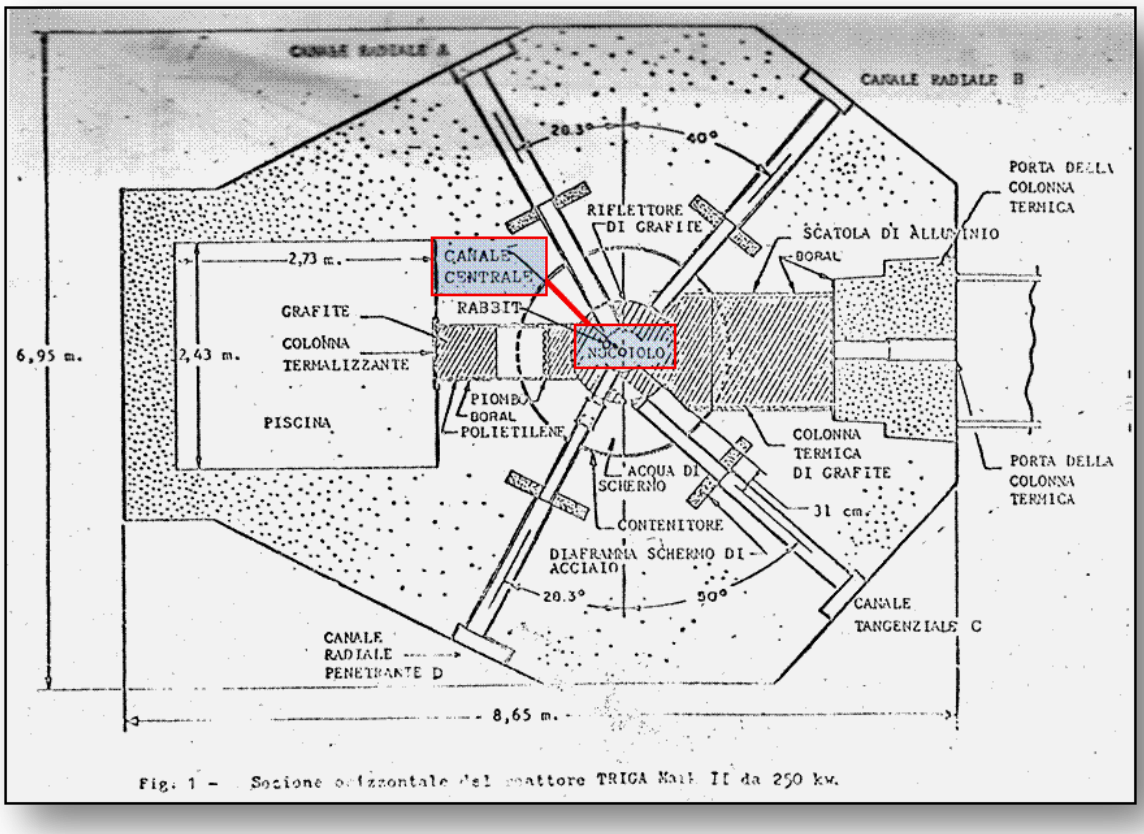

Figure 21: Triga Mark II reactor horizontal section: underlined in red the central channel in which the samples irradiation was performed.

During the first irradiation time we underestimated the radiation damage inflicted to the sample holder even if we intentionally projected and created the container using high purity Teflon material in order to avoid generation of secondary radioactive subproducts. Those inconveniences were then circumvented using two new sample holder: the first made of aluminium (see Figure 22) while the other were quartz vials directly used for SQUID measurements before and after irradiation without any sample contamination.

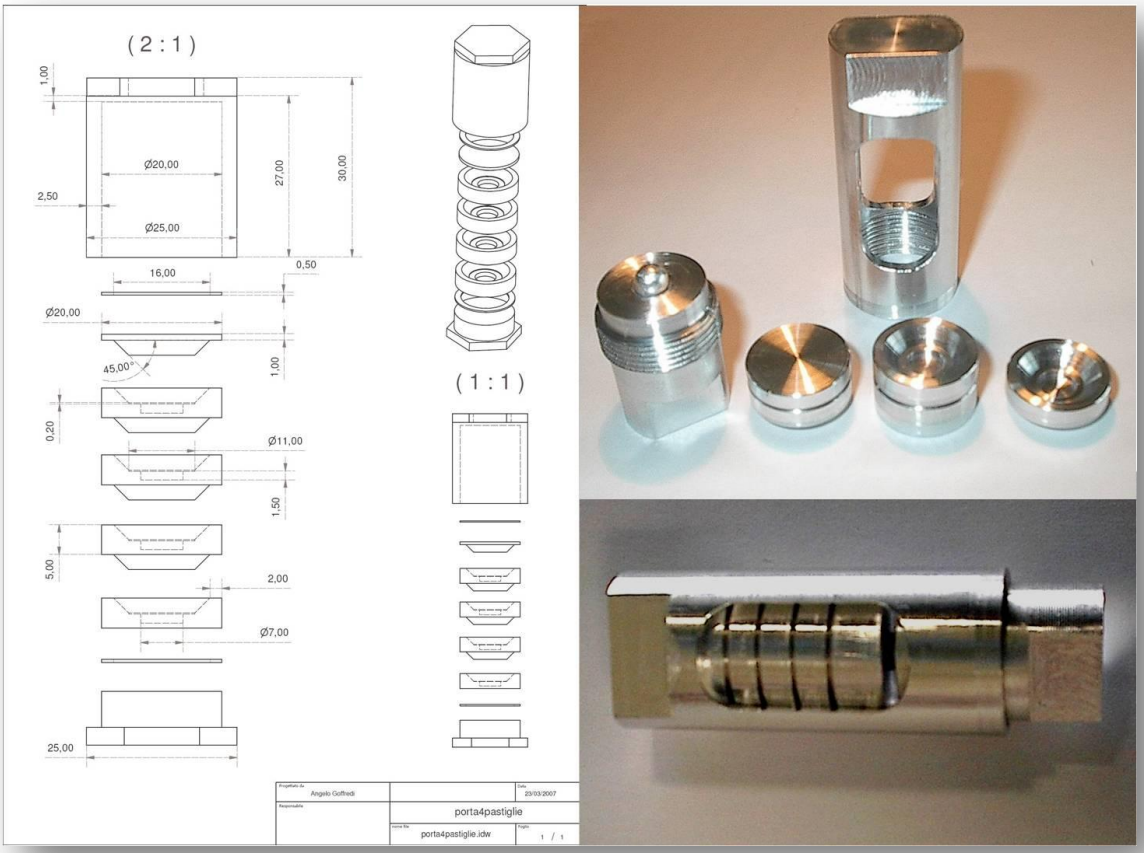

Figure 22: On the left the home-made sample holder project and on the right its visualization.

2.3.2 Boron enriched graphite

Basically, we tried to introduce defects into the graphite structure by simple neutron irradiation of boron enriched graphite through a direct exposure to the nuclear reactor flux. It is known that when an incident neutron ($E_n \sim 1$ eV, see Figure 23) hits a ^{10}B atom, a ^{4}He – an α particle – and a ^{7}Li nucleus are generated and emitted in opposite directions, approximately sharing the Q-value energy released in the nuclear reaction.

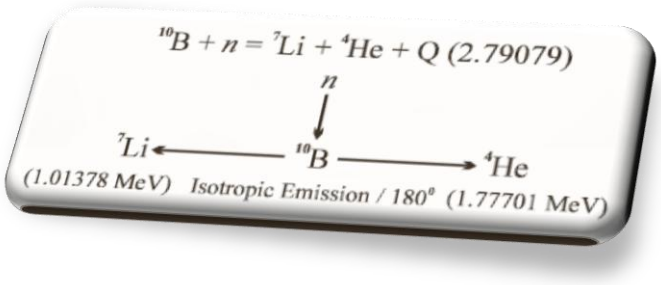

Figure 23: Nuclear interaction between a ^{10}B atom and an incident neutron particle ($E_n \sim 1$ eV).

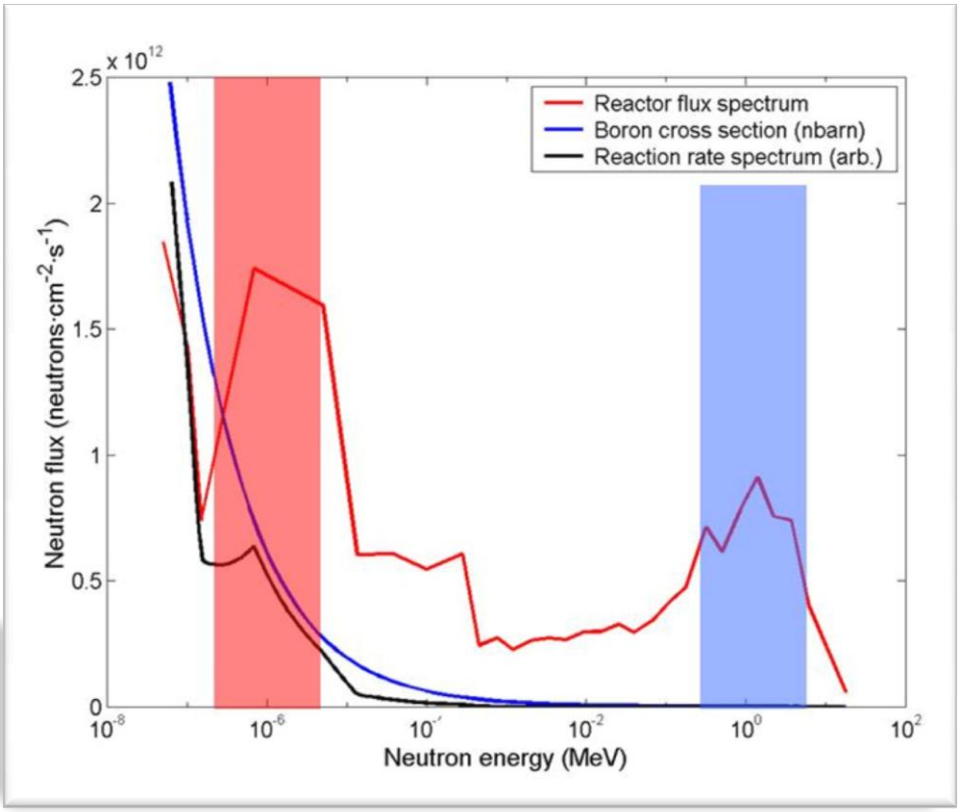

Figure 24: The bimodal spectrum of LENA reactor (250 KW, Pavia, Italy). The red curve shows the neutron flux spectrum, while the curve in blue represents the boron cross section. The black curve is the corresponding reaction rate spectrum.

The energy of emitted ^{4}He nucleus is 1.777 MeV, while in the case of ^{7}Li nucleus energy lowers up to 1.014 MeV. This kind of micro-nuclear explosion produces a

damage effect that has been simulated (see Figure 25) using SRIM2003 Monte Carlo simulations[108].

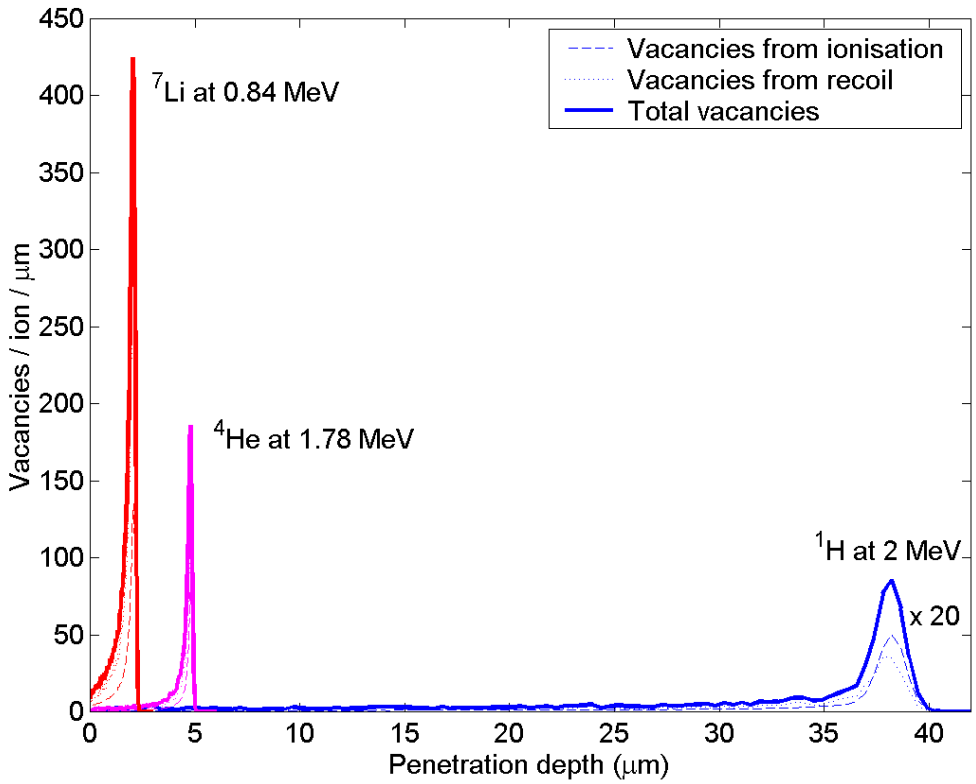

Figure 25: SRIM2003 Monte Carlo simulations of vacancies generated by the products of neutron irradiation of boron, namely ^{7}Li (read line) and ^{4}He (purple line); a comparison with the damage effect of 2 MeV protons is also reported (blue line, magnified by a 20 factor).

In other words this graph explains the amount of defects generated by the implanted particles and it is clearly shown that ^{7}Li and ^{4}He particles generate a higher amount of defects if compared to protons, taking also into account that the "proton peak" has been magnified by a 20 factor.

The samples were prepared tuning two fundamental parameters: boron doping percentage (see Figure 26) and emitted particle ranges (see the results of the simulation in Figure 27).

[108] A special thank to Prof. Tony Shiroka for all SRIM2003 Monte Carlo simulations.

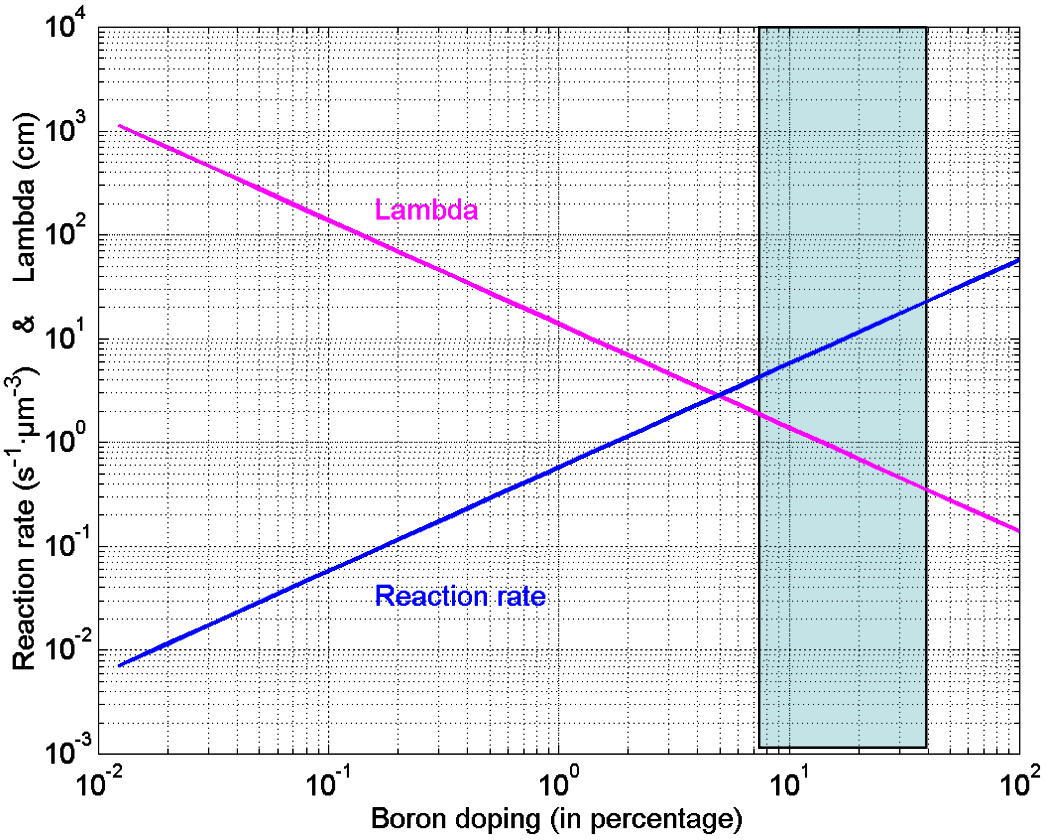

Figure 26: Trend of the nuclear reactions rate with respect to boron doping. On the same graph the trend of Lambda parameter compared to the boron doping is also reported. The shaded region has been identified as the ideal boron doping percentage.

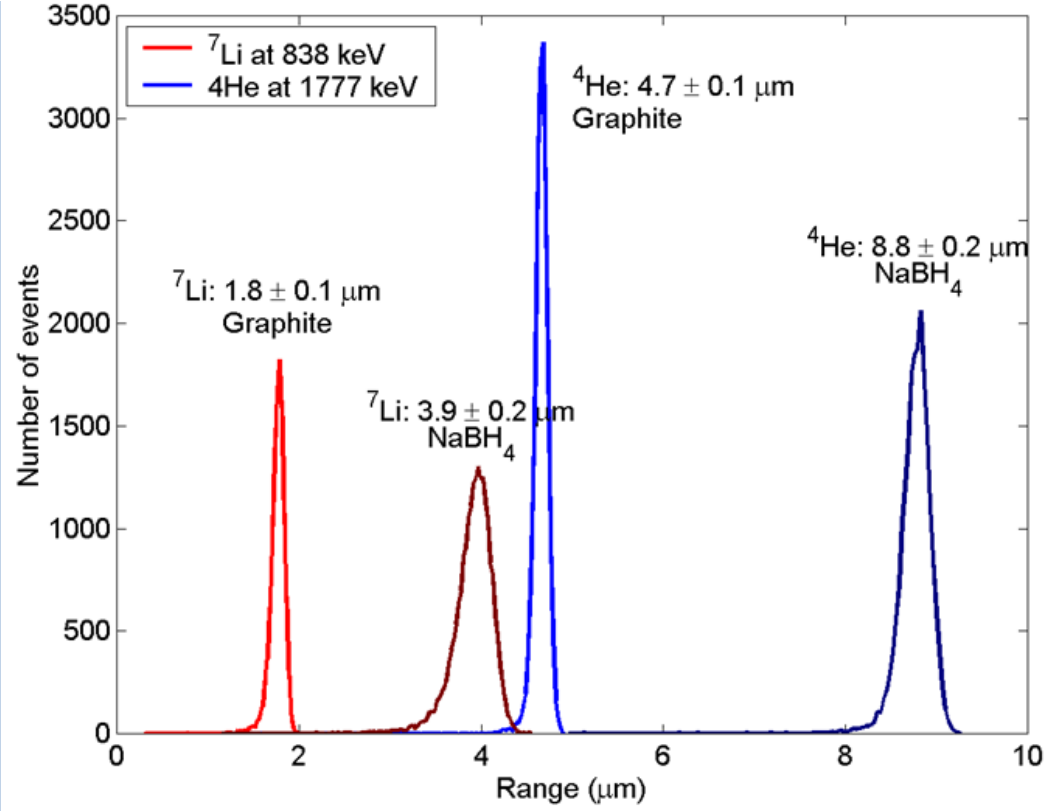

Figure 27: SRIM2003 Monte Carlo simulations of emitted particle ranges in Graphite and in the boron carrier: $NaBH_4$.

In Figure 26 the trend of reaction rate has been reported – that is the number of nuclear events per surface unit and time unit – and at the same time the Lambda trend, which represents the neutrons penetration depth (Figure 28), both as a function of the boron doping percentage. So this graph permits to identify the best boron doping percentage necessary to avoid a pure surface effect, that is nuclear explosions only on the graphite surface, and, on the same time, to let neutrons to pass through the graphite planes with no relevant damage – remember that graphite has been widely used as moderator in nuclear reactors –. Assuming those remarks, the underlined region corresponds to the range of boron doping percentage that has been followed in synthesising our samples.

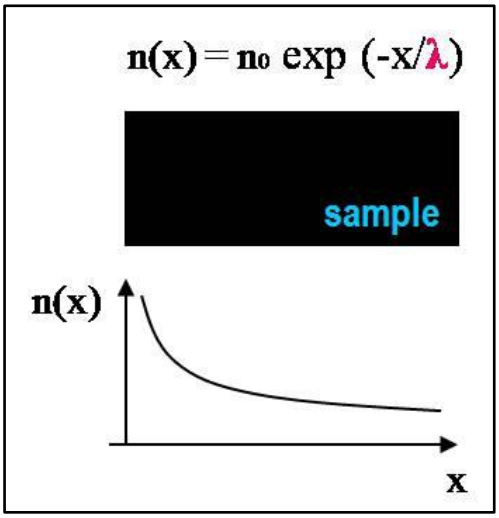

Figure 28: Lambda represents the neutrons penetration depth as a function of RW-A graphite sample thickness and it shows the trend of nuclear explosions through sample width.

Moreover Figure 27 shows our Monte Carlo simulations of the emitted particle ranges in graphite and in the adopted boron carrier: sodium boron hydride ($NaBH_4$) which has been our choice in order to avoid all the problems related with secondary radioactive product generation.

Taking into account these important parameters we have optimized the milling time necessary to reach the objective of decreasing grain dimensions down to particle ranges – that is the only way to allow the ^{7}Li and ^{4}He to come out from the $NaBH_4$ grains and damage graphite grains – increasing defects density and, however, preserving the graphite layered crystalline structure in the samples. Those dimensions were estimated evaluating the diffraction peaks enlargement at different milling times.

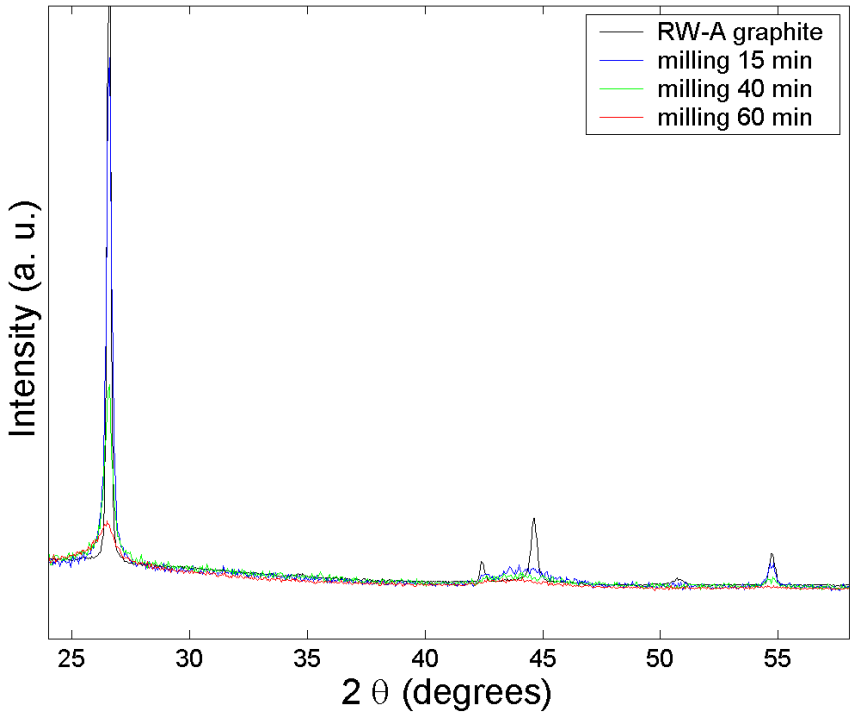

Figure 29: X-rays powder diffraction of different RW-A graphite samples. The black graph shows diffraction pattern of pure RW-A graphite (Ringsdorff® - SGL Carbon group) heated under vacuum at 700 °C for 7h. The other coloured diffractograms are referred to milled graphite samples respectively for 5, 10 and 15 minutes, stopping grinding every 5 minutes.

The ball-milling procedure not only operates on a macroscopic scale reducing grain dimensions, it is also directly involved on a microscopic scale introducing defects (dislocations and vacancies) in pristine graphite (we used RW-A high purity grade graphite, in which the nominal Fe impurities are below 0.2 ppm, in order to minimise the amount of magnetic impurities introduced in the samples). Moreover, the action of balls inside the grinding agate jar on graphite powder leads to graphite planes breaking and the consequently production of a great number of edges. In particular *zig-zag* edges have been shown to generate stable ferromagnetically ordered ground states along the edge[109] (see Figure 30).

[109] H. Lee *et al.*, *Chemical Physics Letters* **398**, 207–211 (2004).

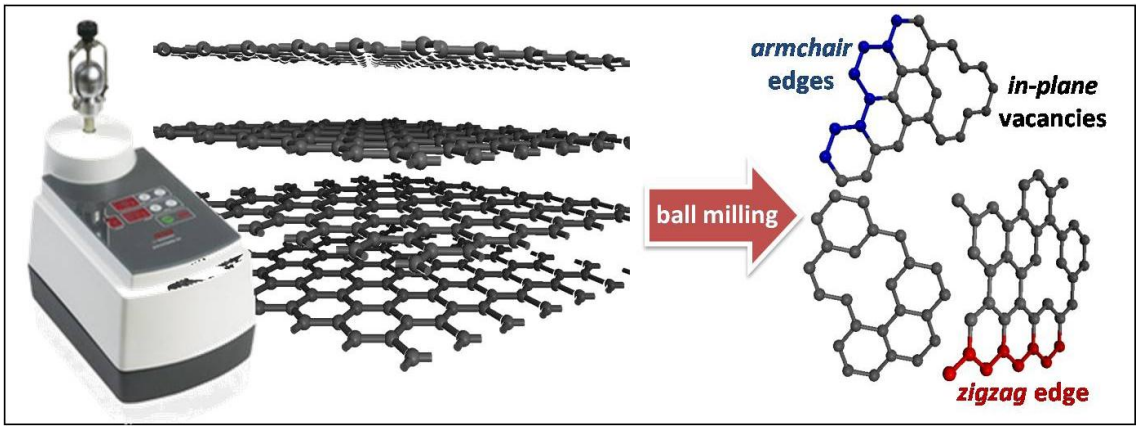

Figure 30: On the left the milling apparatus equipped with a jar is showed while on the other side can be seen the effect of grinding onto graphite planes: in-plane defects but also planes breaking are expected.

In other words one could say that the only milling action should bring a grinded graphite powder into a ferromagnetic sample: unfortunately SQUID measurements (see Figure 31) performed on these sample indicated the absence of any kind of magnetic order; in fact the only ball-milling effect on graphite is the production of paramagnetic centres apart from defects implantation and graphene layers generation.

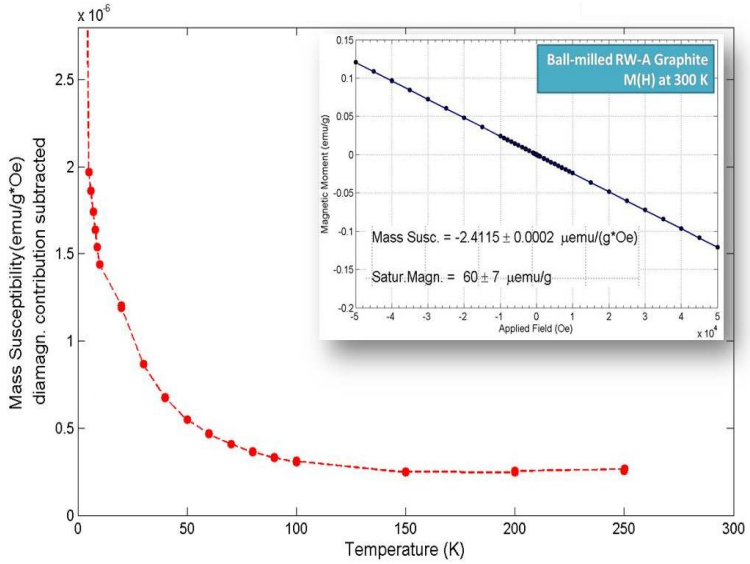

Figure 31: SQUID measurements showing the paramagnetism extracted from the graphite diamagnetic background (inset) are reported – all sample operations were performed in a controlled atmosphere glove-box – .

On the other hand, an accurate study of graphite morphology was carried out on ball milled graphite by Transmission Electron Microscopy (TEM) technique. Images were taken both on as-prepared samples and on powders dispersed in ethanol; in both cases, the photos confirm the high grade of disorder of our system, as expected (see Figure 32). In particular, it is possible to identify either regions where the original graphite layered structure is preserved or regions where the inter-layer order was lost.

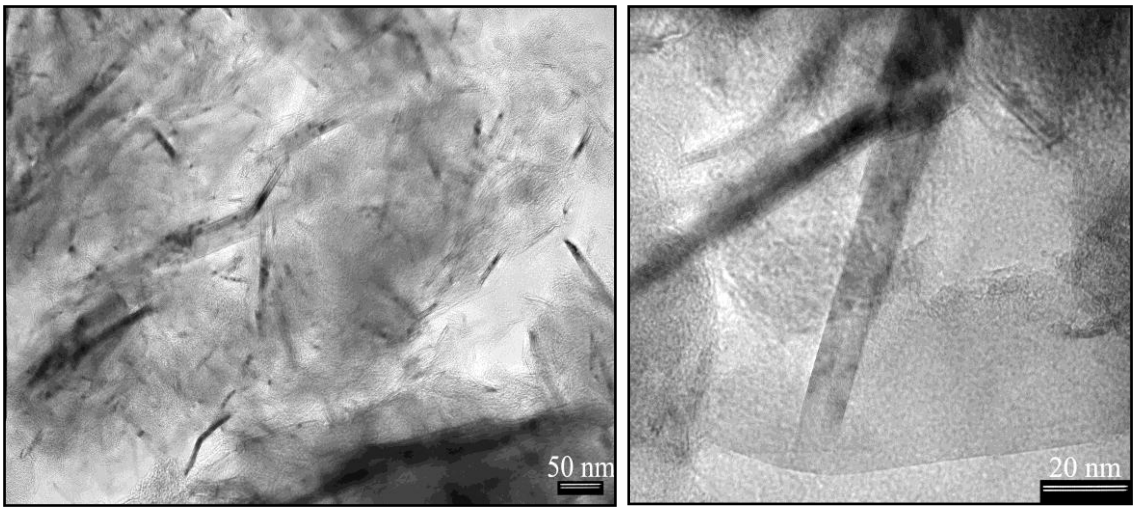

Figure 32: **left)** Transmission Electron Microscopy image of 1h high-frequency ball-milled RW-A graphite; it could be recognised the presence of both 2D (layers) and 1D (ribbons) structures. **right)** Image of a ribbon-like structure.

However, a layered arrangement can be recognized even in these nanoribbons (see Figure 33). The example shown in the picture is indeed a multigraphene ribbon, in which 30 graphene sheets of approximately only 2 nm width and ~100 nm length are stacked with the typical graphite planar distance of ~3.4 Å. It is worth noting that, since in this nanostructure the ribbon width is about one order of magnitude smaller than the dimension along the stacking direction, the role played by the graphite edges in such arrangement is very important. These nanoribbons generation mechanism is still an open question but we think that could be a consequence of the high local temperature due to milling action.

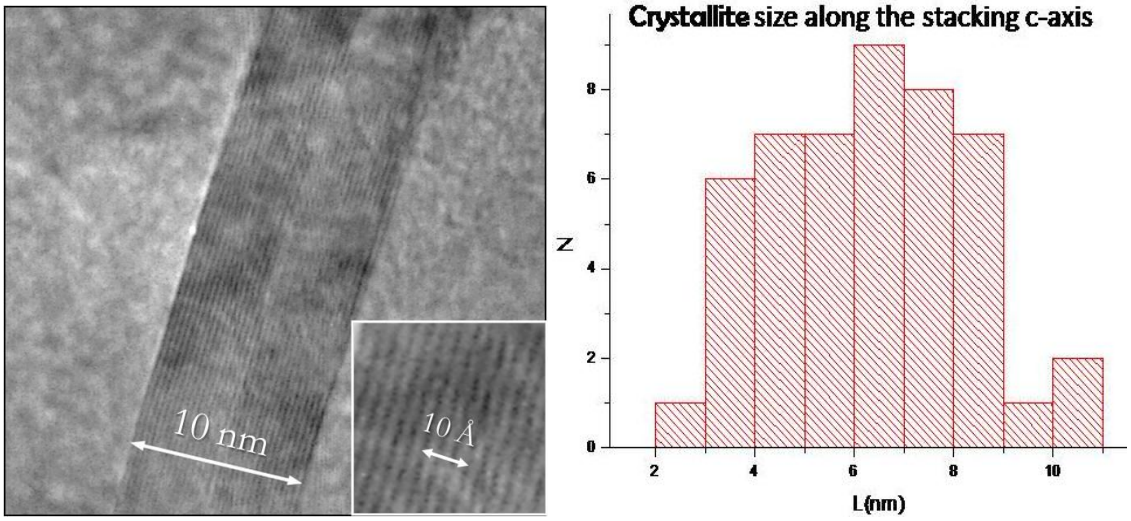

Figure 33: Ball-milled graphite (BMG) morphology has been fully characterized using TEM microscopy (left image). In particular we can see the layered structure with the characteristic graphite stacking distance of ~3.4 Å. The mean thickness of the observed multigraphene ribbons is confirmed to be ~ 6 nm.

Focusing on B-enriched graphite synthesis, actually we have prepared samples with a boron doping percentage ranging from 1 %, to 50%. We have synthesized a huge number of samples in order to reach high reproducibility and milling action control. The synthesis consist of an initial milling of RW-A graphite and $NaBH_4$ (99.99% purity, Aldrich) respectively for 10 and 40 minutes, stopping grinding every 5 minutes. After that the two reagents were perfectly mixed together by an additional 3 minutes milling – one by one – and finally reduced in pellets. All the operations were performed in a controlled atmosphere glove box. Pellets were introduced either in an aluminium container or in quartz ampoules and then irradiated for six hours in the Lena reactor central channel. All samples underwent SQUID measurements which will be presented in the next paragraph together with the measurements on the other irradiated samples.

2.3.2 Intercalated graphites

The intercalation of graphite with molecular spacers, up to the exfoliation, allows to obtain the quasi-isolation of the single graphene planes in bulk; in these systems, the in-plane defects induced by neutron bombardment at relatively high energy (~ 1 MeV) are expected to be magnetic[14].

In general neutrons produce defects in graphite by elastically knocking carbon atoms. The binding energy of C – C single bond is about 7 eV, hence, assuming that only ⅓ of neutron energy is transferred to carbon atoms during an elastic process, if $E_n < 60$ eV no defects will be implanted in graphite. On the contrary, if $60 < E_n < 120$ eV neutrons will produce only primary defects and in the case of $E_n > 120$ eV secondary defects will be also generated[62]. In our case, the irradiation source utilised was the main channel of the LENA reactor (Pavia, Italy), where neutron beam is constituted essentially by two contributions: the former of high-energy neutrons (~1 MeV), whose flux is of $0.8 \cdot 10^{12}$ neutrons / cm² • sec, while the latter of epithermal neutrons (~1 eV), whose flux is of $1.7 \cdot 10^{12}$ neutrons / cm² • sec (see Figure 24).

Therefore if E_n=1 MeV, as it is in our case, the secondary defects represent the majority of the damage (see Figure 34) and actually in this conditions graphite is irradiated by ionised carbon atoms, rather than neutrons with a great similarity with high energy proton bombardment effect.

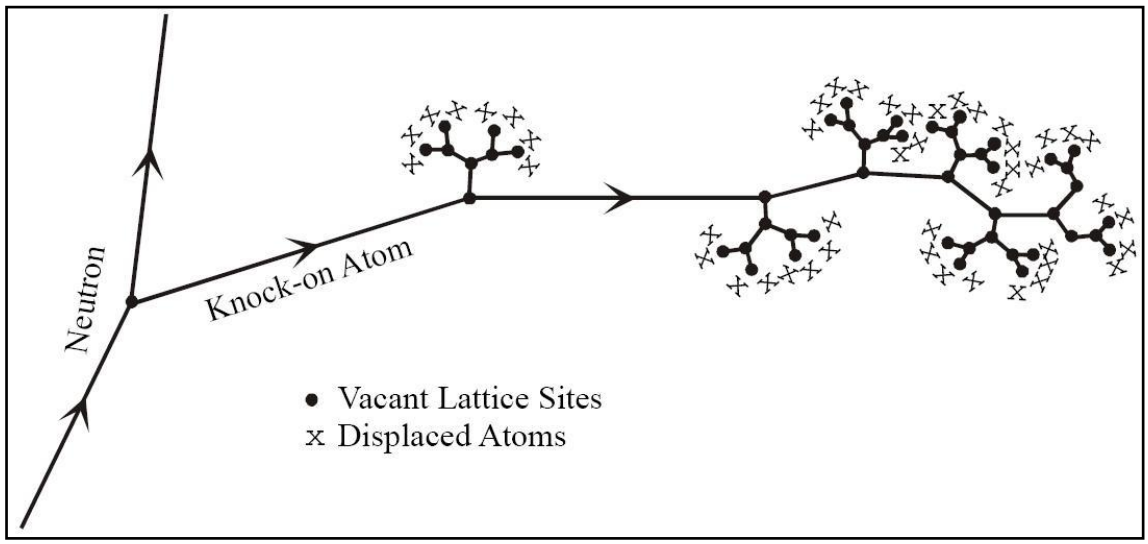

Figure 34: Distribution of displaced atoms and vacant lattice sites (secondary defects) due to a single knock-on atom (primary defect).

The irradiated samples were:

- Pristine graphite (RW-A purity grade, produced by SGL Carbon);
- Potassium intercalated graphite (KC_{24}) exposed to NH_3 vapours;
- RW-A graphite treated with SO_3 vapours;
- Exfoliated graphite (see Scheme 6);
- Potassium intercalated graphite (KC_{24}) treated with BCl_3 vapours;
- Potassium intercalated graphite (KC_{24}) treated with Borazine ($B_3N_3H_6$) vapours.

A "standard" method for the intercalation, as depicted in Figure 35, consisted in exposing KC_{24} to the intercalating molecule vapour pressure, after pumping the system under high vacuum at low temperature. This chemical contact in every case, induced a rapid colour changing of the pristine potassium intercalated graphite, from gold/blue to brown/black, followed by an evident temperature increase. The confirmation of the effective intercalation was provided by laboratory XRD analysis (see "Experimental section" chapter).

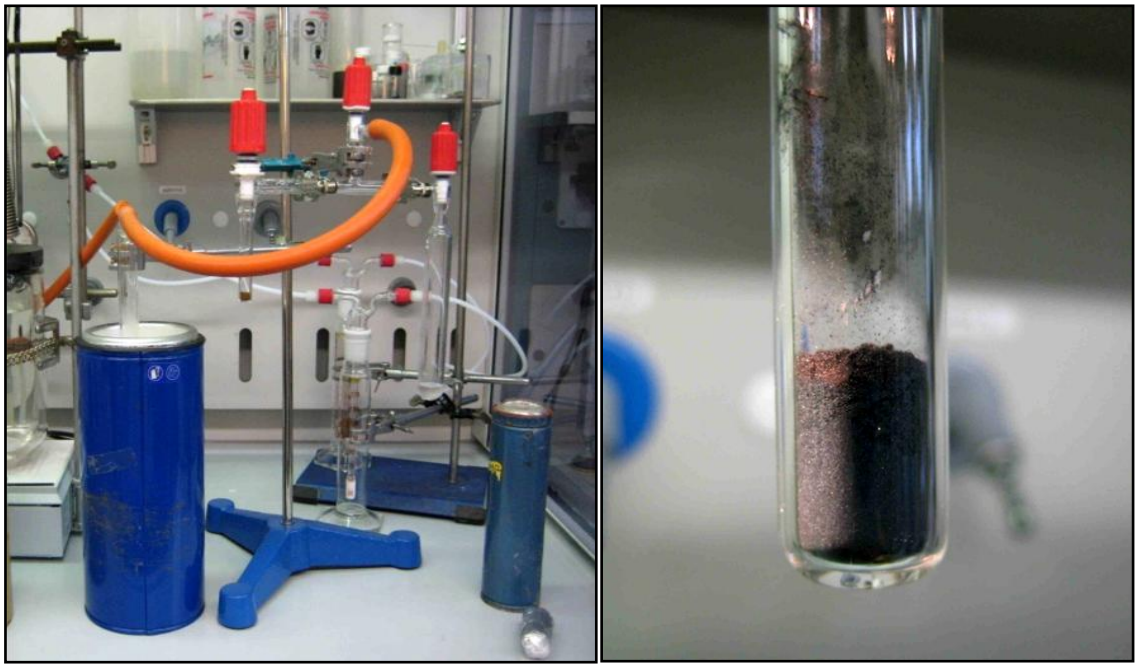

Figure 35: *Left*) Potassium intercalated graphite (KC_{24}) treated with SO_3 vapours experimental setup. *Right*) The intercalation moment; colour changing can be clearly seen, the intercalation starting from the top of the vial and results from the diffusion of the intercalant into graphite powder.

Among all the molecular spacers we used to distance graphite planes it is important to notice that the sample 5 and 6 prepared by intercalation of Boron containing spacers such as Boron trichloride (BCl_3) and Borazine ($B_3N_3H_3$), called the inorganic Benzene, has been intentionally studied to induce defects onto graphite lattice both directly by high energetic neutrons and indirectly via boron nuclear explosion, in order to maximize damage action as well as magnetism.

All the samples were manipulated using an Ar glove box avoiding any O_2 and H_2O contamination. Moreover, with the intention of overcoming the problems of sample-holder degradation, which affected the first irradiation experiment (see Figure 36), they were sealed either in aluminium containers or in quartz ampoules. On the one hand, these vessels did not show any chemical degradation or generation of secondary radioactive products while on the other hand, the quarts vials had the advantage of being suitable for a direct magnetic measurement with our SQUID apparatus. Hence, we managed to check the magnetic response of the samples before and after the irradiation without any intermediate manipulation.

Figure 36: Teflon sample holder degradation after the first longer irradiation section. Even though we used a high purity Teflon containers, as suggested by the LENA local contact, they encounter degradation after neutron treatment.

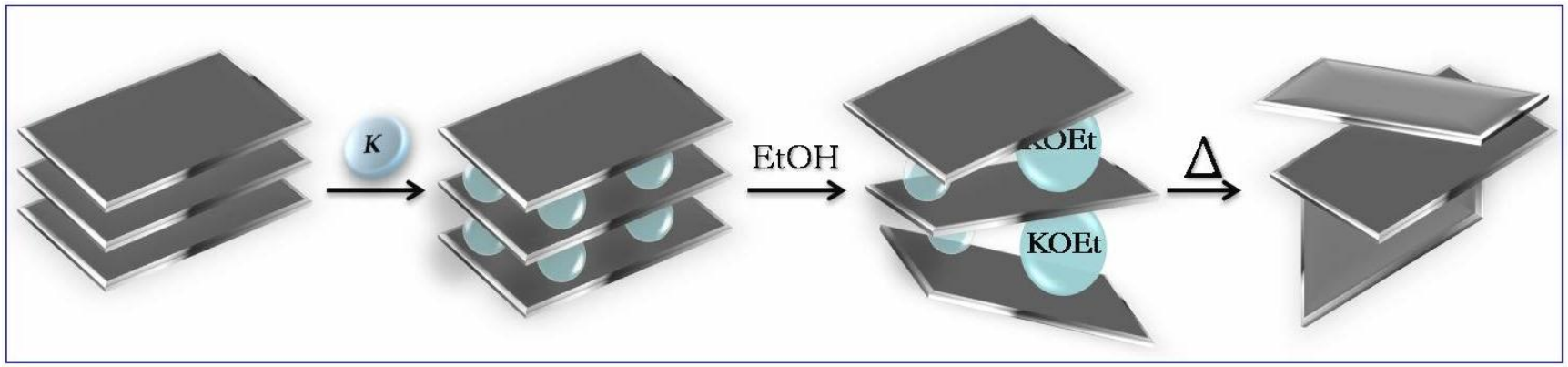

Scheme 6: Exfoliation process of a graphite sample. Firstly pristine graphite powder is exposed to potassium vapours in order to reach a stage I intercalation (KC_8), then the GIC is exposed to ethanol vapours promoting the synthesis of a K-ethanolate *intra*-planes. Finally a high and fast thermal treatment lets the CH_3CH_2OK decomposing, thus inducing the separation of the planes.

We planned an irradiation time of six hours – shorter than the first experiment trying to overcome the problems of sample-holder degradation – at a neutron flux of $0.8 \cdot 10^{12}$ neutrons / cm^2 • sec, equivalent to a dose of $1.73 \cdot 10^{16}$ neutrons / cm^2.

SQUID magnetic measurements, however, did not detect a clear evidence of the onset of magnetism in any of the irradiated samples. The typical change of magnetisation in the samples, measured either as a function of the temperature or as a function of the applied field, evidenced only an increase of paramagnetism, probably due to the contribution of the induced defects (see Figure 37 and Figure **38**).

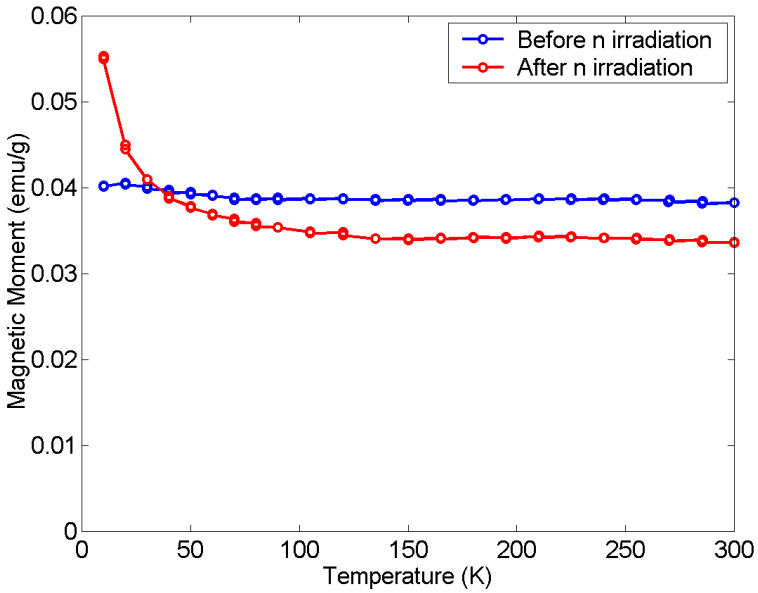

Figure 37: Typical temperature dependence in an irradiated sample (KC_{24} + borazine in this case, field cooling measurement applying a field of 5 Tesla). A difference is present only in the temperature independent susceptibility and in the Curie-Weiss paramagnetic contribution of the defects. No steep increase in the magnetization due to the onset of magnetic order was detected.

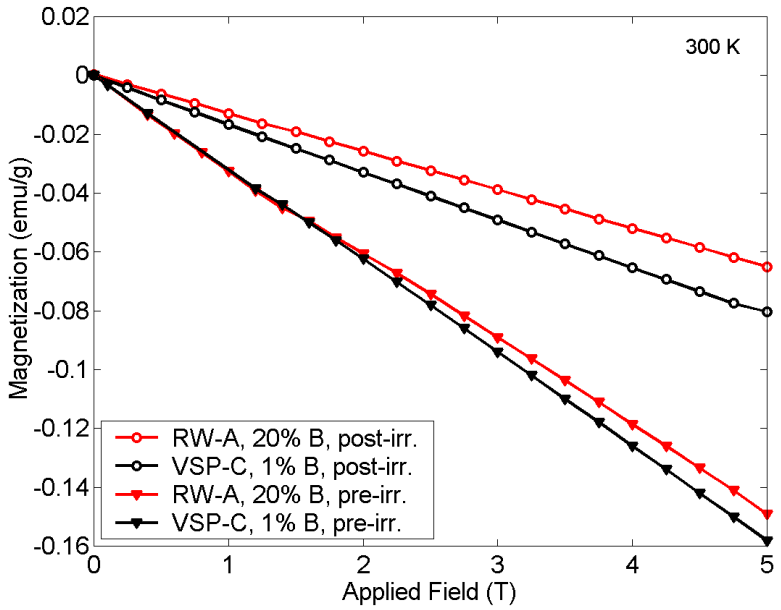

Figure 38: SQUID measurements showing the decrease of diamagnetism in $NaBH_4$ enriched graphite after neutron irradiation (measurements performed either on RW-A graphite purity grade and previously on the lower purity grade VSP-C graphite).

Hence, the expected defects density induced directly by neutrons, based on the Thompson-Wright formula, was ~ $3 \cdot 10^{15}$ neutrons / cm^2 , namely one $C_{displaced}$ every 40000 carbon atoms. So we can guess for our sample one def in a cube of 35 atoms of edge and, in other words, can be estimated a mean distance between two implanted vacancies of 50 Å while, on the one hand, theoreticians have indicated to be ferromagnetic only graphene with defects separation up to 20 Å[14]. Also, Prof. Esquinazi *et al.*[63] calculated, in the case of magnetic proton irradiation graphite spots, defect densities of one C_{dis} every 266 carbon atoms with a defect separation of 10 Å.
In other word those estimations could explain that in our case the critical defect concentration in the graphene layers has not been reached with the performed treatments, and in that direction further investigations are in progress.

Conclusions

The present work describes all the efforts performed during a three year PhD course in the Fullerene Research group of Parma within the European FERROCARBON venture. In the last three years the FERROCARBON project (financed by NEST FP6 and coordinated by our group) has brought together an array of European scientific talents from Italy, Spain, Germany, Sweden, Russia and the United Kingdom with the common challenging task of achieving and understanding how to produce completely organic room-temperature ferromagnets routinely and in bulk.

As a general matter, the efforts has been focused on the synthesis of new room temperature carbon based ferromagnets following substantially the two most promising systems described in the "Introduction" chapter.

Firstly, we managed to synthesise and characterise two new polymeric fullerides, which displayed noticeable features. Since the C_{60} molecule reacts with the strong Lewis superacid AsF_5, we reached the synthesis of the first fullerenium salt, that is to say a donor/acceptor intercalated C_{60} system in which fullerenes are in the oxidised C_{60}^{2+} state. In addition this cationic fulleride is indeed a polymer, formed by 1D zigzag chains never observed before in other fullerene based compounds. In spite of the unconventional electronic properties expected from a fullerenium salt, SQUID magnetic measurements did not show significant electronic and magnetic properties even if further investigations are in progress.

Along with the creation of new fullerene polymers, we improved, with a completely new synthetic path, the preparation of the polymeric fullerides Mg_xC_{60} having, in our case, the nominal stoichiometry Mg_5C_{60}: we overcame all the previous insuperable magnesium intercalation problems through a thermal decomposition of a metallorganic precursor in order to intercalate the alkali-earth ion into C_{60} powder through a single day synthesis. The preliminary magnetic response was invariably found diamagnetic for all the samples, with only small paramagnetic contribution arising from impurities; in fact no evidence of magnetic ordering, even at low temperatures, was detected.

Secondly, we performed neutron irradiation on several graphite samples at the LENA TRIGA MARK II type nuclear research reactor (Pavia, Italy), in order to induce ferromagnetic order in high purity graphite systems.

Since defective graphene planes are supposed by theoreticians to be magnetic[106], we tried to provoke them in a controlled way, either by direct neutron bombardment of intercalated / exfoliated graphite samples or by indirect irradiation trough neutron fission of Boron enriched graphites.

In the first class of compounds we increased the inter-layer distance between graphite planes through intercalation or even exfoliation of high purity grade RW-A graphite in order to achieve also in the bulk the irradiation of single graphite planes. The other class of samples was synthesised by enriching milled graphite with a Boron carrier thus exploiting the fission of ^{10}B with consecutively emission of high energetic ^{4}He and ^{7}Li particles, as a real *in situ* defect generators.

The preliminary magnetic characterizations of the irradiated systems showed that neutron irradiation of pure, boron intercalated and exfoliated graphite mainly produced Frankel type defects which macroscopically consisted in an increase of the sample paramagnetism but did not show any relevant onset of ferromagnetism even at low temperature.

At the moment we are planning firstly a longer irradiation section– regarding only the first class of intercalated graphites because a precise estimation of the defect number of the boron composites were not possible – since our SRIM2003 Monte Carlo simulations showed that the induced defect density was ~ $3 \cdot 10^{18}$ neutrons / cm^3, corresponding to 50 Å mean defect separation whereas theoreticians[106] predict graphene room-temperature ferromagnetism only for defect separations up to 20 Å. In addition we are going to perform a longer irradiation experiment even on boron-graphite composite with smaller grains dimensions.

Experimental Section

4.1 Experimental details

4.1.1 X-Rays Diffraction measurements

Polycrystalline materials are made up of a great number of tiny (μm to nm) single crystals. The diffracted rays from a single crystal point to precise directions each corresponding to a family of diffraction planes. The diffraction pattern from a polycrystalline powder sample forms a series of diffraction cones, called Debye-Scherrer cones, each corresponding to the diffraction from the same family of crystalline planes in the different powder grains.

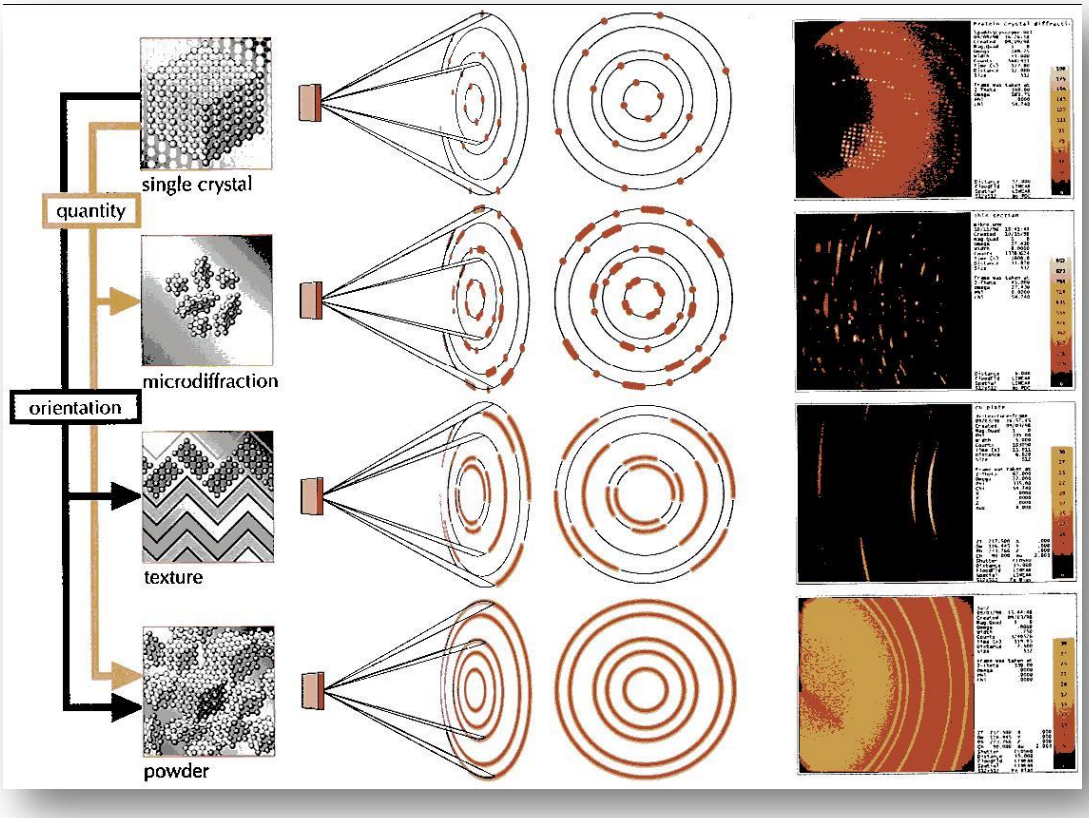

Figure 39: Patterns of diffracted x-rays: different examples depending on the specimen nature.

In the last two decades the development of very effective mathematical procedures (Rietveld method) for the quantitative analysis of powder diffraction patterns

determined the rapid diffusion of this method which nowadays can be considered as one of the main investigation techniques in material science. The compounds studied in this thesis work were in polycrystalline form, due to the impossibility, so far, to produce single crystals. Hence powder diffraction experiments and successive analyses were performed on the samples.

The Rietveld method is based on the "least square" routine and allows the refinement of the diffraction data starting from the knowledge of a rough structural model. The analysis is performed by optimising the agreement between the observed data and those calculated. This process considers a high number of free parameters (including the lineshape) to be refined and requires complicated calculations which only the recent advances in computer technologies allowed to be easily executed with conventional personal computers.

The possible geometries in an x-ray powder diffraction experiment are essentially Bragg- Brentano and Debye-Scherrer geometries. Modern powder x-ray diffractometers consist of an x-ray source, a movable sample platform, an x-ray detector (usually a scintillation detector), and the associated computer controlled electronics. The sample is positioned in the centre of the goniometer while the sample holder spins slowly during the experiment to improve the homogeneity of the powder scattering. The x-ray source is a Cu or Mo anode (see Figure 40).

The XRD results which are shown in the present PhD thesis work mainly refer to experiments performed in Debye-Scherrer geometry with a Bruker D8 Discover equipped with an HY STAR area detector and GADDS, with a sealed tube generator (CuK_{α}). The powders are stored in a quartz capillary having diameter ~ 0.7 mm.

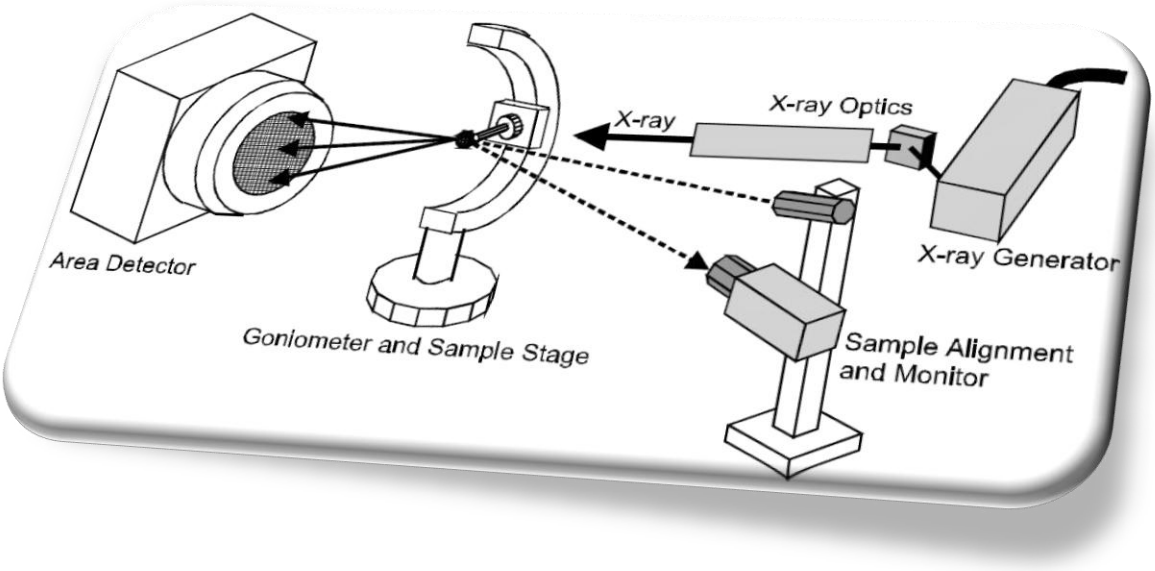

Figure 40: Five major components in an X-ray powder diffractometer, an area detector, an x-ray generator, x-ray optics (monochromator and collimator), goniometer and sample stage, sample alignment and monitoring (laser/video) system.

Some measurements were performed in large scale Facilities, as the European Sinchrotron Radiation Facility (ESRF) and the Institut Laue Langevin ILL (Grenoble), respectively at the powder diffraction beamline ID31 and SuperD2B.

4.1.2 SQUID measurements

The magnetic measurements performed on the samples which were synthesized during this work were performed with a Quantum Design MPMS-XL5 SQUID magnetometer[110] (SQUID is an acronym for Superconducting Quantum Interference Device). Essentially it is an extremely sensitive magnetometer used to measure small magnetic moment values.

The magnetic characterization of the samples consisted essentially in measurements at different applied magnetic field values at room temperature and measurements at different temperatures at a selected field value. The former type of measurement is the

[110] A special thank to Dr. Matteo Belli for magnetic characterizations (SQUID analysis).

most interesting for the identification of ferromagnetic and para/diamagnetic components of the magnetic response of the different samples, though also the temperature scans are necessary to identify possible onset of ferromagnetism at low temperature. Of course, the behaviour at room temperature is the most interesting for possible applications.

4.1.3 NMR Analysis

High resolution ^{1}H-NMR (NMR is an acronym for Nuclear Magnetic Resonance) measurements were performed using a Brucker AC300 spectrometer. The chemical shifts are presented in part per million (ppm) and all analysis were carried out at the CIM (Centro Interfacoltà Misure – Parma University).

4.1.4 Chemical details

Before describing the single procedures it is necessary to premise that all substance manipulations have been carried out in a Controlled Atmosphere Argon Glove Box, Mr. Braun Labmaster 130, which guaranties to operate with a monitored concentration of H_2O and O_2 (< 1 ppm). This equipment allows to use air and water extremely sensitive reagents and product but also to avoid any sample contamination.

4.2 Synthetic report

In this section will be presented the experimental details related to all preparations performed during the PhD period.

4.2.1 Synthesis of Fullerenium dihexafluoroarsenate

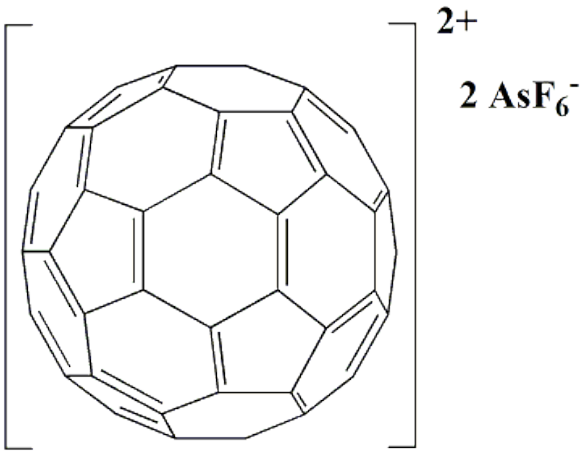

Figure 41: Fullerenium dihexafluoroarsenate.

280 mg of C_{60} (0.39 mmol, Merck 99.9%), fine milled in an agate mortar, were inserted in a Schlenk tube equipped with a Teflon-covered magnetic stirring bar. Once extracted from the GB, the reaction tube was connected to a vacuum line (see Scheme 3) and evacuated. After transferring a definite quantity of solvent (liquid SO_2 dehydrated over CaH_2), 0.43 bar (1.16 mmol) of Arsenic pentafluoride (AsF_5) has been condensed over C_{60} powder. The mixture was then heated to 50 °C while stirring for 15 h. At this time gaseous sub products and solvent have been evaporated and neutralized in a NaOH solution. 370 mg (0.34 mmol, 87% yield) of a black solid have been collected and immediately stored in liquid nitrogen in order to prevent any sample degradation.

All structural and magnetic analysis have already been presented in the "Results and discussion" chapter.

4.2.2 Synthesis of Magnesiumanthracene • 3THF complex

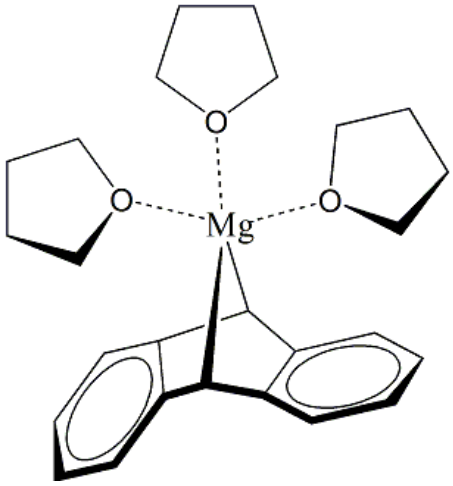

Figure 42: Magnesium-Anthracene organometallic complex.

To a mixture of 482 mg (20.4 mmol) of magnesium powder (Alfa-Aesar, ~ 325 mesh, 99.8%) and 1.842 (10.25 mmol) of Anthracene contained in a 100-ml round bottom Schlenk flask equipped with a Teflon-covered magnetic stirring bar and attached to a high-vacuum line (see

Scheme **2**) was transferred by condensation 10 ml of THF dried over $LiAlH_4$. Finally, 40 μl of ethylene dibromide was added to activate the Mg surface. Heating and sonicating (ultrasonic tip dipped in water bath, amplitude of 20 pulses/sec) the solution to 40 °C caused the colour to shift to a bright yellow. After 7 h the mixture consisted of an orange-yellow flocculent solid in a green-yellow solution. After that the solvent was evacuated and 3.47 g of a solid product were collected (82.4% yield).

4.2.3 Synthesis of Magnesium Fullerite

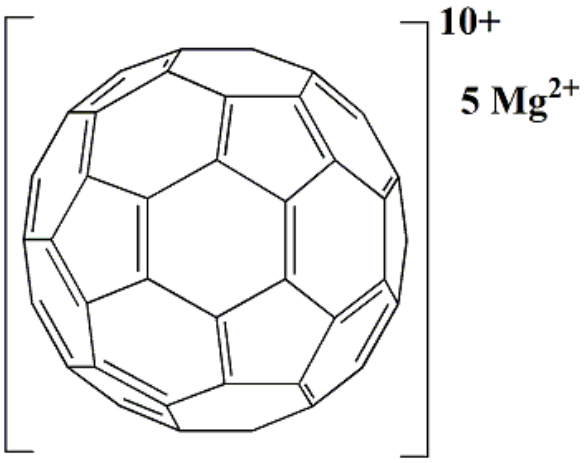

Figure 43: Mg-C_{60} polymer with the nominal stoichiometry Mg_5C_{60}.

To 1.31 g (3.13 mmol) of Magnesium complex (see Figure 42) a stoichiometric amount of Fullerene powder was added (460 mg, 0.64 mmol). The mixture was sealed in a vial and temperature treated (50°C/h up to 480°C, annealing for 10 h).

All structural and magnetic analysis have already been presented in the "Results and discussion" chapter.

4.2.4 Synthesis of Borazine

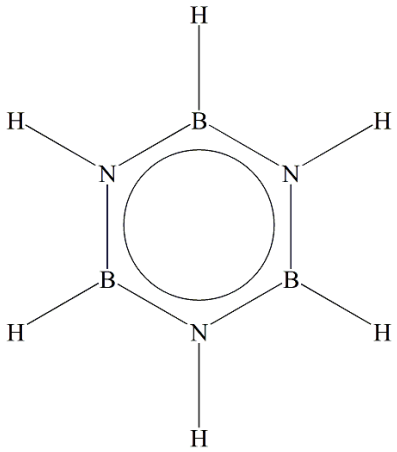

Figure 44: The Borazine structure; it is also called the "Inorganic benzene".

Sodiumboronhydride and ammonium sulphate were purchased from Aldrich and used after GB storage. Tetraglyme was dried over 4 Å molecular sieves.

27.3 g (0.20 mol) of $(NH_4)_2SO_4$ were inserted in a 1L, three-neck round-bottomed flask and dried at 40 torr at 120 °C. Then a solution of 10.6 g (0.27 mol) of $NaBH_4$ and 116 mL of anhydrous tetraglyme was added drop by drop during 3h under Argon flux. The flask was than fitted with a thermometer and a reflux condenser. The exit of the reflux condenser was connected to a standard vacuum line equipped with one Methanol and two liquid-nitrogen traps. The reaction mixture was gradually warmed to 135 °C over the course of 1 h and held at this temperature for an additional hour under a dynamic vacuum (the pressure was maintained at 2-5 Torr by the continuous removal of the evolved hydrogen and borazine through the vacuum line). 4.05 g (56% yield) of a colourless liquid product was collected and stored at 4 °C.

Figure 45: Borazine synthesis experimental setup.

The obtained borazine has been characterized through ^{1}H-NMR spectrometry (see Figure 46).

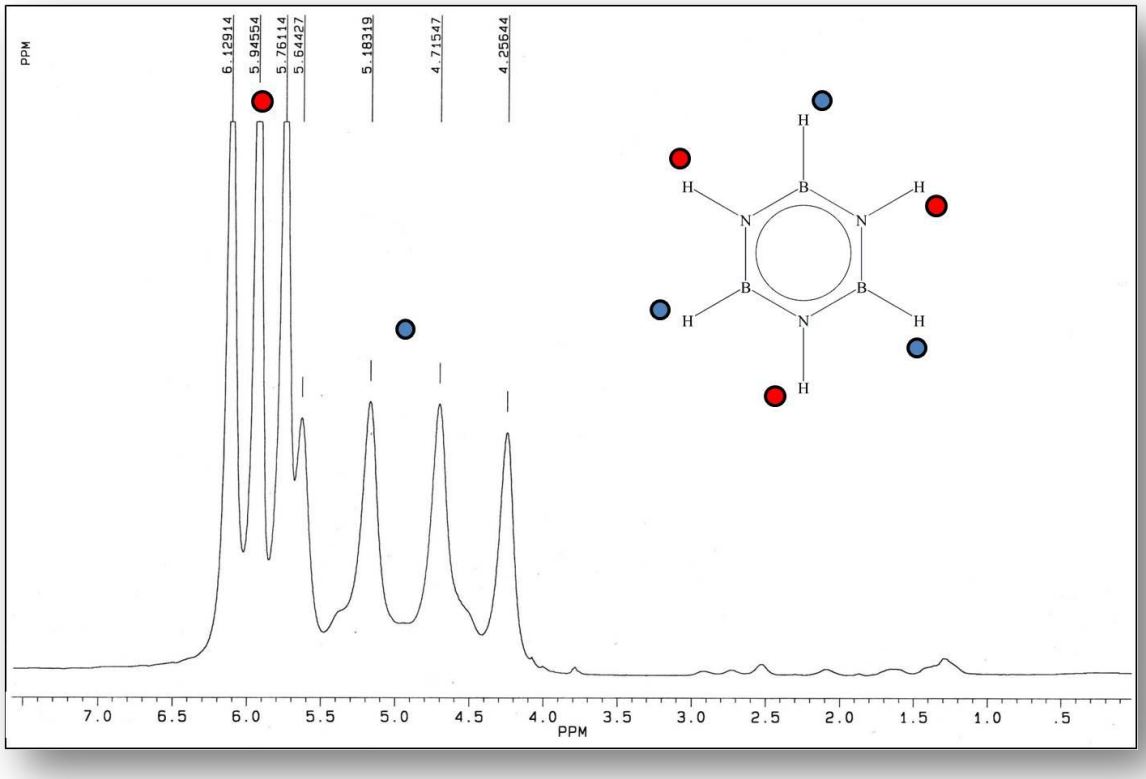

Figure 46: ^{1}H-NMR spectra of our borazine. In particular can be observed B –H proton at δ 4-5 ppm as a quartet and N–H proton at 5.5-6 ppm as a triplet[111,112].

[111] P. J. Fazen, J. S. Beck, A. Lynch, E. E. Remsen and L. G. Sneddon, *Chem Mater.* **2**, 96 (1990).
[112] E. K. Mellon, B. M. Coker and P. B. Dillon, *Inorganic Chemistry* **11**, 852-857 (1972).

4.2.5 Synthesis of stage I/II- K-GIC (KC_8 – KC_{24})

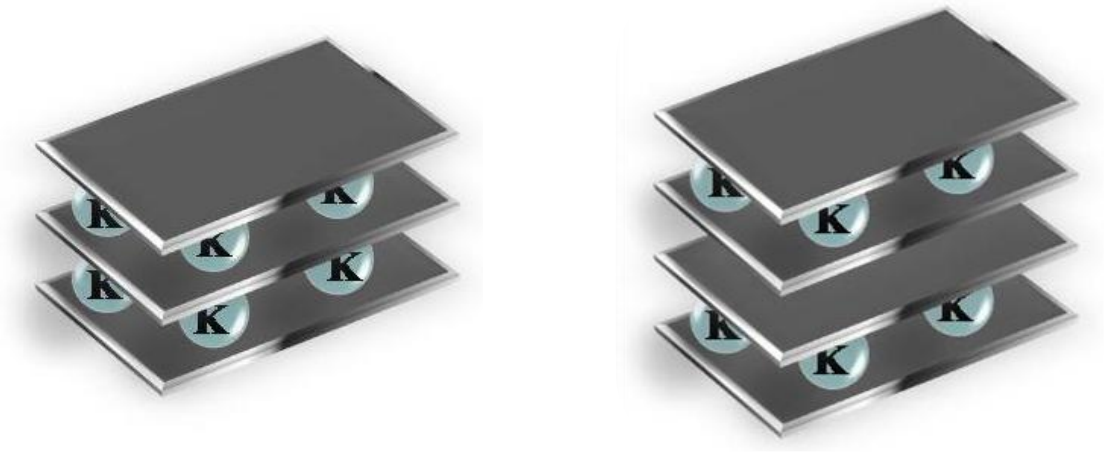

Figure 47: *Left)* Stage I potassium intercalated RW-A graphite. *Right)* Stage II potassium intercalated RW-A graphite.

In a typical reaction, RW-A graphite powder (Ringsdorff® – SGL Carbon group) was heated under vacuum to 700 °C and then 505.4 mg, (42.12 mmol) were introduced in a narrow neck vial. On the other end of the reaction vessel a stoichiometric amount of small pieces of potassium (205 mg, 5.26 mmol) over a Tantalum foil was added. The vial was then evacuated to 0.1 mtorr and sealed.

The temperature difference between the graphite and potassium was achieved using a double furnace The reaction vessel was placed inside the furnace, measured by an Eurotherm thermocouple and manually controlled to ±l °C: T_{RW-A} = 250 °C, T_K = 150°C for 3 h and 375 °C for 3 h(cycled for 4 times). After 24 h reaction time the resulting bright gold powder KC_8 was then cooled to room temperature (705 mg, 99% yield).

Once obtained stage I K-GIC, only the graphite part was reinserted in the oven, treated at 375 °C for 3 h and reduced to a stage II K-GIC (KC_{24}). 574 mg (100% yield) of a blue coloured solid were collected.

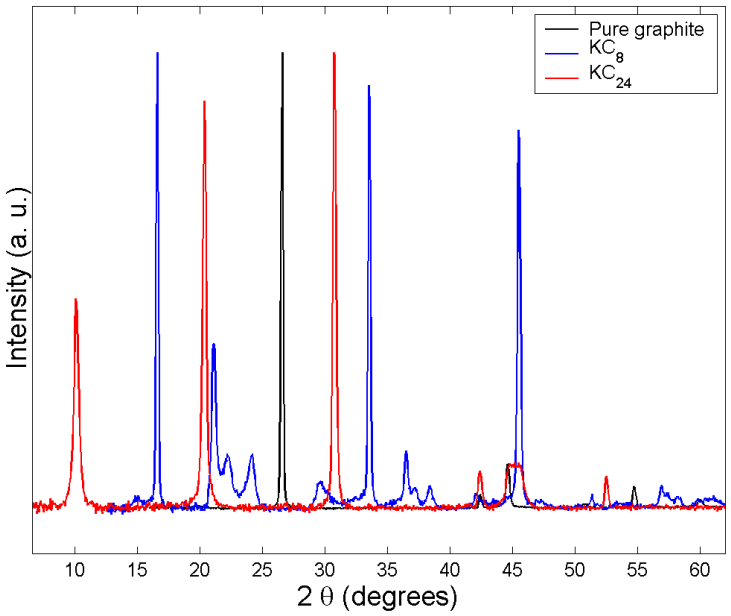

Figure 48: The XRD spectra of pure RW-A graphite (black line), stage I KC_8 (blue line) and the final intercalated product stage II KC_{24} (red line) The disappearance of the main 002 reflection of graphite at $2\theta = 26.4°$ indicates the complete efficiency of the reaction.

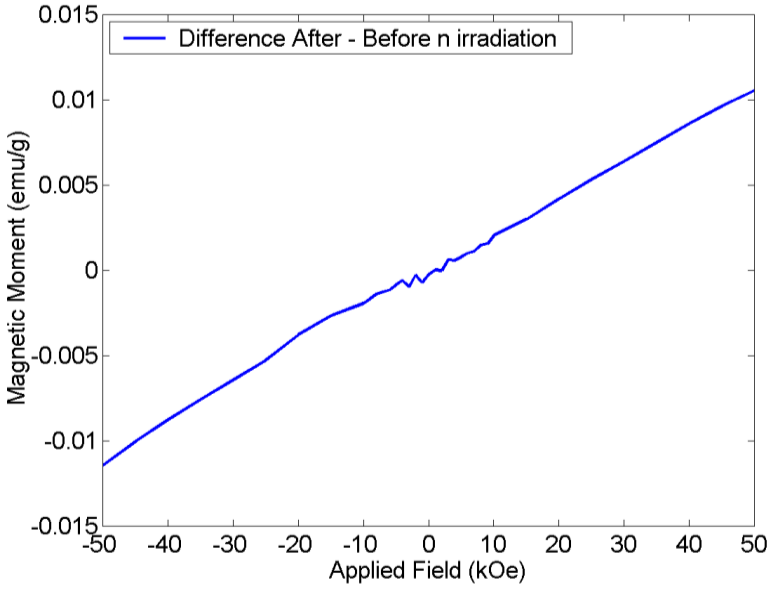

Figure 49: Difference between the room temperature magnetic moment of a sample of KC_{24} after neutron irradiation and the magnetic moment of the same sample before irradiation. Only a linear paramagnetic contribution is present.

4.2.6 Synthesis of Borazine intercalated KC_{24}

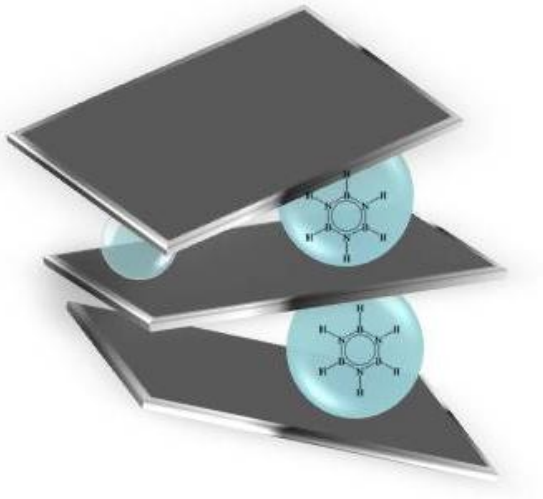

Figure 50: Borazine intercalated KC_{24}.

51.8 mg of KC_{24} were placed into a Schlenk tube in glove box and then drawn out and attached to a three way-Schlenk connector. A Schlenk tube containing 3 cc of Borazine and a vacuum line were connected to the other ends. Once evacuated the KC_{24} tube and the connector space, the Borazine Schlenk was opened in order to expose K-GIC to borazine vapour pressure at 20 torr. The reaction took place in a period of an hour.

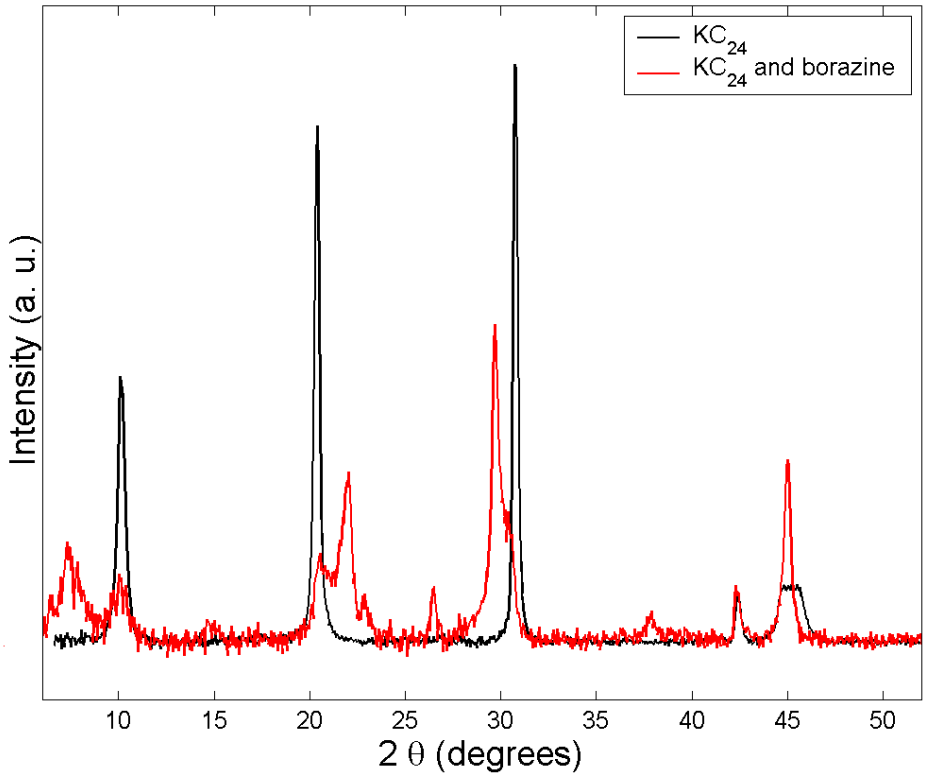

Figure 51: Comparison between the diffraction pattern of the starting KC_{24} (black line) and the diffraction spectrum of the Borazine-GIC product (red line). Here, the presence of new diffraction peaks, which could not be related to those of the reagents, suggests that borazine should be intercalated into the graphite planes, even if a detailed structural study is still in progress.

Regarding magnetic measurements, the SQUID data has already been presented in the "Results and discussion" chapter.

4.2.7 Synthesis of BCl_3 intercalated KC_{24}

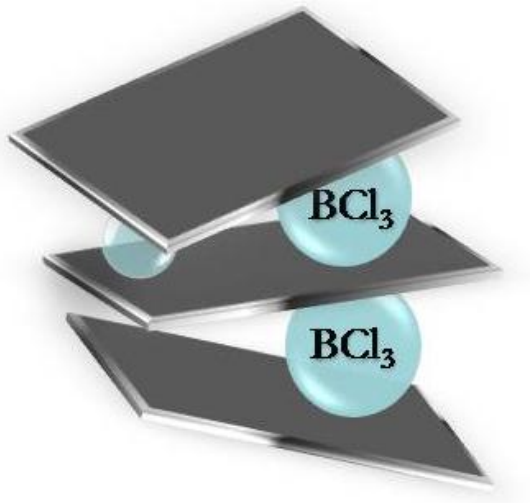

Figure 52: Boron trichloride intercalated KC_{24}.

50.2 mg of KC_{24} were placed into a Schlenk tube in GB and then drawn out and attached to a three way-Schlenk connector. A Schlenk tube containing 2 cc of Boron trichloride and a vacuum line were connected to the other ends. Once evacuated the KC_{24} tube and the connector space, BCl_3 Schlenk were opened in order to expose K-GIC to its vapour pressure at 20 torr. The exothermic reaction took place in a period of 15 min at room temperature and the evidence came from a rapid colour changing from blue to black.

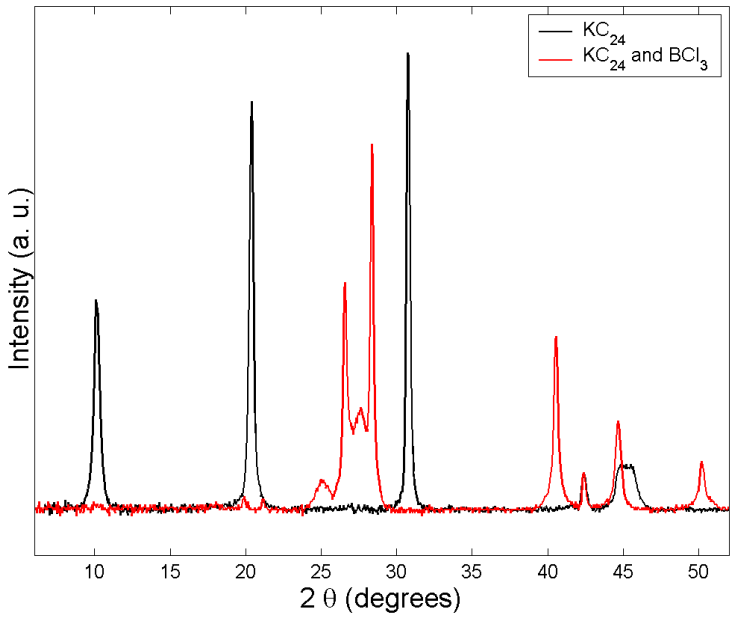

Figure 53: Comparison between the diffraction pattern of the starting KC_{24} (black line) and the diffraction spectrum of the BCl_3-GIC product (red line). Some reflections could be referred to the formation of KCl and pure graphite, thus indicating that part of BCl_3, used as intercalant, reacts with the intercalated potassium.

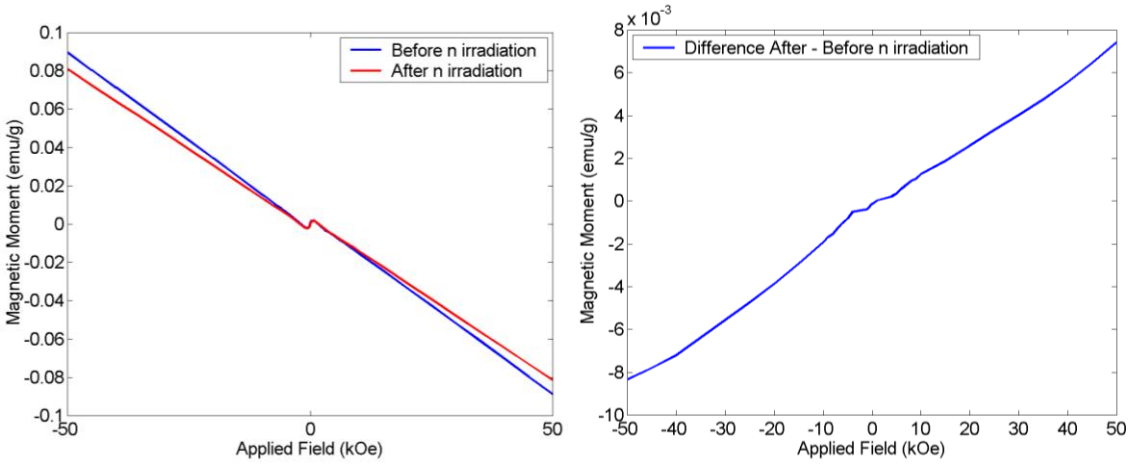

Figure 54: On the left SQUID measurements before and after irradiation of a KC_{24}+BCl_3 sample at 300 K. The right graph shows the difference between the room temperature magnetic moment of the same sample after neutron irradiation and the magnetic moment before irradiation. The irradiation treatment induces the onset of a paramagnetic contribution, but no ferromagnetism is observed.

4.2.8 Synthesis of NH_3 intercalated KC_{24}

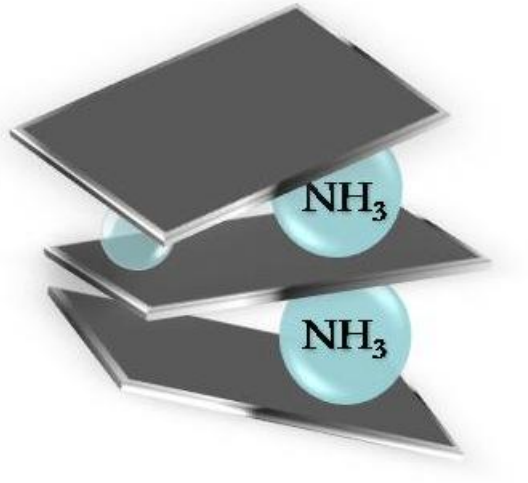

Figure 55: Ammonia intercalated KC_{24}.

53.6 mg of KC_{24} were placed into a Schlenk tube in GB and then drawn out and attached to a three way-Schlenk connector. An ammonia bottle and a vacuum line (see

Scheme **2**) were connected to the other ends. Once evacuated the KC_{24} tube, 0.04 atm of NH_3 were inserted in the reactor gas stage and subsequently in the graphite schlenk. The exothermic reaction took place in a period of 15 min at room temperature and the intercalation evidence came from a rapid colour changing from blue to black (see also XRD analysis presented in Figure 56).

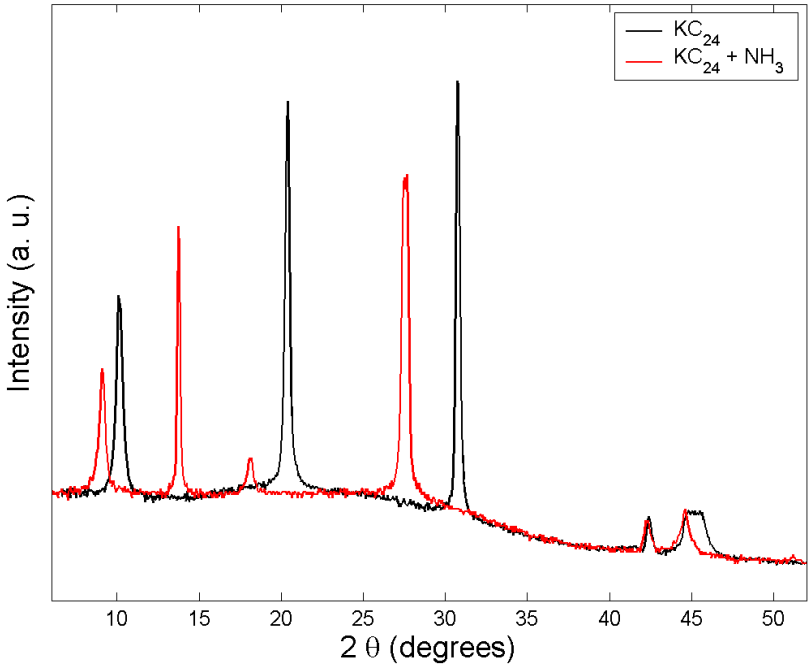

Figure 56: Structure evolution of KC_{24} after the intercalation with ammonia. therein the product (red line) there is a complete disappearance of the peaks of the precursor (black line) , due to the formation of a mixture of stage I and stage II $(NH_3)_xKC_{24}$, approximately with the ratio 1:1.

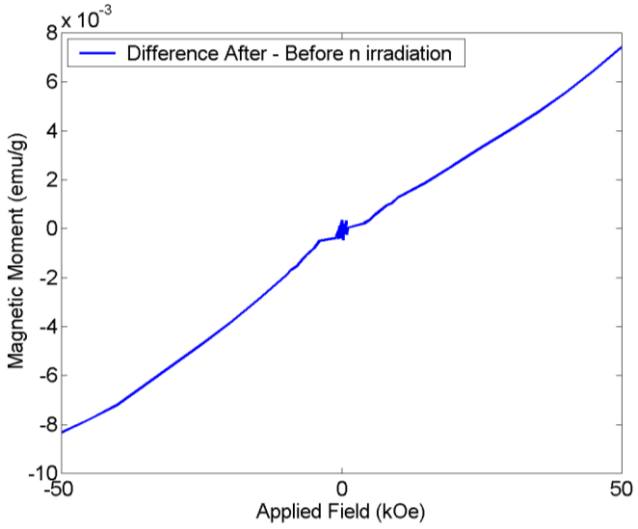

Figure 57: Difference between the room temperature magnetic moment of a sample of ammonia intercalated KC_{24} after neutron irradiation and the magnetic moment of the same sample before irradiation. Only a linear paramagnetic contribution is present.

4.2.9 Synthesis of SO_3 intercalated graphite

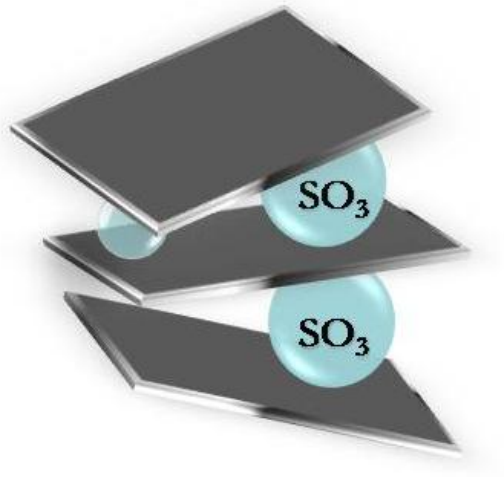

Figure 58: Sulphur trioxide intercalated graphite.

RW-A graphite powder (Ringsdorff® - SGL Carbon group) was pumped under vacuum up to 700 °C and than 82.2 mg were placed into a Schlenk tube in GB and then drawn out and attached to a three way Schlenk connector. A Schlenk tube containing 3 cc of degassed sulphuric acid with approx. 20% SO_3 and a vacuum line were connected to the other ends. Once evacuated the graphite tube and the connector space, the acid-containing Schlenk was opened in order to expose graphite powder to SO_3 vapours. The exothermic reaction took place in a period of 24 hours at 300 °C. The resulting intercalated compound has been structurally (see Figure 59) and magnetically (see Figure 60) characterized.

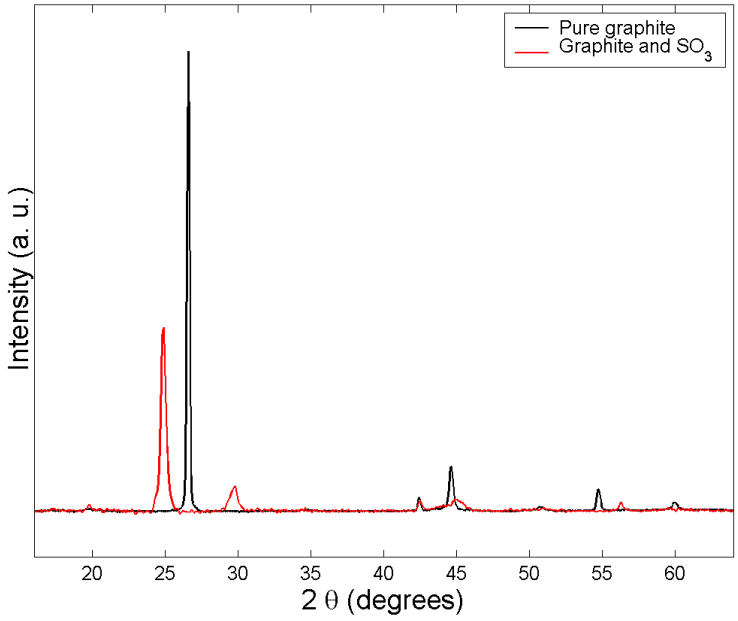

Figure 59: X-ray powder diffractogram of SO_3 intercalated graphite (red line), compared to the diffractogram of pure graphite powder used as a precursor (RW-A grade). The disappearance of the (0 0 2) graphite reflection, as well as the shift of some peaks at lower angles, suggests that the intercalation was complete.

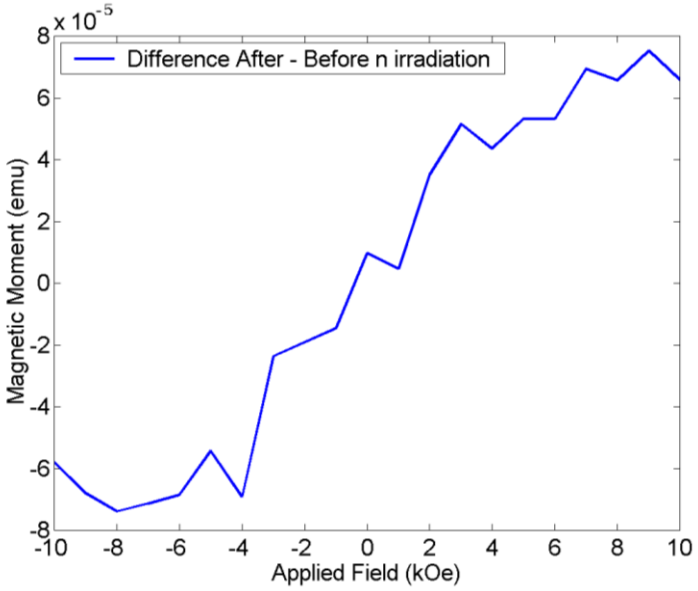

Figure 60: Difference between the room temperature magnetic moment of a sample of sulphur trioxide intercalated graphite after neutron irradiation and the magnetic moment of the same sample before irradiation. No real ferromagnetic signal is observed.

4.2.10 Synthesis of Exfoliated RW-A Graphite

Figure 61: Expanded RW-A graphite.

363 mg of KC_8 were placed into a Schlenk tube in GB and then attached to a three way-Schlenk connector. A Schlenk tube containing 5 cc of degassed and dried over $LiAlH_4$ Ethanol (99.9 %, Fluka) and a vacuum line equipped with a liquid nitrogen trap were connected to the other ends. Once evacuated the KC_{24} tube and the connector space, EtOH Schlenk was opened and the salification reaction occurred in a period of 3 hours. All the K-Ethanolate intercalated graphite was immediately exfoliated. In other words the tube was evacuated and twice thermally treated at 1050 °C for 1 min. The expansion reaction took place in a 30 cm long Pyrex vial. The black high density expanded product was fully characterized.

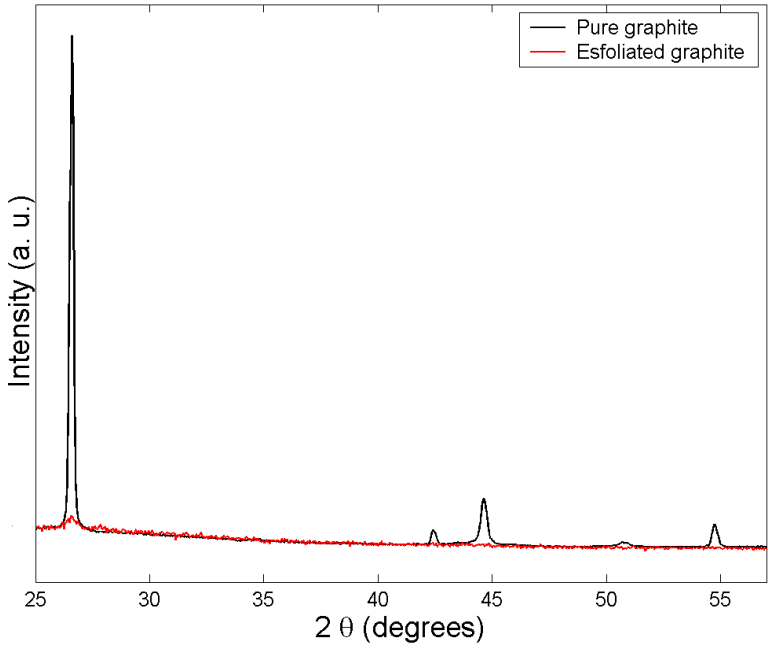

Figure 62: Comparison between the X-ray diffractogram of pure graphite powder, RW-A grade (black line), and that observed in the exfoliated graphite (red line). The disappearance of all the reflections indicates the loss of spatial coherence induced by the exfoliation of the planes.

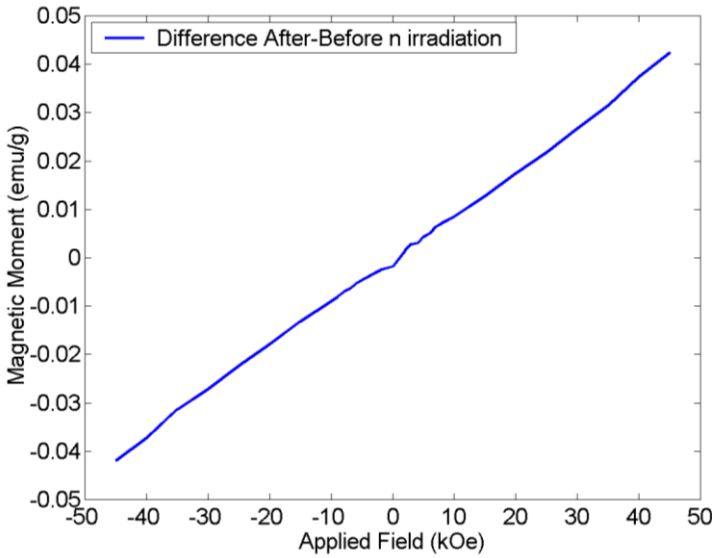

Figure 63: Difference between the magnetization after and before the irradiation treatment on exfoliated graphite at room temperature. The magnetic field dependence evidences a linear paramagnetic contribution.

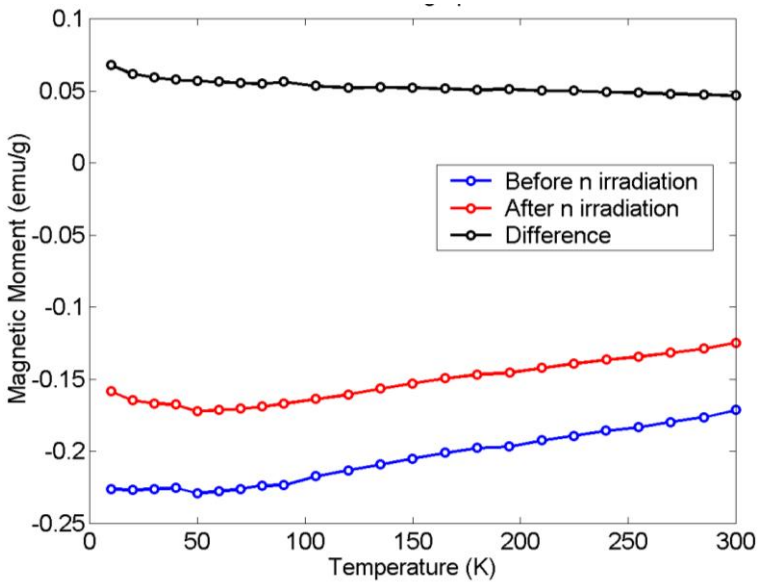

Figure 64: Temperature dependence of magnetization in exfoliated graphite, before (blue) and after (red) neutron irradiation, along with the difference (black) which highlights the effect of the irradiation treatment. The temperature dependence of exfoliated graphite has been interpreted by our SQUID experts through the Kotosonov equation[113], which depends on the γ parameters considered in the Slonckzewsky-Weiss-McClure band model of graphite[114]. The irradiation is expected to introduce a Curie-Weiss paramagnetic component, but may also be responsible of a change in the parameters of the Kotosonov equation.

[113] A. S. Kotosonov, S. V. Kuvshinnikov, *Physics Letters A* **229**, 377-380 (1997).
[114] J. W. McClure, *Physical Review* **108**, 612-618 (1957).

4.2.11 Synthesis of $NaBH_4$ Graphite composite

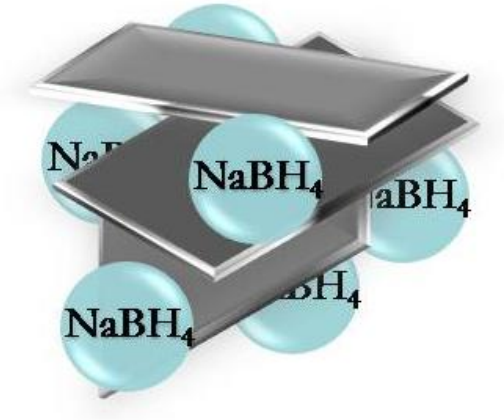

Figure 65: Sodium boron hydride Graphite composites

In a typical synthesis, RW-A graphite powder (Ringsdorff® - SGL Carbon group) was heated under vacuum to 700 °C and then 200 mg were milled for 10 min with 5 minutes stop every 5 min. Afterwards sodiumboronhydride ($NaBH_4$, 99,99% purity, Aldrich, no problems with secondary radioactive products) underwent a milling time of 40 minutes (with 5 min stop every 5 min). After grinding, the two reagents were perfectly mixed together through an additional 3 min milling (one by one) in a ratio of 1, 5, 10, 20, 50% w/w of $NaBH_4$. The samples were finally reduced in pellets and irradiated at the LENA reactor using a special home-designed sample holder.

Regarding magnetic measurements, the SQUID data has already been presented in the "Results and discussion" chapter.

Figures index

Figure 1: *Left)* The structures of eight carbon allotropes, a) Diamond, b) Graphite, c) Lonsdaleite, d) C_{60} (Buckminsterfullerene or buckyball), e) C_{540}, f) C_{70}, g) Amorphous carbon, and h) single-walled carbon nanotube or buckytube. *Right)* Visualization of the two well-known carbon allotropes: Diamond and Graphite 12

Figure 2: Everyday life is full of magnets, for example **a)** modern cars contains up to 30 Kg of high intensity magnetic material, **b)** natural medicine in some cases utilize magnets for therapies, **c)** magnets can even be found in modern toys and **d)** the magnetic resonance technique represents our medical forefront. 13

Figure 3: Ball&stick structure of Fullerene (C_{60}). 15

Figure 4: *Left)* Tetrakisdimethylaminoethylene (red: hydrogen; blue: nitrogen; grey: carbon). *Right)* Structure of $[TDAE]^{+\bullet}$ $C_{60}^{-\bullet}$. 16

Figure 5: The enthalpy of polymerization as a function of the negative charge transfer on C_{60} for several known polymerized structures, either linked with [2+2] cycloaddition reaction or single C-C bond, calculated with thermochemical methods. 19

Figure 6: The field dependence of magnetization at T = 5 K for (a) pristine C_{60} crystal, (b) the sample exposed to light in oxygen for 2.5 hours (c) baked at 400 °C for 2.5 hours, and (d) exposed in air for 3 months. 21

Figure 7: Susceptibility measurements for powder C_{60} sample: (a) pristine; (b) exposed to oxygen in the dark; (c, d) exposed to strong visible light in the presence of oxygen for 48 and 720 h, respectively. 22

Figure 8: Transformations of fullerene C_{60} under pressure: (a): pristine *fcc* lattice, (b): orthorhombic phase, (c): tetragonal phase, (d): rhombohedral phase. 23

Figure 9: SRIM2003 Monte Carlo simulations for 2.25 MeV protons on HOPG. (**a**) The number of defects per ion and per µm depth interval referred to a penetration range of 46 µm. (**b**) Sketch of the modified area in graphite due to 2.25 MeV proton bombardment. The values are obtained assuming a displacement energy of 35 eV for Frenkel pairs in HOPG[69]. 29

Figure 10: The magnetic moment measured at T = 300 K as a function of magnetic field (1 kOe = $10^6 / 4\pi$ Am^{-1}) by cycling the field from zero to +10 kOe, from +10 kOe to -10 kOe, and back to -10 kOe for a sample glued on a silicon substrate, after various proton irradiations. **(a)** Total magnetic moment without any background subtraction for the sample after stages No. 1 (□, homogeneous irradiation of an area 1720 x 1720 μm^2, dose: 0,99 pC / μm^2, total charge: 2,93 µC (proton current I = 1,6 nA)) and No. 3 (●, four spots of 0.8 mm diameter each,

dose: 0.3 nC / μm², total charge: ≈ 600 μC (2 MeV, I = 350 nA)) irradiations. **(b)** Magnetic moment after subtraction of the sample holder magnetic moment, for the sample after the first (□), second (*, 100 x 100 spots of 2 μm diameter each, on an area 570 x 570 μm² in the middle of the sample, dose: 0,3 nC / μm², total charge: ≈ 8 μC (I = 1,6 nA)), third (●), and fourth (Δ, the same as No. 3 (2 MeV, I = 200 nA)) irradiation stages. The inset in (a) shows a smaller field region of the hysteresis loops after the third and fourth irradiation stages. 30

Figure 11: AFM (top left) and MFM images (scan size: 20 × 20 μm²) for a 2 × 2 μm² spot irradiated with 2.25 MeV protons at a fluence of 7.5 × 10^{16} cm^{-2} ~ 0.115 nC μm². The reported AFM and MFM line scans were extracted from the images as indicated by the black triangles. The images show the results of the spot measured after irradiation *(B = 0)*, after exposing it to a field of ~1 kOe in the c direction (B-up) or $-c$ direction *(B-down)* . The measurements were done, however, at zero applied field. 31

Figure 12: Left) on the top are reported AFM and MFM images of a spot irradiated with a 2.25 MeV proton beam and a fluence of 50 nC / μm2. The AFM image reveals the beam impact area. A line scan through its centre reveals a deepening of about 70 nm depth in 5 μm distance. The MFM image suggests a magnetic "ring" around the impact area. On the bottom an STXM images at the Fe, Co, and Ni absorption resonance obtained from the area marked with a dotted line in the force microscopy images above: notice that no contamination is found within the impact area. Right) Carbon K-edge absorption spectrum (bottom) obtained from a sample prepared at room temperature (black) and at 560°C substrate temperature (red). The arrows indicate the photon energies for which the STXM images (top) in the corresponding columns were acquired for a spot irradiated at 50 nC/μm². The helicity (σ) of the x-rays was reversed between the first and the second row of images. For the third row the direction (μ) of the applied field was reversed as well so that both polarization and applied field are opposite to the situation in the first row. Images acquired at the π* resonance (284.0 eV) exhibit a clear XMCD signal. 33

Figure 13: Fullerene salt experimental setup. 42

Figure 14: *Left)* Observed (o) and calculated (solid red line) powder diffraction pattern of $C_{60}(AsF_6)_2$ at 300 K, both from synchrotron and neutron diffraction data. *Right)* The 1D polymeric structure of $C_{60}(AsF_6)_2$, consisting in polymeric chains connected alternatively by single C-C bonds and four-membered carbon rings. 43

Figure 15: Thermal stability of the fullerenium salt $C_{60}(AsF_6)_2$. The polymeric phase disrupts above ~ 450 K and undergoes an irreversible polymer-to-monomer transition, by the contemporary emission of gas. The monomer phase is face centred cubic and persists on cooling the sample. 44

Figure 16: Magnetic SQUID measurements performed on the fullerenium salt in the polymeric state (curve in blue) and after the polymer-to-monomer transition (curve in red). In both cases, the samples show essentially a diamagnetic behaviour, with a small superimposed Curie-Weiss contribution arising from paramagnetic impurities and corresponding respectively to 0.14 and 0.25 ½ spin per C_{60}. 45

Figure 17: Observed (o) and calculated (solid red line) powder synchrotron diffraction pattern of Mg_5C_{60} measured at 300 K (Le Bail analysis). The compound arranges in a rhombohedral lattice, where inter-fullerene distances are compatible with 2D polymerisation. The peaks marked with asterisks are due to unreacted Mg (Rwp = 9.89 %). 48

Figure 18: Magnetic SQUID measurement performed on Mg_5C_{60}. A small Curie-Weiss contribution, due to the presence of paramagnetic impurities, is superimposed to a Pauli constant contribution, probably arising from the metallic unreacted Mg. 49

Figure 19: The TRIGA MARK II LENA reactor (Pavia, ITALY). 51

Figure 20: Top view of the LENA irradiation channels. 52

Figure 21: Triga Mark II reactor horizontal section: underlined in red the central channel in which the samples irradiation was performed. 53

Figure 22: On the left the home-made sample holder project and on the right its visualization. 54

Figure 23: Nuclear interaction between a ^{10}B atom and an incident neutron particle (E_n ~ 1 eV). 55

Figure 24: The bimodal spectrum of LENA reactor (250 KW, Pavia, Italy). The red curve shows the neutron flux spectrum, while the curve in blue represents the boron cross section. The black curve is the corresponding reaction rate spectrum. 55

Figure 25: SRIM2003 Monte Carlo simulations of vacancies generated by the products of neutron irradiation of boron, namely ^7Li (read line) and ^4He (purple line); a comparison with the damage effect of 2 MeV protons is also reported (blue line, magnified by a 20 factor). 56

Figure 26: Trend of the nuclear reactions rate with respect to boron doping. On the same graph the trend of Lambda parameter compared to the boron doping is also reported. The shaded region has been identified as the ideal boron doping percentage. 57

Figure 27: SRIM2003 Monte Carlo simulations of emitted particle ranges in Graphite and in the boron carrier: $NaBH_4$. 58

Figure 28: Lambda represents the neutrons penetration depth as a function of RW-A graphite sample thickness and it shows the trend of nuclear explosions through sample width. 59

Figure 29: X-rays powder diffraction of different RW-A graphite samples. The black graph shows diffraction pattern of pure RW-A graphite (Ringsdorff® - SGL Carbon group) heated under vacuum at 700 °C for 7h. The other coloured diffractograms are referred to milled graphite samples respectively for 5, 10 and 15 minutes, stopping grinding every 5 minutes. 60

Figure 30: On the left the milling apparatus equipped with a jar is showed while on the other side can be seen the effect of grinding onto graphite planes: in-plane defects but also planes breaking are expected. 61

Figure 31: SQUID measurements showing the paramagnetism extracted from the graphite diamagnetic background (inset) are reported – all sample operations were performed in a controlled atmosphere glove-box – . 61

Figure 32: **left)** Transmission Electron Microscopy image of 1h high-frequency ball-milled RW-A graphite; it could be recognised the presence of both 2D (layers) and 1D (ribbons) structures. **right)** Image of a ribbon-like structure. 62

Figure 33: Ball-milled graphite (BMG) morphology has been fully characterized using TEM microscopy (left image). In particular we can see the layered structure with the characteristic graphite stacking distance of ~3.4 Å. The mean thickness of the observed multigraphene ribbons is confirmed to be ~ 6 nm. 63

Figure 34: Distribution of displaced atoms and vacant lattice sites (secondary defects) due to a single knock-on atom (primary defect). 65

Figure 35: *Left*) Potassium intercalated graphite (KC_{24}) treated with SO_3 vapours experimental setup. *Right*) The intercalation moment; colour changing can be clearly seen, the intercalation starting from the top of the vial and results from the diffusion of the intercalant into graphite powder. 66

Figure 36: Teflon sample holder degradation after the first longer irradiation section. Even though we used a high purity Teflon containers, as suggested by the LENA local contact, they encounter degradation after neutron treatment. 67

Figure 37: Typical temperature dependence in an irradiated sample (KC_{24} + borazine in this case, field cooling measurement applying a field of 5 Tesla). A difference is present only in the temperature independent susceptibility and in the Curie-Weiss paramagnetic contribution of the defects. No steep increase in the magnetization due to the onset of magnetic order was detected. 69

Figure 38: SQUID measurements showing the decrease of diamagnetism in $NaBH_4$ enriched graphite after neutron irradiation (measurements performed either on RW-A graphite purity grade and previously on the lower purity grade VSP-C graphite). 70

Figure 39: Patterns of diffracted x-rays: different examples depending on the specimen nature. 77

Figure 40: Five major components in an X-ray powder diffractometer, an area detector, an x-ray generator, x-ray optics (monochromator and collimator), goniometer and sample stage, sample alignment and monitoring (laser/video) system. 79

Figure 41: Fullerenium dihexafluoroarsenate. 81

Figure 42: Magnesium-Anthracene organometallic complex. 83

Figure 43: Mg-C_{60} polymer with the nominal stoichiometry Mg_5C_{60}. 84

Figure 44: The Borazine structure; it is also called the "Inorganic benzene". 85

Figure 45: Borazine synthesis experimental setup. 86

Figure 46: ^{1}H-NMR spectra of our borazine. In particular can be observed B –H proton at δ 4-5 ppm as a quartet and N–H proton at 5.5-6 ppm as a triplet. 87

Figure 47: *Left)* Stage I potassium intercalated RW-A graphite. *Right)* Stage II potassium intercalated RW-A graphite. 88

Figure 48: The XRD spectra of pure RW-A graphite (black line), stage I KC_8 (blue line) and the final intercalated product stage II KC_{24} (red line) The disappearance of the main 002 reflection of graphite at $2\theta = 26.4°$ indicates the complete efficiency of the reaction. 89

Figure 49: Difference between the room temperature magnetic moment of a sample of KC_{24} after neutron irradiation and the magnetic moment of the same sample before irradiation. Only a linear paramagnetic contribution is present. 89

Figure 50: Borazine intercalated KC_{24}. 90

Figure 51: Comparison between the diffraction pattern of the starting KC_{24} (black line) and the diffraction spectrum of the Borazine-GIC product (red line). Here, the presence of new diffraction peaks, which could not be related to those of the reagents, suggests that borazine should be intercalated into the graphite planes, even if a detailed structural study is still in progress. 91

Figure 52: Boron trichloride intercalated KC_{24}. 92

Figure 53: Comparison between the diffraction pattern of the starting KC_{24} (black line) and the diffraction spectrum of the BCl_3-GIC product (red line). Some reflections could be referred to the formation of KCl and pure graphite, thus indicating that part of BCl_3, used as intercalant, reacts with the intercalated potassium. 93

Figure 54: On the left SQUID measurements before and after irradiation of a KC_{24}+BCl_3 sample at 300 K. The right graph shows the difference between the room temperature magnetic moment of the same sample after neutron irradiation and the magnetic moment before irradiation. The irradiation treatment induces the onset of a paramagnetic contribution, but no ferromagnetism is observed. 93

Figure 55: Ammonia intercalated KC_{24}. 94

Figure 56: Structure evolution of KC_{24} after the intercalation with ammonia. therein the product (red line) there is a complete disappearance of the peaks of the precursor (black line) , due to the formation of a mixture of stage I and stage II $(NH_3)_xKC_{24}$, approximately with the ratio 1:1. 95

Figure 57: Difference between the room temperature magnetic moment of a sample of ammonia intercalated KC_{24} after neutron irradiation and the magnetic moment of the same sample before irradiation. Only a linear paramagnetic contribution is present. 95

Figure 58: Sulphur trioxide intercalated KC_{24}. 96

Figure 59: X-ray powder diffractogram of SO_3 intercalated graphite (red line), compared to the diffractogram of pure graphite powder used as a precursor (RW-A grade). The disappearance of the (0 0 2) graphite reflection, as well as the shift of some peaks at lower angles, suggests that the intercalation was complete. 97

Figure 60: Difference between the room temperature magnetic moment of a sample of sulphur trioxide intercalated KC_{24} after neutron irradiation and the magnetic moment of the same sample before irradiation. No real ferromagnetic signal is observed. 97

Figure 61: Expanded RW-A graphite. 98

Figure 62: Comparison between the X-ray diffractogram of pure graphite powder, RW-A grade (black line), and that observed in the exfoliated graphite (red line). The disappearance of all the reflections indicates the loss of spatial coherence induced by the exfoliation of the planes. 99

Figure 63: Difference between the magnetization after and before the irradiation treatment on exfoliated graphite at room temperature. The magnetic field dependence evidences a linear paramagnetic contribution. 99

Figure 64: Temperature dependence of magnetization in exfoliated graphite, before (blue) and after (red) neutron irradiation, along with the difference (black) which highlights the effect of the irradiation treatment. The temperature dependence of exfoliated graphite has been interpreted by our SQUID experts through the Kotosonov equation, which depends on the γ parameters considered in the Slonckzewsky-Weiss-McClure band model of graphite. The irradiation is expected to introduce a Curie-Weiss paramagnetic component, but may also be responsible of a change in the parameters of the Kotosonov equation. 100

Figure 65: Sodium boron hydride Graphite composites 101

Schemes index

Scheme 1: Phase Diagram of pure polymerized C_{60}. **A** indicates the existence range of atomic carbon due to the collapse of C_{60} cage, **M** corresponds to the monomeric state. **Mp** is the range of polymerized C_{60}, both tetragonal (**T**) and rhombohedral (**R**). 20

Scheme 2: Three stage glass reactor employed in the synthesis of $C_{60}(AsF_6)_2$. 40

Scheme 3: Fullerenium salt reaction scheme. 41

Scheme 4: $MgAnt(THF)_3$ synthetic scheme. 46

Scheme 5: $Mg_{x=4-5}C_{60}$ polymer synthetic scheme. To notice that the stoichiometry of this compound has not been completely investigated. All presented data are preliminary results. 47

Scheme 6: Exfoliation process of a graphite sample. Firstly pristine graphite powder is exposed to potassium vapours in order to reach a stage I intercalation (KC_8), then the GIC is exposed to ethanol vapours promoting the synthesis of a K-ethanolate *intra*-planes. Finally a high and fast thermal treatment lets the CH_3CH_2OK decomposing, thus inducing the separation of the planes. 68

Bibliography

Abe H., H. Naramoto, A. Iwase and C. Kinoshita, Effect of damage cascades on the irradiation-induced amorphization in graphite. *Nuclear• Instruments and Methods in Physical Research Section B*, 127/128, 681–684 (1997). 30

Akutsu S. and Y. Utsushikawa, *Mater. Sci. Res. Int.* 5, 110 (1999). 36

Allemand P M, Kishan K C, Koch A, Wudl F, Holczer K. and Thompson J D, *Science* 253, 301-3 (1991). 16

Andriotis A. N., R. M. Sheets, M. Menon, *Phys. Rev. B* **74**, 153403 (2006). 39

Antonov V. E., I. O. Bashkin, S. S. Khasanov, A. P. Moravsky, Yu. G. Morozov, Yu. M. Shulga, Y.A. Ossipyan, E. G. Ponyatovsky, *J. Alloys, and Comp.* **330**, 365 (2002). 18

Ata M., M. Machida, H. Watanabe, and J. Seto., *Jpn. J. Appl. Phys.* **33**,1865 (1994). 17

Auerbach, A., Manini, N., and Tosatti, E., Electron-vibron interactions in charged fullerenes. I. Berry phases, *Physical Review B* **49**, 12998 (1994). 40

Banhart F., Irradiation effects in carbon nanostructures, *Reports on Progress in Physics*, **62**, 1181–1221 (1999). 29

Barzola-Quiquia J., P. Esquinazi, M. Rothermel, D. Spemann, T. Butz, N. Garcia, *Phys. Rev. B* **76**, 161403 (2007). 27

Borondics F., *et al.*, *Sol. State Comm.*, **127**, 311 (2003). 46

Boukhvalov D.W. and M. I. Katsnelson, cond-mat: arXiv:0712.2928v1 (2007). 39

Boukhvalov, D. W. et al. Testing the magnetism of polymerized fullerene. *Phys. Rev. B* **69**, 115425 (2004). 25

Bruno C. et al., *J. Am. Chem. Soc.* **125**, 15738 (2003). 41

Caudillo R., X. Gao, R. Escudero, J. B. Goodenough, *Phys. Rev. B* **74**, 214418 (2006). 15

Chan J. A., B. Montanari, J. D. Gale, S. M. Bennington, J. W. Taylor, and N. M. Harrison, *Phys. Rev. B* **70**, 041403 (2004). 25

Datars W. R. and P. K. Ummat, Identification of AsF_6^- in C_{60}, *Solid State Communications* **94**, 649 (1995). 41

Datars W. R., Chien, T. R., Nkum, R. K., and Ummat, P. K, Intercalation of AsF_5 in C_{60}, *Physical Review B* **50**, 4937 (1994). 41

Datars W. R., Palidwar, J. D., and Ummat, P. K. Identification of acceptors in C_{60}, *Journal of Physics and Chemistry of Solids* **57**, 977 (1996). 41

Davydov V. A., H. Szwarc *et al*, "Tetragonal polymerized phase of C_{60}", *Phys Rev B* **58**, 14786 (1998). 21

Dubman M., T. Shiroka, H. Luetkens, M. Rothermel, F. J. Litterst, E. Morenzoni, A. Suter, D. Spemann, P. Esquinazi, A. Setzer, and T. Butz, *Join European Magnetic Symposia (JEMS08)*, to be published in JMMM. 35

Ekimov E. A., V. A. Sidorov, E. D. Bauer, N. N. Mel'nik, N. J. Curro, J. D. Thompson, S. M. Stishov, *Nature* **428** 542 (2004). 13

Esquinazi P., A. Setzer, R. Hoehne, C. Semmelhack, Y. Kopelevich, D. Spemann, T. Butz, B. Kohlstrunk, and M. Loesche. *Phys. Rev. B* **66**,024429 (2002). 28

Esquinazi P., D. Spemann, R. Höhne *et al.*, Carbon-Based Magnetism: An Overview of the Magnetism of Metal-Free Carbon-Based Compounds and Materials, Makarova, T. and Palacio, F. (Eds.), Elsevier Science, pp. 437–462, chapter 19 (2006). 28

Esquinazi P., D. Spemann, R. Höhne *et al.*, Induced magnetic ordering by proton irradiation in graphite. *Physical Review Letters* **91**, 227201-4 (2003). 28

Esquinazi P., *et al.*, "Magnetic order in proton irradiated graphite: Curie temperatures and magnetoresistance effect", Journal of Nuclear Material in press (presented at TMS 2008 Meeting). 51

Evolution of the preliminary PhD work of dr. Massimo Pagliari and dr. Fabio Gianferrari. 41

Faccio R., H. Pardo, P. A. Denis, R. Y. Oeiras, R. Yoshikawa, F. M. Araujo-Moreira, M. Verissimo-Alves, A. W. Mombru, *Phys. Rev.B* **77**, 035416 (2008). 28

Fazen P. J., J. S. Beck, A. Lynch, E. E. Remsen and L. G. Sneddon, *Chem Mater.* **2**, 96 (1990). 88

Fernandez-Rossier J., *Phys. Rev. B* **77**, 075430, (2008). 27

Fernandez-Rossier J., *Phys. Rev. Lett.* **99**, 177204 (2007). 27

Goffredi A., M. Pagliari, D. Pontiroli, T. Shiroka, M. Belli, F. Gianferrari, G. Zandomeneghi and M. Riccò, *manuscript in preparation.* 44

Han K. H., D. Spemann, P. Esquinazi *et al.*, Ferromagnetic spots in graphite produced by proton irradiation, *Advanced Materials* **15**, 1719–1722 (2003a). 29

Han, K. H. *et al.*, Observation of intrinsic magnetic domains in C_{60} polymer. *Carbon* **41**, 785–795 (2003); addendum **431,** 2425–2426 (2003). 25

Heisenberg W., *Z. Phys.* **49,** 636 (1928). 14

Höhne R., P. Esquinazi, K. H. Han *et al.*, Ferromagnetic structures in graphite and amorphous carbon films produced by high energy proton irradiation. In *Proceedings of the 16 International Conference of Soft Magnetic Materials*, Raabe, D. (Ed.), pp. 185–190 (2004a) (ISBN 3-514-00711-X). 32

Höhne, R. & P. Esquinazi, Can carbon be ferromagnetic? *Adv. Mater.* **14**, 753–756 (2002). 25

Ishii K., A. Fujiara, H. Suernatsu, Y. Kubozono, *Phys. Rev. B*, **65** 134431 (2002). 13

Ivanovskii A. L., *Phys.Usp.* **50**, 1031 (2007). 27

Iwasa Y. *et al.*, "New phases of C_{60} synthesized at high pressure", *Science* **264**, 1570 (1992). 19

Jin C. Q., X. Wang, Z. X. Liu, Y.L. Zhang, F.Y. Li, and R.C.Yu. Braz, *J. Phys.* **33**,723 (2003). 35

Kelly B. T., *Physics of Graphite*, Applied Science Publishers, London (1981). 28

Kempa H., P. Esquinazi and Y. Kopelevich, *Phys. Rev. B*, **65** 241101(R). 12

Kopelevich Y., J. H. S. Torres, R. R. da Silva, F. Mrowka, H. Kempa, and P. Esquinazi, *Phys. Rev. Lett.*, **90** 156402 (2003). 13

Kopelevich Y., P. Esquinazi, J. H. S. Torres, R. R. da Silva, and H. Kempa, *Advances in Solid State Physics* **43**, 207 (2003). 13

Kopelevich Y., P. Esquinazi, J. H. S. Torres, S. Moehlecke, *J. Low Temp. Phys.* **119**, 691 (2000). 28

Kopelevich Y., R. R. da Silva, J. H. S. Torres, A. Penicaud, and T. Kyotani, *Phys. Rev. B* **68**, 092408 (2003). 36

Kotosonov A. S., S. V. Kuvshinnikov, *Physics Letters A* **229**, 377-380 (1997). 101

Kumar A., D. K. Avasthi, J. C. Pivin, A. Tripathi, F. Singh, *Phys. Rev. B.* **74**, 153409 (2006). 15

Kumazaki H., D. S. Hirashima, *J. Phys. Soc. Jpn.*, **76**, 064713 (2007). 27

Kusakabe K. and M. Maruyama, *Phys. Rev. B* **67**, 092406 (2003). 35

Lee H., *et al.*, *Chemical Physics Letters* **398**, 207–211 (2004). 61

Lehtinen P. O., A. S. Foster, Y. Ma *et al.* Irradiation induced magnetism in graphite: a density-functional study. *Physical Review Letters* **93**, 187202-1–187202-4 (2004). 30

Li S., Z.G. Huang, L. Lue, F. M. Zhang, Y. Du, Y. Cai, Y. G. Pan, *Appl. Phys. Lett.* **90,** 232507 (2007). 15

Lobach A. S., Yu. M. Shulga, O.S. Roshchupkina, A. I. Rebrov, A. A. Perov, Y. G. Morozov, V. N. Spector, and A. A. Ovchinnikov, *Fullerene Sci. Technol.* **6**, 375 (1998). 18

Lopez-Urias F., J. A.Rodriguez-Manzo, M. Terrones, H.Terrones, *Int. J. Nanotech.* **4,** 651(2007). 15

Lüders M., Bordoni, A., Manini, N., Corso, A. D., Fabrizio, M., and Tosatti, E., Coulomb couplings in positively charged fullerene, *Philosophical Magazine B* **82**, 1611(2002). 40

Lüders M., Manini N., Gattari P., and Tosatti E., Hund's rule magnetism in C_{60} ions, *The European Physical Journal B* **35**, 57 (2003). 40

M. A. N. Araújo, N. M. R. Peres, *J. Phys.: Condens. Matter* 18, 1769 (2006). 27

Ma Y. C., P. O. Lehtinen, A. S. Foster, and R. M. Nieminen, *Phys. Rev. B* **72**, 085451 (2005). 35

Makarova T. L. *et al.*, *Carbon* **41**, 1575 (2003). 23

Makarova T. L. in "Progress in Industrial Mathematics" Vol. 12, L. L. Bonilla et al., Eds. 467 (2007). 15

Makarova T. L., B. Sundqvist, R. Höhne, P. Esquinazi, Y. Kopelevich, P. Scharff, V. Davydov, L. S. Kashevarova, and A. V. Rakhmanina, *Nature* **413**,716 (2001). 24

Makarova T. L., *Studies of high-T꜀ Superconductivity*, **45**, 107 (2003). 14

Makarova T., F. Palacio, Carbon based magnetism: an overview of the magnetism of metal free carbon-based compounds and materials, Elsevier Science, 576 pag (2006). 15

Manini N., Tosatti, E., and Auerbach, A, Electron-vibron interactions in charged fullerenes. II. Pair energies and spectra, *Physical Review B* **49**, 13008 (1994). 40

Marques L., M. N. Regueiro, V. D. Blank *et al*, *Science* **283**, 1720 (1999). 19

McClure J. W., *Physical Review* **108**, 612-618 (1957). 101

Mellon E. K., B. M. Coker and P. B. Dillon, *Inorganic Chemistry* **11**, 852-857 (1972). 88

Mombrú A. W., H. Pardo, R. Faccio, O. F. de Lima, A. J. C. Lanfredi, C. A. Cardoso, E. R. Leite, G. Zanelatto, and F. M. Araújo-Moreira, *Phys. Rev. B* **71**, 100404(R) (2005). 36

Morenzoni E., H. Glückler, T. Prokscha, R. Khasanov, H. Luetkens, M. Birke, E. M.Forgan, Ch. Niedermayer, M. Pleines, *Nucl. Instrum. and Methods B* **192**, 254 (2002). 35

Murakami Y. and H. Suematsu, *Pure Appl. Chem.* **68,** 1463 (1996). 18

Murata K., H. Ushijima, H. Ueda and K. Kawaguchi, A stable carbon-based organic magnet. *Journal of the Chemical Society, Chemical Communications*, 567–569 (1992). 28

Murata K., H. Ushijima,H. Ueda and K. Kawaguchi, Magnetic properties of amorphous-like carbons prepared by tetraaza compounds by the chemical vapour deposition (CVD) method, *Journal of the Chemical Society, Chemical Communications*,•1265–1266 (1991). 28

Narozhnyi V. N., K.-H. Müller, D. Eckert, A. Teresiak, L. Dunsch, V. À. Davydov, L. S. Kashevarova, and A. V. Rakhmanina. *Physica B* **329**, 1217 (2003). 25

Niwase, K. (1995). Irradiation-induced amorphization of graphite. *Physical Review B*, **52**, 15785–15798. 29

Nunez-Regueiro M., L. Marques *et al.*, Polymerized fullerite structure", *Phys. Rev. Lett.* **74**, 278 (1995). 19

Ohldag H., T. Tyliszczak, R. Höhne, D. Spemann, P. Esquinazi, M. Ungureanu, T. Butz, π-Electron Ferromagnetism in Metal-Free Carbon Probed by Soft X-Ray Dichroism, *Phys. Rev. Lett.* **98**, 187204 (2007). 15

Owens F. J., Z. Iqbal, L. Belova, and K. V. Rao., *Phys. Rev. B* **69**, 033403 (2004). 23

Pardo H., A. Mombrú, and F.M. Araújo-Moreira, *Patent PI* 0402338-2 (2004). 36

Parkansky N., B. Alterkop, R. L. Boman, Z. Barkay, Y. Rosenberg, N. Eliaz, *Carbon* **46,** 215 (2008). 15

Pei X. Y., X. P. Yang, and J. M. Dong, *Phys. Rev. B* **73**, 195417 (2006). 35

Pekker S., G. Oszlanyi and G. Faigel, "Structure and stability of covalently bonded polyfulleride ions in A_xC_{60}", *Chem. Phys. Lett.* **282**, 435 (1998). 20

Pennikod K., Highlights of the year. *Physics Web* **20** (2001). 14

Pisani L., J. A. Chan, B. Montanari and N. M. Harrison, A defective graphene phase predicted to be a room temperature ferromagnetic semiconductor, *New Journal of Physics* **10**, 033002 (2008). 15

Pisani L., J. A. Chan, B. Montanari and N. M. Harrison, Electronic structure and magnetic properties of graphitic ribbons, *Physical Review B* **75**, 064418 (2007). 51

Quintavalle D., F. Borondics, G. Klupp, A. Baserga, F. Simon, A. Jánossy, K. Kamarás and S. Pekker, *Phys. Rev. B* **77**, 155431 (2008). 46

Rao A., T. Lee, X. X. Bi, "Photoinduced polymerization of solid C_{60} films", *Science* **259**, 955 (1991). 18

Rode A. V., E. G. Gamaly, A. G. Christy, J. D. Fitz Gerald, S. T. Hyde, R. G. Elliman, B. Luther-Davies, A. I. Veinger, J. Androulakis, and J. Giapintzakis, *Phys. Rev. B* **70**, 054407 (2004). 36

Spemann D., *et al.* Evidence for intrinsic weak ferromagnetism in a C_{60} polymer by PIXE and MFM. *Nucl. Instrum. Meth. B* **210**, 531–536 (2003). 25

Spemann D., K. H. Han, P. Esquinazi *et al.*, Ferromagnetic microstructures in highly oriented pyrolytic graphite created by high energy proton irradiation. *Nuclear Instruments and Methods in Physical Research Section B* **219–220**, 886–890 (2004). 29

Stöhr J., *NEXAFS Spectroscopy*, Springer Series in Surface Sciences Vol. 25 (Springer, Heidelberg, 1992). 33

Talyzin A., A. Dzwilewski, L. Drubovinsky, A. Setzer, & P. Esquinazi, Magnetic properties of polymerized C_{60} with Fe, *The European physical journal B* **55**, 57-62 (2007). 18

Tanabe T., Radiation damage of graphite - degradation of material parameters and defect structures. *Physica Scripta*, **T64**, 7–16 (1996). 29

Tokumoto T., E. Jobiliong, E. S. Choi, Y. Oshima, and J. S. Brooks, *Solid State Commun.* **129**, 599 (2004). 13

Wang W. L., S. Meng, E. Kaxiras, *Nano Lett.* **8**, 241 (2008). 27

Wang X., Z. X. Liu, Y. L. Zhang, F. Y. Li, and C. Q. Jin, J. Phys.: *Condens. Matter.* **14**,10265 (2002). 35

Wood R. A., M. H. Lewis, M. R. Lees, S. M. Bennington, M. G. Cain, and N. Kitamura, *J. Phys. Condens. Matter.* **14**, L385 (2002). 25

Yanada T., Japanese Patent JP5159915 (1993). 17

Yazyev O. V., L. Helm, *Phys. Rev. B* **75**, 125408 (2007). 27

Yazyev O. V., L. Wei, S. M. Wang, E. Kaxiras, *Nano Lett.* **9**, 766 (2008). 27

Yazyev O. Y., M. I. Katsnelson, *Phys. Rev. Lett.* **100**, 047209 (2008). 27

Zhang Y., S. Talapatra, S Kar, R. Vajtai, S. K. Nayak, P. M. Ajayan, *Phys. Rev. Lett.* **99**, 107201 (2007). 28

Acknowledgements

Finally I want to acknowledge...ooops!!!

Credo che almeno quest'ultima parte, per essere realmente incisiva, debba essere scritta in lingua madre.

Desidero principiare dai "ringraziamenti di rito", d'altronde così è stato nelle due tesi precedenti e quindi perché evadere una così fulgida tradizione. Ringrazio quindi il Prof. Mauro Riccò per avermi fatto imbarcare su questa nave povera di soddisfazioni ma ricca di enormi delusioni nonché di avermi fatto comprendere chiaramente quanto mi appaia distante il suo metodo di "ricerca" e di vita.

Ringrazio tutti i miei collaboratori che nei tre anni di dottorato mi hanno dato, seppur con alti e bassi, un valido supporto fisico e morale citando in particolare Matteo Belli, unico efficace ed instancabile revisore del presente lavoro. Ringrazio inoltre le persone che ho conosciuto in questi tre anni e che, chi più e chi meno, hanno contribuito a rendere questo periodo una grande esperienza di vita: Paolo (peccato...), Fabio (grande!), Daniele (grazie del tuo aiuto), Toni (a presto), Matteo (la vita è sorprendersi), Marcello ed Alessandra (grazie), Alberto & Co (un'officina con i fiocchi!), Marco (sei forte, a presto), Amoretti (grazie del rapporto umano).

Terminata la lista colleghi & Co viene da sé procedere con i ringraziamenti di coloro i quali mi sono stati vicini in questi anni e che fanno parte di me e della mia "second life": il Canto: Leo (sei importante ricordalo sempre), Roberto&Antonella (vvb), Lelio (è banale ma ... grazie!), Domenico (grazie x la tua amicizia), Massimo&Mauro (mittici). Grazie anche a Diego, Barbara, Cristian e Silvana, ci si vede da poco ma è come se ci fossimo sempre conosciuti.

Un grazie alla mia famiglia ed al mio adorato anche se un po' "serrvatico" Fabio.

Ed infine ringrazio te, amore mio: ogni giorno hai arginato qualsiasi mia elucubrazione negativa, hai letto la mia anima come fosse un libro e ne hai dipinto le pagine, hai condotto il mio cuore fino a questo momento come un eroe conduce il proprio esercito a vittoria certa; in due parole: sei fantastica.